Epipolar Consistency in Transmission Imaging

Die Epipolare Konsistenz in der Transmissionsbildgebung

Der Technischen Fakultät
der Friedrich-Alexander-Universität
Erlangen-Nürnberg

zur

Erlangung des Doktorgrades Dr.-Ing.

vorgelegt von

André Aichert

aus

Hersbruck, Deutschland

Als Dissertation genehmigt
von der Technischen Fakultät
der Friedrich-Alexander-Universität Erlangen-Nürnberg

Tag der mündlichen Prüfung:	27.11.2019
Vorsitzende des Promotionsorgans:	Prof. Dr.-Ing. Andreas P. Fröba
Gutachter:	Prof. Dr.-Ing. Andreas K. Maier
	Prof. Dr.-Ing. Harald Köstler

Abstract

Two X-ray projection images of a rigid object may have different points of view, yet redundant information can be identified in such images. Not unlike a checksum, these occur naturally in the data and are known as consistency conditions. Real acquisitions, however, result from a measurement process which is affected by inaccurate geometric calibration of the scanner, physical effects such as scatter and beam-hardening or in some applications patient motion. These effects can be observed as differences between theoretically redundant information in the data and, to some extent, can be corrected.

Consistency conditions have been known for decades, yet only few practical applications have been demonstrated. State-of-the-art often assumes 2D parallel or fan-beam geometries in a perfect circle around the object. Extension of these findings to flat-panel detector geometry are not straight-forward. Meanwhile, however, practical applicability in flat-detector computed tomography has been demonstrated for a set of pairwise conditions known as epipolar consistency (EC). Their advantage is that they can be applied, in principle, to any two 2D projection images.

This thesis first gives a brief introduction to data consistency conditions in two and three dimensions, providing a context for the main part of this work. The reader is then introduced to projective geometry of real two- and three-space and the geometry of X-ray imaging. This provides the mathematical tools for a derivation of the novel epipolar consistency conditions and demonstrates the connection to well-understood computer vision tasks. Three flavors of a metric to measure epipolar inconsistency in two images are suggested and a framework for motion compensation is introduced. Finally, the metric is used for motion correction in three applications of FDCT imaging. First, an unknown object under fluoroscopy is tracked relative to a small set of reference views. Second, respiratory and cardiac motion in rotational angiography is estimated. And third, the alignment of two computed tomography acquisitions is estimated from their raw data.

Kurzfassung

Zwei Röntgenbilder von einem starren Objekt zeigen zwar unterschiedliche Ansichten, dennoch kann redundante Information in solchen Projektionen identifiziert werden. Man spricht dabei von Konsistenzbedingungen. Diese sind wie eine Prüfziffer automatisch in den Daten enthalten. Echte Aufnahmen gehen allerdings aus einem Messprozess hervor, der ungenaue geometrische Scannerkalibrierung, physikalische Effekte, wie Strahlaufhärtung oder Streustrahlung, oder in manchen Anwendung Patientenbewegung mit sich bringt. Diese Effekte können als Abweichungen von theoretisch redundanter Information beobachtet und zu einem gewissen Grad korrigiert werden.

Konsistenzbedingungen sind schon seit Jahrzehnten bekannt, doch gibt es nur wenige praktische Anwendungen. Im Stand der Technik wird oft von 2D parallel oder Kegelstrahlgeometrie entlang eines perfekten Kreises ausgegangen. Die Erweiterung solcher Erkenntnisse auf Flachdetektorgeometrie ist jedoch nicht direkt übertragbar. Inzwischen wurde jedoch die praktische Anwendbarkeit auf Flachdetektor Computed Tomography von einer Menge von paarweisen Bedingungen gezeigt, die als epipolare Konsistenz bekannt geworden sind. Ihr Vorteil liegt darin, dass sie prinzipiell auf zwei beliebige Bilder angewendet werden können.

Diese Arbeit gibt einen Einblick in Konsistenzbedingungen in zwei und drei Dimensionen, um den Kontext für den Hauptteil der Arbeit zu geben. Der Leser wird in die projektive Geometrie des reellen zwei- und dreidimensionalen Raumes eingeführt und damit in die Geometrie der Flachdetektor-Röntgenbildgebung. Dies stellt das mathematische Rüstzeug zur Verfügung, um die neuen epipolaren Konsistenzbedingungen herzuleiten und den Zusammenhang zu wohlbekannten Arbeiten dem maschinellen Sehen zu zeigen. Es werden drei Varianten vorgeschlagen, um die epipolare Inkonsistenz zweier Bilder zu beziffern und ein Framework für die Bewegungskompensation wird eingeführt. Abschließend wird diese Metrik zur Bewegungskorrektur in drei Anwendungen Flachdetektortomographie benutzt. Erstens wird die Position eines unbekannten Objekts relativ zu einer kleinen Menge von Referenzbildern bestimmt. Zweitens wird die Atmungs- und Herzbewungung in der Rotationsangiographie geschätzt. Drittens wird die geometrische Ausrichtung von zwei Computed Tomography Aufnahmen direkt mit deren Rohdaten geschätzt.

Acknowledgements

Without the support of many friends, my family, colleagues, teachers, and mentors this thesis would have been impossible.

I would like to express my gratitude to Prof. Dr.-Ing. habil. Andreas Maier, not only for the supervision of my Ph.D. but for enabling it. Without him and Dr.-Ing. Christian Rieß, I would have left the university years ago and I have a lot of respect for their work.

The next person I must name is Prof. Dr. Nassir Navab. His support for my Ph.D. is ongoing, although I have only known him as a professor in my bachelor and master studies. He was an essential source of curiosity and motivation throughout and a teacher of scientific methodology. I thank Dr. rer. nat. Oliver Kutter, for the supervision during my studies in Munich and Dr. rer. nat. Mathias Wieczorek for our pleasant cooperation as HiWis. While in Princeton, NJ, I had the privilege of working with Dr. Ali Kamen and particularly Dr. Wolfgang Wein, both of whom lent me a great deal of time and freedom for furthering my experience and interests. I should add Prof. Dr. Dr. Jürgen Richter-Gebert as my geometry professor, who perfectly understands transporting mathematical concepts and ideas, even to novices.

I would like to thank Prof. Dr.-Ing. Joachim Hornegger for bringing me to Erlangen. The Pattern Recognition Lab has been the most pleasant workplace for 6 years, not least because of my office mates Dr.-Ing. Martin Kraus, Dr.-Ing. Thomas Köhler and Katharina Breininger. I would also like to thank other chair dudes and dudettes for the scientific discussions and friendship. First of all, Dr.-Ing. Martin Berger for creative discussions and help with the DFG proposal, but also Dr.-Ing. Christian Rieß, Dr.-Ing. Vincent Christlein, Dr.-Ing. Johannes Jordan, Dr.-Ing. James "Chet" Sanders, Dr.-Ing. Christine Martindale, Martin Koch and especially those I have actively worked together with, Tobias Würfl, Prof. Dr.-Ing. Mathias Unberath, Dr.-Ing. Jian Wang and Lina Felsner. Such a list cannot be complete. I thank Kristina Müller for her patience with scientists' filing of paperwork.

A crucial encounter for me was Dr. Nicole Maass, who gave me the idea for epipolar consistency in the first place. I thank her for the detailed discussions and constructive practical input. Although I had only one short opportunity to visit Grenoble, France, I gained a great impression of the solid work by Prof. Dr. Rolf Clackdoyle and Prof. Dr. Laurent Desbat, and I would like to particularly thank Dr. Jérôme Lesaint for his insights and invaluable exchange.

Erlangen, Nov 27th 2019 André Aichert

"I believe we are lucky. If there were just one fewer dimension we would have to close shop."
Reproduced with permission by Joscha Sauer.

Contents

CHAPTER 1

Introduction

Computed tomography (CT) reconstructs a three-dimensional (3D) object from its two-dimensional (2D) projection images. Projection images can be from either a transmission-only (e.g. X-ray) or emission-only modalities (e.g., single-photon emission CT in nuclear medicine). This section begins by introducing CT reconstruction and discussing how the reconstruction process is prone to various artifacts in the reconstructed images. The concept of data redundancy of multiple projection images of the same object is introduced which leads to mathematical consistency conditions. The main topic of this thesis is then presented as the estimation of motion using a certain type of consistency conditions. The author's contribution to this field of research is briefly listed, and finally, the contents of each chapter of this thesis are briefly summarized.

1.1 X-Ray Imaging

The discovery of X-rays in 1895 by W. C. Röntgen was equally important for physics and medicine, as the new radiation allowed for a glimpse inside a living organism. It was found that X-rays similarly behave in visually opaque materials to visible light in a semi-transparent solution. An X-ray projection is a transmission image, which means that rays traverse the object as they are attenuated depending on the material of the object. The object is modeled as a function f which assigns an absorption coefficient to each point in space. Each X-ray can be understood as accumulating absorption irrespective of the location along the ray (i.e., the depth). X-rays are emitted in the so-called focal spot. In this thesis, we assume a point-shaped X-ray source i.e., the focal spot is of negligible size compared to the distance from the object. Images are produced on a detector located on the opposite side of the object being imaged. We consider the case where the detector is a flat-panel detector (FDCT) which is planar.

The source-detector geometry follows the same geometry as a pinhole camera. The focal spot of the X-ray source typically has a negligible size and its can be assumed that all rays intersect in a single point. This point takes the role of the pinhole, i.e. center of projection and corresponds to the camera center of a usual photo camera. The image is recorded on the X-ray detector, which is a flat rectangle in case of FDCT. It takes the role of the image plane.

With the aforementioned assumptions, the geometry is exactly the same as for usual visual light cameras. However, visual light cameras can reconstruct points on the surface of opaque objects seen from two views, while X-ray imaging, in general, cannot. Objects appear translucent, and each pixel shows an overlay of intensities from many parts of the object. In the case of X-ray imaging, the object f can still be reconstructed under certain conditions [Tuy 83, Metz 02], from a large number of projections of a moving X-ray source. In 1973, the radiation was first used for tomographic reconstruction [Houn 73] which has since developed into the enabling technology for a wide range of transmission-based 3D imaging modalities. Tomography refers to the process of imaging slices through an object. Reconstruction is the inverse problem to the projection caused by X-ray or Radon transforms, respectively. The first X-ray (CT) scanners built in the 1970ies used parallel geometries [Corm 63, Houn 73] which would record parallel projections of a plane through a rotating object, i.e. the 2D Radon transform and solve the problem using algebraic methods. In order to speed-up acquisition, the systems soon moved to fan-beam and finally cone-beam geometries. The latter exists for both planar and curved detectors which are, however, easily transformed into one another. A treatise of the history and physics of X-ray tomography can be found in a book by T. Buzug [Buzu 08].

Flat-panel detectors are common in C-arm fluoroscopy and angiography systems, onboard imaging systems in radiation therapy, mobile C-arms, tomosynthesis, and many other imaging systems. A visualization of the geometry of one such system is shown in Figure 1.1. Most spiral CT scanners which allow for fast 360° rotation use curved detectors instead. Mathematically, this can be mapped to the planar case by a change of variables. While reconstruction is not the primary focus of this work, most essential related work is rooted in analytic reconstruction literature, where consistency conditions have been known early on [Ludw 66]. The most common cone-beam reconstruction algorithm today, by Feldkamp, Davis and Kress (FDK) [Feld 84], is a member of the "filtered backprojection" family of analytic reconstruction algorithms for circular trajectories. Its main advantage lies in its simplicity and computational efficiency, although more computationally complex and flexible iterative approaches are starting to catch on [De M 09].

1.2 Artifact Reduction in Computed Tomography

In the context of X-ray imaging, reconstruction algorithms usually assume a perfect Lambertian absorption along straight rays (explained later in Equation 2.1). Real scans violate this assumption for various reasons, for example by ignoring physical effects which change the direction of electromagnetic radiation (e.g. scattering) or by ignoring changes in the spectrum of an X-ray beam (e.g. beam-hardening of non-monochromatic radiation) [Maie 18]. In addition, the scanner or turntable motion

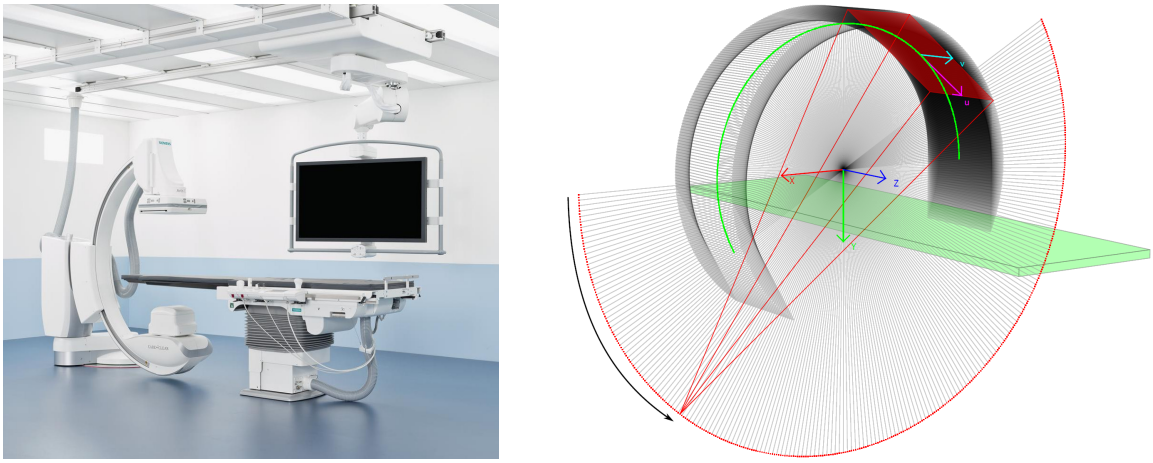

Figure 1.1: Left: A typical clinical C-arm CT scanner for interventional use. Image adapted from Maier et al. [Maie 18]. Right: Visualization of a CT trajectory. This trajectory represents a 20 second short-scan of a Siemens Artis Zeego clinical C-arm scanner. The red dotted line is the source trajectory, the green arc represents the trajectory of the center of the detector. One particular source and detector are highlighted as a red pyramid enclosing the volume which is projected to the image. In this thesis, we use u and v axes for the 2D detector coordinate system, while X,Y and Z represent the 3D world coordinate system. The green box represents the table on which a patient might lie.

must be calibrated [Stro 03, Aich 18a], which is not always accurate and sometimes invalidated by irreproducible motion. The detector of a table-top CT system may be misaligned with respect to a turntable [Leeu 18, Wick 12, Von 04], while a C-arm may be subject to irreprducible wobble due to acceleration and inertia. Especially robotic C-arm systems become more and more flexible [Maie 11] but their odometry may not be accurate enough to allow for CT reconstruction by themselves [Thur 15]. In medical applications, a breathing patient [Breh 12] or the beating heart [Laur 06] introduce additional non-rigid motion between individual images. Data may be missing due to a limited field-of-view and truncation (i.e. the object is not fully visible on the detector) [Ohne 00, Kold 10, Xia 15] or photon starvation (i.e. the density of materials cannot be measured because all radiation is absorbed) [Chan 17] and over-exposure [Raus 16] and angular under sampling may present a problem for fast scanning protocols [Manh 13]. All of these effects lead to artifacts which degrade the quality of reconstructed images.

It is desirable to estimate motion from the patient or inaccuracies of scanner motion, as well as estimate the beam-hardening or scatter effects and missing parts of objects etc. directly from acquired data. In tomography, such methods typically aim at improving the image quality of reconstructed methods and are known as artifact reduction. Most artifact reduction methods in FDCT rely either on heuristics [Ohne 00], prior information [Kold 10], additional sensors [Laur 06, Raus 16], or iterative procedures [Chen 08, Pane 08, Prum 09, Breh 12, Manh 13, Mull 14, Chan 17], to name a few examples. This work, in contrast, uses redundant information [Debb 13, Lang 13] on the projections for artifact reduction, especially motion estimation.

1.3 Redundancy in X-ray Projections

Two or more X-ray projections of the same object are not independent. Redundancies between multiple projections from different directions can be expressed as a set of mathematical conditions. These redundancies have to be taken into account in many reconstruction algorithms, for example [Clac 94], so as to weight the data correctly. Nevertheless, the redundant information can also be used to verify the acquisition process. Not unlike a naturally occurring checksum, data consistency conditions (DCCs) allow for the observation of inaccuracies in the raw data and to correct certain systematic effects. Especially in earlier work, DCCs are also called range conditions of the projection operator. In this context, the projection operator is understood as the function mapping from a representation of the object to the entire projection data of an acquisition, i.e. not just a single image. Imagine an acquisition of an object continuously rotating in a circle. Naturally, its projection on the detector has to follow a continuous curve as well (in fact, a sinosoid) and it cannot arbitrarily jump from one location to another between individual time points.

DCCs have been applied successfully in the context of positron emission tomography (PET), a nuclear imaging modality [Defr 12] and much earlier work can be found in this context. Most work about DCCs such as Helgasson-Ludwig consistency conditions (HLCC) [Ludw 66], discussed later in Section 2.3.1, have limitations for practical applicability because they make strong assumptions, specifically on the projection geometry. In Figure 1.2 are two of the most common 2D projection geometries for a perfect circular scan which can also be found in much of the theoretical work on DCCs. However, not all methods formulated under one set of assumptions can be adapted to suit another set. This is especially true for FDCT, where the geometry is a 3D cone-beam and the trajectory is usually only approximately an arc of a circle. For example, methods exist for motion compensation [Yu 07] but assume a fan-beam geometry. If they were applied to a cone-beam scan, only a small fraction of data would actually be considered. The classical HLCC and their connection to Fourier properties of the Radon transform have been used for data extrapolation [Xia 17, Preu 15] but their extension to 3D is ad hoc. Only few works apply to cone-beam geometries directly [Clac 13b, Clac 16, Patc 02, Levi 10] and are only starting to become applicable to real FDCT data. A heuristic extension of the Fourier consistency conditions to 3D has been investigated for motion correction for knee-data [Berg 17]. Patch et al. have used John's equation to synthesize projections [Patc 02]. This thesis addresses, specifically, a relatively simple pairwise consistency condition which has the strong advantage of being quite generally applicable [Debb 13]. It is based on redundancies observed in a type of analytic reconstruction algorithm [Clac 94] which measures certain quantities on 3D planes directly via line integrals in the projection images. Debbeler et al. [Debb 13] use this property on what we now understand to be epipolar lines for calibration correction in FDCT. In the last few years, a similar method collectively referred to as epipolar consistency (EC) has been shown to be applicable quite generally to any two X-ray images and effectively reduce reconstruction artifacts in several calibration correction scenarios in turntable CT [Leeu 18, Lesa 17b] and has been applied to other applications in FDCT as well.

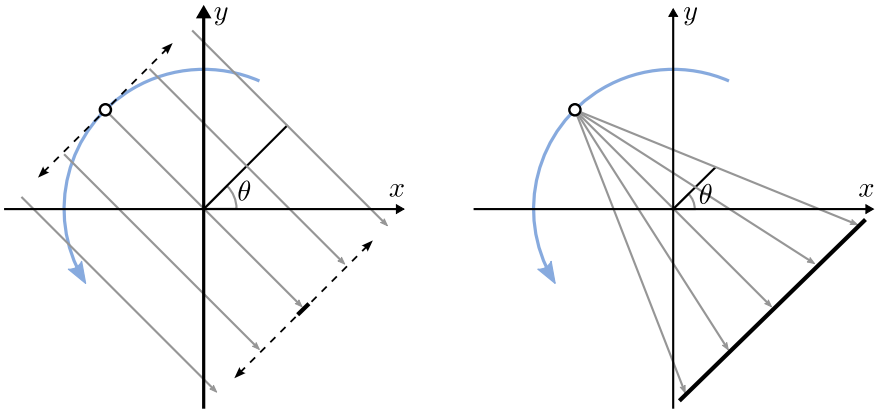

Figure 1.2: Visualization of parallel (left) and fab-beam (right) geometries (reproduced from Maier at al. [Maie 18]).

This thesis develops epipolar consistency and investigates several novel applications in motion correction.

1.4 Contributions

The following section briefly names the contributions made by the author of this thesis to the state-of-the-art. The most relevant publications which form the basis for this thesis are highlighted in blue. The focus of the thesis is epipolar consistency. After an initial publication by Debbeler et al. [Debb 13] of a pairwise consistency condition based on Radon intermediate functions [Clac 94], we established the connection to the well-understood epipolar geometry used in computer vision for stereo-vision.

[Aich 14] A. Aichert, N. Maass, Y. Deuerling-Zheng, M. Berger, M. Manhart, J. Hornegger, A. Maier, and A. Doerfler. "Redundancies in X-ray images due to the epipolar geometry for transmission imaging". In: *4th International Conference on Image Formation in X-Ray Computed Tomography*, pp. 333–336, 2014

The work was extended by a derivation of epipolar consistency from Grangeat's theorem and epipolar geometry. The work directly implicates which parameters can - and cannot - be estimated in a stable manner. By considering pairs of projections independently, the method becomes easier to understand and implement.

[Aich 15a] A. Aichert, M. Berger, J. Wang, N. Maass, A. Doerfler, J. Hornegger, and A. K. Maier. "Epipolar consistency in transmission imaging". *IEEE Transaction on Medical Imaging*, Vol. 34, No. 11, pp. 2205–2219, 2015

This allowed us to build an efficient GPU implementation. Most of the geometry can be reduced to just two small matrix multiplications and evaluation of inconsistency becomes mostly a sampling process. The implementation enables application to large data sets and also swift evaluation for few views. The C++/CUDA source code has been made publicly available (GitHub: `https://github.com/aaichert`)

for other research groups to reproduce experiments and quickly adapt the methods to their applications and data.

[Aich 16] A. Aichert, K. Breininger, T. Köhler, and A. K. Maier. "Efficient Epipolar Consistency". In: *4th International Conference on Image Formation in X-Ray Computed Tomography*, pp. 383–386, 2016

We later established the connection between epipolar geometry and an existing order-0 consistency condition [Levi 10] and the derivation of epipolar consistency directly from John's Equation, which is explained in Section 2.4.1. Combined with work by Lesaint et al. [Lesa 16] we can differentiate between three flavors of epipolar consistency: first, a weighted integral over epipolar lines, second, a derivative orthogonal to integrals over epipolar lines, and third, the same condition with the derivative replaced by a ramp filter.

[Aich 18b] A. Aichert, J. Lesaint, T. Würfl, R. Clackdoyle, L. Desbat, and A. K. Maier. "Stereo Rectification for X-ray Data Consistency Conditions". In: *5th International Conference on Image Formation in X-Ray Computed Tomography*, pp. 198–201, 2018

The reason for our interest in epipolar consistency, specifically, its general applicability. Since epipolar geometry applies to any two X-ray images, epipolar consistency can, in principle, be used in any trajectory. We went so far as to say that the consistency conditions can also be used in scenarios not directly related to computed tomography. A new application of consistency conditions to tracking unknown objects in fluoroscopic image sequences was presented. Notably, the 3D pose of an object can be determined from just a few reference projections, although the object itself is not known, and there is not enough data to reconstruct it. The major weakness of the method is that inconsistencies from truncation and motion cannot be separated.

[Aich 15b] A. Aichert, J. Wang, R. Schaffert, A. Dörfler, and J. Hornegger. "Epipolar Consistency in Fluoroscopy for Image-Based Tracking.". In: *British Machine Vision Conference (BMVC)*, 2015

This thesis contains a contribution in Section 5.3 not otherwise published, where EC is used for the first time to register two FDCT scans based on the raw data domain. In addition, the author made considerable contributions to the following research on motion compensation in rotational angiography, much of which is based on epipolar consistency. We introduce virtual digital subtraction angiography (vDSA) as a means to address inconsistencies arising from truncation enabling heart motion estimation using consistency conditions. We suggest methods for automatic gating and motion estimation and evaluate the methods based on phantom and real data. In this context, we also compared performance of epipolar consistency and Fourier consistency and investigated graph-based optimization strategies [Fels 17] to better handle recurring motion patterns (such as the beating heart). We also attempted to use consistency as additional information to improve vessel segmentation [Unbe 16b].

[Unbe 16c] M. Unberath, A. Aichert, S. Achenbach, and A. K. Maier. "Virtual Single-frame Subtraction Imaging". In: *4th International Conference on Image Formation in X-Ray Computed Tomography*, pp. 89–92, 2016

[Unbe 17a] M. Unberath, A. Aichert, S. Achenbach, and A. K. Maier. "Consistency-based respiratory motion estimation in rotational angiography". *Medical Physics*, Vol. 44, No. 9, 2017

[Unbe 17b] M. Unberath, M. Berger, A. Aichert, and A. K. Maier. "Fourier Consistency-Based Motion Estimation in Rotational Angiography". In: *Bildverarbeitung für die Medizin 2017*, pp. 110–115, Springer, 2017

Contributions were made to a lesser extent to research on artifact correction algorithms related to various consistency conditions and modalities, including motion correction in fan- and cone-beam geometries using Fourier properties of the sinogram [Berg 17], applications of motion and calibration correction using epipolar consistency conditions [Maas 14, Bier 17, Grul 15]. Epipolar consistency has meanwhile been used for beam-hardening and scatter correction algorithms [Wurf 18, Hoff 18]. Minor contributions were made to volume-of-interest imaging using consistency conditions [Xia 17].

The author has also contributed to medical imaging in a wider context, not directly related to this thesis. A geometric calibration algorithm for FDCT systems was patented and published [Aich 18a] and a joint calibration and motion correction algorithm was suggested [Sybe 17]. In medical augmented reality, the author investigated tracking algorithms [Aich 12a], visualization [Kutt 08, Wiec 10] and user perception [Blum 10, Wiec 11, Aich 12b].

1.5 Organization of this Thesis

Chapter 2 provides an introduction to data consistency conditions in parallel 2D and cone-beam geometry. After mathematical introduction of the projection operators in Section 2.1, a discrete representation as a system matrix will be given in Section 2.2. Consistency conditions appear as the image and null-space of this matrix and the example nicely explains how inconsistent information in projections is such that cannot be generated by projection of any object. A few examples of DCCs in continuous Radon and X-ray transform are then given in Sections 2.3.1 with the HLCC, Section 2.3.2 with the Fourier properties of the Radon transform and Section 2.4.1 with John's equation. Section 2.4.2 then derives a simple pairwise condition from John's equation, which is the first type of epipolar consistency. The condition will be extended and applied from Chapter 4 onwards.

Chapter 3 investigates the geometry of two central projections to a planar detector in terms of real projective geometry. The concept of homogeneous coordinates will be introduced for two and three dimensions and be applied to the geometry of point and lines in two-space, as well as points and planes in three-space in Sections 3.1.

Special care will be taken to elegantly express lines in space, since these are not only the basic element of the imaging process of pinhole cameras in Section 3.2 but are also essential for understanding the details of epipolar geometry in Section 3.3. This provides the geometric tools used in the algorithms of the following chapters.

Chapter 4 introduces epipolar consistency and derives a quality metric from it. In Section 4.1 projective geometry will be used to generalize the consistency condition already discussed in Section 2.4.2 to almost any pair of projection images. Two other kinds of epipolar consistency based on the Radon transform of cone-beam projection images are presented and simplified for efficient implementation in Section 4.2. Section 4.3 presents an efficient implementation of the metrics and Section 4.4 compares them on two exemplary real projections of a pumpkin. Finally, Chapter 5 will present applications of a metric based on epipolar consistency for motion estimation in fluoroscopy in Section 5.1, angiography in Section 5.2, as well as registration of computed tomography scans in Section 5.3. Chapter 6 presents a summary and an outlook of the whole thesis and concludes by motivating future research.

CHAPTER 2

Data Consistency Conditions

THE THEORETICAL MODEL of geometry and physics in CT impose constraints on these projection images. It is known that data consistency conditions (DCCs) also known as range conditions, describe mathematical redundancies in the projection data. These redundancies go back to the fact that each projection image is composed of line integrals passing through the same object, merely from different directions. The tomographic problem is well-understood and DCCs have been investigated, especially for parallel-beam geometries for more than 25 years [Clac 13b]. It has been shown that data consistency conditions can be used to correct for inaccuracies in the acquisition process. This section provides an introduction to 2D and 3D X-ray projection and its data redundancies. We begin by introducing the continuous and discrete representations of the X-ray projection operator. Data consistency conditions exist, because such operators have a limited range and two or more X-ray projections of the same bounded object are not entirely independent. We take a brief detour and represent tomographic projection and reconstruction discretely as a system matrix and its inverse. In this context the space of all possible tomographic projections is spanned by the image of said matrix, and projections in its null-space are inconsistent since no object exists that could produce them. Finally, we present established continuous formulations of data consistency for the case of 2D parallel projections and we derive a practical 3D cone-beam consistency condition for an X-ray source moving on a line.

2.1 Transmission Imaging

2.1.1 Notation

Throughout this work, we will write scalar values as lowercase Latin characters $a, b, c \dots$. These usually measure length, position or distance and exist in the real numbers $\mathbb{R}$ or a subset thereof. A special case are angles, which are denoted in Greek lowercase letters $\alpha, \beta, \gamma \dots$. Real vectors of two, three and more dimensions are denoted as bold italic lowercase letters $\boldsymbol{a}, \boldsymbol{b}, \mathbf{c} \dots$. We indicate unit vectors with an

additional $^\circ$ decorator, such as $\mathring{\boldsymbol{a}}, \mathring{\boldsymbol{b}}, \mathring{\mathbf{c}} \ldots$. Orthogonal vectors are indicated by a $^\perp$ decorator.

In this thesis, we sometimes consider the same physical object in three, two and even one dimension. In order to differentiate between two- and three-dimensional coordinate systems, we will refer to 2D coordinates of points by the u- and v-axes, while we refer to 3D coordinates by x-, y- and z-axes. Coordinates on a line or ray are denoted r, s or t, e.g. position along a ray, a linear detector variable or a linear translation. We try to follow a convention, by which the real coordinates of vectors use the same character (not set in bold) with an subset index indicating the component $a_0, a_1, a_2 \ldots$. These are always explicitly introduced and in some situations we resort to capital Latin characters, when there is a potential conflict with two- and three-dimensional objects. In those cases, the capital letters are components of the higher-dimensional vector. Matrices are written in bold capital Latin characters $\mathbf{A}, \mathbf{B}, \mathbf{C} \ldots$. The decorators $^\top$ and $^+$ denote vector and matrix transposition and the pseudo-inverse.

Finally, functional operators are written in calligraphic capital characters with explicit braces around the function they operate, notably the Fourier, Radon and X–ray transforms $(\mathcal{F}), (\mathcal{R}), (\mathcal{X})$. A function after Fourier transform is decorated with a hat and spectral variables are denotes in corresponding Greek letters. More notation and conventions will be introduced in the following sections. There is a complete nomenclature lists on page 101 after the conclusion.

The following introduction into tomographic projection and consistency uses several different geometries. Again, we introduce some specific notation to differentiate between these. A summary of symbols used in this chapter is given in Table 2.1. In all situations, we will model the object as a function mapping from space (in the geometric sense) to an attenuation value. In the simplest case, we consider the values along a single ray $f_{ray}(r)$, and based on the distance of protons traveled along that ray $r \in \mathbb{R}^+$. We go on to consider a plane through the object which is written with a function taking two arguments $f^{2D}(u, v)$. A special instance of this case is $f^\bullet(u, v)$, which represents a single point in the plane. Its projection $p^\bullet(\alpha, s)$ will prove valuable in theoretical considerations. Most of the thesis, however, addresses objects in the 3D world, for which we simply write $f(x, y, z)$.

2.1.2 The X-ray Transform

A simplistic model for X-ray absorption states that an initial intensity of radiation I_{tube} is absorbed along the ray path through an object of varying attenuation $f_{ray}(r)$ by an exponential fall-off with the distance traveled r along the ray, the so-called Lambert(-Beer) law

$$I = I_{\text{tube}} \cdot \exp\left(-\int_0^\infty f_{ray}(r)\ \mathrm{d}r\right). \tag{2.1}$$

In practice, we will model this imaging process as a projection of a three-dimensional object function $f : \mathbb{R}^3 \mapsto \mathbb{R}$ which is twice continuously differentiable $f \in C^2(\mathbb{R}^3)$. A point-shaped X-ray source in position $\boldsymbol{c}$ projects the objects along straight rays to a planar detector at 3D location of a pixel $\boldsymbol{x}$. The Beer-Lambert law then holds for

Table 2.1: Summary of notation used in this chapter.

Decorators	
vector decor. $\mathring{}$	A unit vector in $\mathbb{S}^1$, e.g. $\mathring{\boldsymbol{a}} = (\cos(\alpha), \sin(\alpha))^\top$.
vector decor. $^\perp$	An orthogonal, e.g. $\mathring{\boldsymbol{a}}^\perp = (-\sin(\alpha), +\cos(\alpha))^\top$.
function decor. $\hat{}$	The (partial) Fourier transform.
Operators	
$(\mathcal{X}f)$	The X-ray transform.
$(\mathcal{R}f^{2D})$, $(\mathcal{R}f)$	The Radon transform of a 2D resp. 3D object function.
$(\mathcal{F})$	Fourier transform e.g. $\hat{f} = (\mathcal{F}f)$
Other	
$\hat{p}(\alpha, \sigma)$	1D Fourier transform of $(\mathcal{R}f^{2D})(\alpha, s)$ in only the second variable.
$f^\bullet(u, v)$	Point-shaped 2D object function.
$p^\bullet(\alpha,\ s)$	Projection of point-shaped object at angle α and detector var. s.
$\tilde{g}(\boldsymbol{c}, \boldsymbol{x})$	The normalized X-ray transform.
$\hat{g}(\boldsymbol{c}, \boldsymbol{\xi})$	1D Fourier transform of $\tilde{g}(\boldsymbol{c}, \boldsymbol{x})$ in only the second variable.

any ray through space, represented by a source position and point on the detector. Mathematically, we model the John or X-ray transform

$$(\mathcal{X}f)(\boldsymbol{c}, \boldsymbol{x}) \overset{\text{def}}{=} \int_0^1 f(\boldsymbol{c}(1-t) + t \cdot \boldsymbol{x})\ \mathrm{d}t. \tag{2.2}$$

A pixel measurement on a real X-ray detector, however, is not dependent on the distance of the pixel to the source. Let $\boldsymbol{r} = \boldsymbol{x} - \boldsymbol{c}$ denote the vector pointing from $\boldsymbol{c}$ to $\boldsymbol{x}$. We assume that f is zero everywhere except between our choices of $\boldsymbol{c}$ and $\boldsymbol{x}$. The X-ray attenuation recorded in a pixel is actually the normalized X-ray transform

$$\begin{aligned} -\ln\left(\frac{I}{I_{\text{tube}}}\right) &\overset{(2.1,2.2)}{=} \int_0^1 f\left(\boldsymbol{c} + r \cdot \frac{\boldsymbol{r}}{\|\boldsymbol{r}\|}\right)\ \mathrm{d}r \\ &= \|\boldsymbol{x} - \boldsymbol{c}\|\,(\mathcal{X}f)(\boldsymbol{c}, \boldsymbol{x}), \end{aligned} \tag{2.3}$$

where $\boldsymbol{r}\,\|\boldsymbol{r}\|^{-1}$ is the unit vector pointing in direction of the ray. In the following section, we will therefore consider the normalized X-ray transform in equation 2.2.

X-ray imaging is not the only imaging modality that abides by this equation in good approximation. Although this thesis covers X-ray imaging in particular, the results can be applied to any emission or transmission modality for the same acquisition geometry. Nuclear imaging [Defr 12, Bruy 02] and some applications in microscopy [Bran 13] are two other examples. The X-ray transform does not model all physical effects, most notably scattering. However, this will be addressed only later in this thesis.

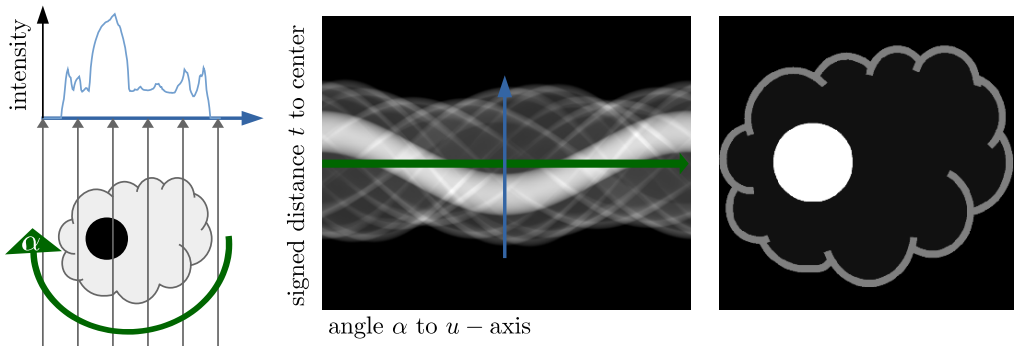

Figure 2.1: The 2D Radon transform. Left: Integration along parallel lines (light blue) given an angle α to the u-axis (represented by the curved arrow) for different distance t (green axis vector) produces the intensity profile on the top. Center: The Radon transform of the test object for $\alpha \in [0, 2\pi[$ and $t \in [-\frac{d}{2}, +\frac{d}{2}]$, where d is the diameter of the test object. Observe that the projection is symmetric for $\alpha \to \alpha + \pi$ and $t \to -t$. Right: The test object, which can be reconstructed from the Radon transform. The round bright feature produces a sinusoidal band in the Radon transform whose amplitude depends on the distance of the center of the feature to the rotation center.

2.1.3 The Radon Transform

In two dimensions, projection can be understood as a linear reduction of a planar object from different directions. Projection assumes the form of an integral operator, just like the X-ray transform in Equation 2.2. In two dimensions, the operator is more commonly referred to as the 2D Radon transform [Rado 17]. Let $f^{2D} : \mathbb{R}^2 \mapsto \mathbb{R}$ denote a two-dimensional object function, α be the angle of a line to the horizontal axis and t denote its signed distance to the origin, cf. Figure 2.1. Further let $\mathring{\boldsymbol{a}} = (\cos(\alpha), \sin(\alpha))^\top \in \mathbb{S}^1$ denote the line normal on the 2D unit circle $\mathbb{S}^1$ and $\mathring{\boldsymbol{a}}^\perp = (-\sin(\alpha), +\cos(\alpha))^\top$ its orthogonal. For brevity of notation, we use the symbol $\int$ without explicit limits to denote an integral over the whole domain, i.e. $-\infty$ to $+\infty$ for $\mathbb{R}$ rather than the antiderivative. The 2D Radon transform can be expressed in terms of line coordinates or with the dirac-impulse $\delta(\cdot)$ as denoted by the integral operator $(\mathcal{R})$ in several similar ways [Zeng 10]

$$(\mathcal{R}f^{2D})(\alpha, s) = \iint f^{2D}(u, v)\delta\left((u, v) \cdot \mathring{\boldsymbol{a}} - s\right) \mathrm{d}u\mathrm{d}v \tag{2.4}$$

$$= \int f^{2D}\left(s \cdot \mathring{\boldsymbol{a}} + t \cdot \mathring{\boldsymbol{a}}^\perp\right) \mathrm{d}s \tag{2.5}$$

$$= \int f^{2D}\left(s \cdot \cos(\alpha) + t \cdot \sin(\alpha),\ -s \cdot \sin(\alpha) + t \cdot \cos(\alpha)\right) \mathrm{d}t. \tag{2.6}$$

The point $s \cdot \mathring{\boldsymbol{a}}$ is the closest point on the line to the origin and $\mathring{\boldsymbol{a}}^\perp$ points in direction of the line. The formula describes the parallel projection of a rotating object onto a linear detector. A 2D Radon transform is frequently referred to as a *sinogram*, since a point-shaped object at coordinates $(u, v)^\top$ projects to a sinusoid curve $s(\alpha) = v \cdot \cos(\alpha) - u \cdot \sin(\alpha)$ in the detector variable s under rotation α. The Radon transform

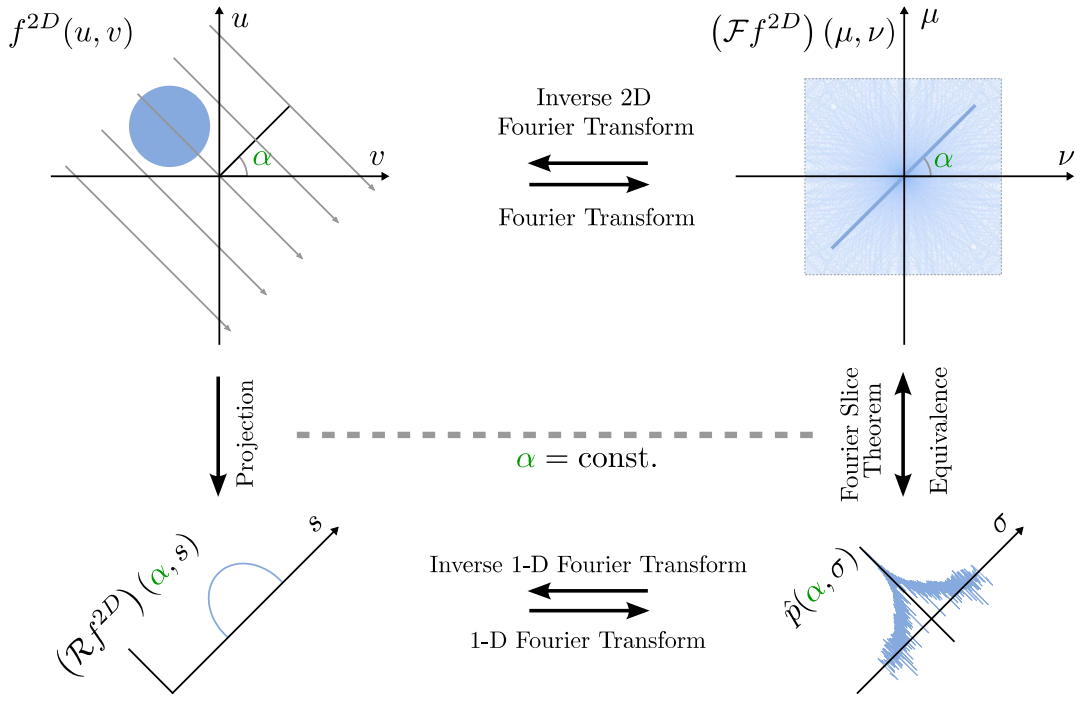

Figure 2.2: The Radon transform $(\mathcal{R}f^{2D})$ for a specific projection angle α (bottom right) is a projection of the object function f^{2D} (top left) to a 1D detector with variable s. The Fourier slice theorem states, that the 1D Fourier transform $\hat{p}(\alpha,\sigma)$ of that projection is identical to a central line through the 2D Fourier transform $(\mathcal{F}f^{2D})$ of the object. Figure adapted from Maier et al. [Maie 18].

is symmetric $(\mathcal{R}f^{2D})(\alpha,s) = (\mathcal{R}f^{2D})(\alpha+\pi,-s)$. In other words, opposing rays are identical. The Radon transform generalizes to n-dimensional spaces as the integral over all $n-1$ dimensional subspaces. For example, the 3D Radon transform collects all integrals over planes through the object. A plane is defined by normal $\mathring{\boldsymbol{n}} \in \mathbb{S}^2$ in the 3D unit sphere $\mathbb{S}^2$ and signed distance to the origin d. The 3D Radon transform is then given as

$$(\mathcal{R}f)(\mathring{\boldsymbol{n}},\, d) = \iiint f(x,y,z)\delta\left((x,y,z)\cdot\mathring{\boldsymbol{n}} - d\right)\mathrm{d}x\,\mathrm{d}y\,\mathrm{d}z, \tag{2.7}$$

or with two mutually orthogonal unit vectors $\mathring{\boldsymbol{n}}_s^{\perp}, \mathring{\boldsymbol{n}}_t^{\perp}$ that span the plane, with $\mathring{\boldsymbol{n}}_s^{\perp} \times \mathring{\boldsymbol{n}}_t^{\perp} = \mathring{\boldsymbol{n}}$

$$(\mathcal{R}f)(\mathring{\boldsymbol{n}},\, d) = \iint f\left(d\cdot\mathring{\boldsymbol{n}} + s\cdot\mathring{\boldsymbol{n}}_s^{\perp} + t\cdot\mathring{\boldsymbol{n}}_t^{\perp}\right)\mathrm{d}s\mathrm{d}t. \tag{2.8}$$

2.1.4 Relationship to the Fourier Transform

The 2D Radon transform is closely related to the Fourier transform $(\mathcal{F}_x)$. This relationship will be important because in Fourier space, the Radon transform has very specific properties. In addition, the relationship provides an approach to recover f^{2D} when only $(\mathcal{R}f^{2D})$ is known, i.e. a first reconstruction algorithm. For the frequency variable $\xi \leftrightarrow x$ we have

$$(\mathcal{F}_x h)(\xi) = \int h(x) e^{-2\pi i \xi x} \, \mathrm{d}x \;\leftrightarrow\; h(x) = \int (\mathcal{F}_x h)(\xi) e^{2\pi i \xi x} \, \mathrm{d}\xi, \tag{2.9}$$

or the Fourier transform in two dimensions for the spectral variables $\mu, \nu \leftrightarrow u, v$

$$(\mathcal{F} f^{2D})(\mu, \nu) = \int f^{2D}(u, v) e^{-2\pi i (\mu \cdot u + \nu \cdot v)} \, \mathrm{d}u\mathrm{d}v. \tag{2.10}$$

The relationship to the Radon transform becomes clear when considering the so-called generalized projection theorem [Lewi 83, Helg 84]. Let

$$p_w(\alpha) = \int (\mathcal{R} f^{2D})(\alpha, s) \cdot w(s) \, \mathrm{d}s \tag{2.11}$$

denote the integral of a projection weighted by a function $w(s)$ over the detector for a fixed angle α. Recall from Equation 2.4 that the s, t coordinate system is merely rotated from the u, v coordinate frame by angle α. We have

$$u = s \cdot \cos(\alpha) + t \cdot \sin(\alpha), \tag{2.12}$$

$$v = -s \cdot \sin(\alpha) + t \cdot \cos(\alpha), \tag{2.13}$$

and thus

$$s = u \cdot \sin(\alpha) + v \cdot \cos(\alpha). \tag{2.14}$$

The generalized projection theorem is simply the change of variables

$$p_w(\alpha) = \int \int f^{2D} \left(s \cdot \cos(\alpha) + t \cdot \sin(\alpha), \; s \cdot \sin(\alpha) - t \cdot \cos(\alpha) \right) \mathrm{d}t \cdot w(s) \, \mathrm{d}s \tag{2.15}$$

$$= \iint f^{2D} \left(u, v \right) \cdot w(u \cdot \sin(\alpha) + v \cdot \cos(\alpha)) \, \mathrm{d}u\mathrm{d}v. \tag{2.16}$$

By choosing $w(s) = e^{-2\pi i \sigma s}$ we see that $p_w(\alpha)$ becomes the Fourier transform $\hat{p} = (\mathcal{F}_s(\mathcal{R} f^{2D}))$ of a projection with angle α for the spectral detector variable $\sigma \leftrightarrow s$

$$\hat{p}(\alpha, \sigma) = \int \int f^{2D} \left(s \cdot \cos(\alpha) + t \cdot \sin(\alpha), \; s \cdot \sin(\alpha) - t \cdot \cos(\alpha) \right) \mathrm{d}t \cdot e^{-2\pi i \sigma s} \, \mathrm{d}s. \tag{2.17}$$

The change of variables in Equation 2.16 leads to a direction $(\sin(\alpha), \cos(\alpha))^\top$ in the 2D Fourier transform of the object $(\mathcal{F} f^{2D})$, which contains the 1D Fourier transform of the projection for angle α

$$\hat{p}(\alpha, \sigma) = \iint f^{2D} \left(u, v \right) \cdot e^{-2\pi i \sigma (u \cdot \sin(\alpha) + v \cdot \cos(\alpha))} \, \mathrm{d}u\mathrm{d}v \tag{2.18}$$

$$= \left(\mathcal{F} f^{2D} \right) \left(\sigma \sin(\alpha), \sigma \cos(\alpha) \right). \tag{2.19}$$

This is is also known as the central slice theorem or Fourier slice theorem. A naive way to recover a 2D object from its 1D projections might be to densely sample Fourier space and then apply an inverse Fourier transform [Zeng 10, Maie 18]. The concept is visualized in Figure 2.2.

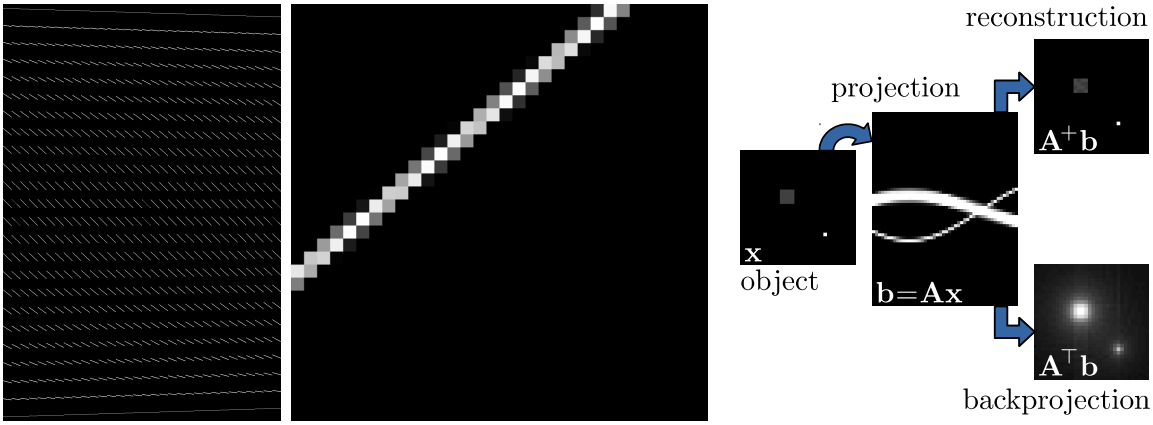

Figure 2.3: Left: Visualization of a system matrix $\mathbf{A}$ for $p = 24$ projections of a 32×32 pixel object onto a detector line of $m = 48$ bins. The matrix is sparse: all non-zero elements are shown in white. Each line describes the contribution of each of the $32 \cdot 32 = 1024$ pixels to a specific bin in the Radon transform. Center: Each row of the matrix contains 1024 elements, which can be re-arranged into a 32×32 grid and visualized as a line in the space of the object. There are a few different ways to define the contribution mathematically. For example, one may compute the intersection length of the line with each pixel. Right: Multiplication with $\mathbf{A}$ is a projection to a sinogram (i.e. discrete representation of the Radon transform) and a multiplication with its transpose $\mathbf{A}^\top$ is a backprojection (shown in the bottom right). The backprojection is a blurred version of the original object.

2.2 Algebraic Reconstruction and the System Matrix

This section is a brief excursion to algebraic reconstruction algorithms. We describe an algorithm to solve a 2D reconstruction problem using algebraic methods [Ande 84]. We do this in order to demonstrate that consistency conditions arise directly from linear algebra in this context. Algebraic reconstruction in practice offers the possibility to integrate regularizers and optimize for other properties (like smoothness [Ries 13]), which is an alternative and more common approach compared to using consistency conditions in many scenarios [Unbe 18, Leeu 18]. Suppose the object f^{2D} is represented discretely as a 2D grid of $n \times n$ real-valued pixels (we ignore the fact that the entries of $\mathbf{x}$ should be greater or equal to zero). We vectorize the image by re-arranging the elements into a vector $\mathbf{x} \in \mathbb{R}^{n^2}$. Let the k-th projection image consisting of m bins be represented by the vector $\mathbf{b}_k \in \mathbb{R}^m$, then projection to this image can be written as a matrix multiplication

$$\mathbf{b}_k = \mathbf{A}_k \mathbf{x}, \tag{2.20}$$

with an $m \times n^2$ matrix $\mathbf{A}_k$. Each element a_k^{ij} in $\mathbf{A}_k$ describes the contribution of a particular pixel $\boldsymbol{x}_j$ of the 2D image to the i-th bin of the k-th projection image. For example, one may use the intersection length of the j-th pixel with the ray $\mathbf{l}_k$ with angle $\alpha_k = \pi \frac{k}{p}$ centered in the i-th projection bin, although better models exist [De M 09].

The computed tomography problem for all $k = 0 \dots p-1$ projections can be written as the solution to the optimization problem in a minimal-least-squares sense

$$\mathbf{x}^\star = \underset{\mathbf{x}}{\operatorname{argmin}} \left\| \mathbf{A}\mathbf{x} - \mathbf{b} \right\|^2, \tag{2.21}$$

where

$$\mathbf{A} = \begin{pmatrix} \mathbf{A}_0 \\ \mathbf{A}_1 \\ \vdots \\ \mathbf{A}_{p-1} \end{pmatrix} \in \mathbb{R}^{pm \times n^2} \text{ and } \mathbf{b} = \begin{pmatrix} \mathbf{b}_0 \\ \mathbf{b}_1 \\ \vdots \\ \mathbf{b}_{p-1} \end{pmatrix} \in \mathbb{R}^{pm}. \tag{2.22}$$

Each ray only intersects very few pixels so $\mathbf{A}_k$ is a sparse matrix and a highly over-determined system of equations. Multiplication of $\mathbf{A}_k$ with a vectorized object $\mathbf{x}$ computes one column in the Radon transform of that object. The sparsity of the matrix $\mathbf{A}$ is visualized in Figure 2.3, left, for a small example $n = 32$, $m = 64$ and $p = 48$. On the one hand, each row is an n^2 vector may itself be visualized as a 2×2 grid in the space of the object as contribution weights, cf. Figure 2.3, center. It represents the relative amount by which each pixel contributes to a specific ray. Each column of $\mathbf{A}$ can be understood as a sinogram of one pixel in the object.

A straightforward solution to the reconstruction problem may be obtained using the pseudo-inverse

$$\begin{aligned} \mathbf{x}^\star &= \mathbf{A}^+ \mathbf{b} \\ &= \left(\mathbf{A}^\top \mathbf{A} \right)^{-1} \mathbf{A}^\top \mathbf{b}. \end{aligned} \tag{2.23}$$

The multiplication with $\mathbf{A}^\top$ is a backprojection into the domain of the object, as each row of $\mathbf{A}$. Backprojection is not the inverse operation to forward projection, since it introduces a blurring of the image, cf. Figure 2.4. We have encountered this property before when discussing the central slice theorem, notably Figure 2.2. As each projection records information through the zero-frequency, low frequencies are sampled more densely, putting a lower weight on high frequencies. In that sense, the term $\left(\mathbf{A}\mathbf{A}^\top \right)^{-1}$ in Eq. 2.23 can be understood as a sharpness filter applied after backprojection, not unlike *filtered back-projection* type analytic methods apply a high-pass filter to the sinogram, e.g. FDK.

The computation of the pseudo-inverse and even the storage of the system matrix is impractical in most real-world problems. Instead, several iterative algorithms may be used to solve for $\mathbf{x}$ [Gord 70, Ande 84]. In the following, we present a toy problem for which explicit storage of the system matrix $\mathbf{A}$ and solution using standard QR or singular value decomposition (SVD) matrix decomposition is possible. In order to gain some insights into the space of possible projections $\mathbf{b}$ [Liu 17], suppose we could actually compute the SVD

$$\mathbf{A} = \mathbf{U}\mathbf{\Sigma}\mathbf{V}^\top, \tag{2.24}$$

with $\mathbf{\Sigma} \in \mathbb{R}^{pm \times n^2}$ diagonal, $\mathbf{U} \in \mathbb{R}^{pm \times pm}$ and $\mathbf{V} \in \mathbb{R}^{n^2 \times n^2}$ both orthogonal. Provided that the matrix $\mathbf{A}$ has full column rank we may compute the pseudo-inverse

$$\mathbf{A}^+ = \mathbf{V} \cdot \mathbf{\Sigma}^{-1} \cdot \mathbf{U}^\top. \tag{2.25}$$

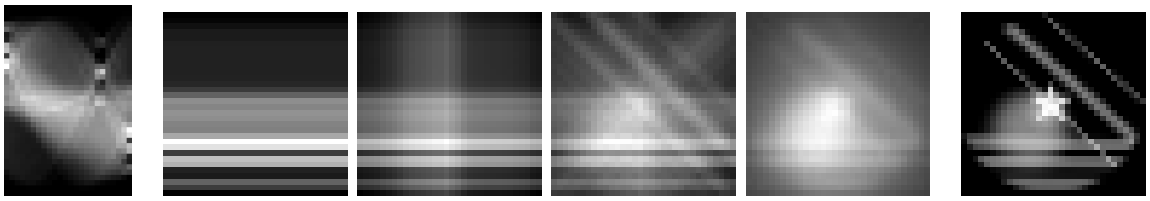

Figure 2.4: Algebraic reconstruction of a toy problem. Left: Sinogram for 32 projections. Right: Reconstruction from that sinogram. In between: Backprojections using 1,2,4 and 32 (all) equally-spaced projections of the sinogram (left). Backprojection introduces a low-pass filter on the image. The ground truth is not shown, since it is indistinguishable from the reconstruction result (right).

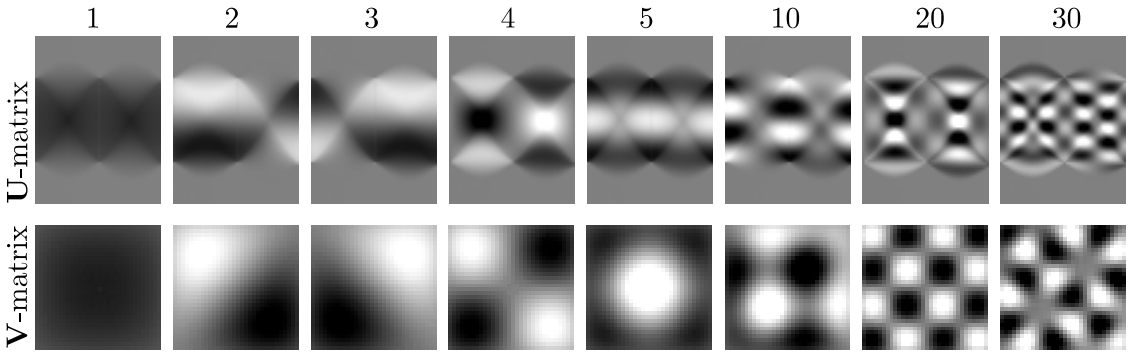

Figure 2.5: Singular value decomposition of the system matrix. Select columns from the **U** matrix (top) and **V** matrix (bottom). Columns from left to right 1-5, 10, 20 and 30. The sinograms on the top are projections (up to scale) of the objects on the bottom. The SVD thus provides an orthogonal basis of both object and sinograms. Note that the **U** matrix has $p \cdot m$ columns, which is considerably more than the **V**-matrix with only n^2 columns. Several sinograms from the null-space (i.e. columns $> n^2$ are shown in Figure 2.6.

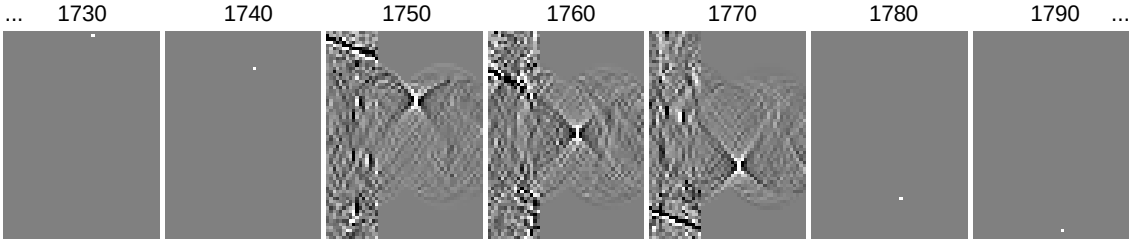

Figure 2.6: Singular value decomposition of the system matrix. Columns $n^2 + 1$ onward of the **U** matrix are in the null space of backprojection. When reconstructed or backprojected, these pseudo-sinogams yield an empty image. Therefore $\mathbf{b} \neq \mathbf{A}\mathbf{A}^{+}\mathbf{b}$. In fact, no object exists, which would produce these projections and they are not actually sinograms. In addition, their singular values are zero and any rotation within the null-space can be applied to all of these vectors. The author supposes that the left pm columns look different from the remaining column is an artifact of the specific orthogonalization algorithm using in the implementation of the singular value decomposition.

By multiplication of $\mathbf{A}^+$ with an observed projection $\mathbf{b}^\star$ we can then reconstruct an object $\mathbf{x}^\star$ which best explains the data w.r.t. the L_2-norm

$$\mathbf{x}^\star = \mathbf{A}^+\mathbf{b}^\star. \tag{2.26}$$

In Figure 2.4, we present one such reconstruction (right) from a sinogram (left). In practice, some form of regularization would be applied to reduce noise. The large singular values are related to low image frequencies [Liu 17], cf. Figure 2.5, so one possibility is to truncate small singular values in the SVD. In our example, we have such a coarse discretization of the object that this is not an issue.

Both image and null-space of $\mathbf{A}$ and its pseudoinverse $\mathbf{A}^+$ are spanned by column vectors of $\mathbf{V}$ and $\mathbf{U}$, respectively. If $\mathbf{b}$ is a perfect sinogram, that means an object $\mathbf{x}$ must exist, such that $\mathbf{b} = \mathbf{A}\mathbf{x}$ holds exactly. However, if $\mathbf{b}$ is in fact measured data, it may be affected by noise and other errors. In such a case, the singular value decomposition in Equation 2.24 tells us which parts of the measurement will influence the reconstruction and another part $\tilde{\mathbf{b}}$ which does not. Since $\tilde{\mathbf{b}}$ cannot be explained by a sinogram, we can express the measured data as $\mathbf{b}^\star = \mathbf{b} + \tilde{\mathbf{b}}$ such that

$$\mathbf{A}^+\tilde{\mathbf{b}} = \mathbf{0}. \tag{2.27}$$

The last $pm - n^2$ rows of $\mathbf{U}$ span the null-space of $\mathbf{A}^\top$, some of which are visualized in Figure 2.6. While adding a multiple of any vector $\tilde{\mathbf{b}}$ in the null-space to given projection data $\mathbf{b}$ changes neither the backprojection nor the reconstruction, it does introduce a residual in the L_2 sense

$$\epsilon = \|\tilde{\mathbf{b}}\| = \|\mathbf{b}^\star - \mathbf{A}\mathbf{x}^\star\|\,. \tag{2.28}$$

We say that the projection data $\mathbf{b}^\star$ is inconsistent and mean that $\mathbf{b}^\star$ is not a valid sinogram as defined by the system matrix $\mathbf{A}$. The residual ϵ can be seen as a metric for the amount of inconsistency in an L2 sense. Other metrics of consistency may be defined and the rest of this thesis addresses ways of measuring inconsistency. Data consistency conditions in terms of the range of a continuous projection operator, such as the X-ray or Radon transform from Equation 2.2 and 2.4 work in a similar way. The following section investigates analytical properties which must be fulfilled by projection data to be explainable by a reconstructed object function. We will achieve this without actually computing a reconstruction.

2.3 Consistency Conditions and the Radon Transform

2.3.1 Helgason-Ludwig Consistency Conditions

This section briefly presents one of the most common formulations of DCCs called Helgason-Ludwig Consistency Conditions (HLCC) [Helg 84, Ludw 66] which are based on the 2D Radon transform in Equation 2.4. These have been shown to be a "full set of conditions" in the sense that they are both necessary conditions for sinogram and sufficient to describe sinograms. In Section 2.2 it was observed that the discrete projection operator has a limited range. In other words, perfect projections

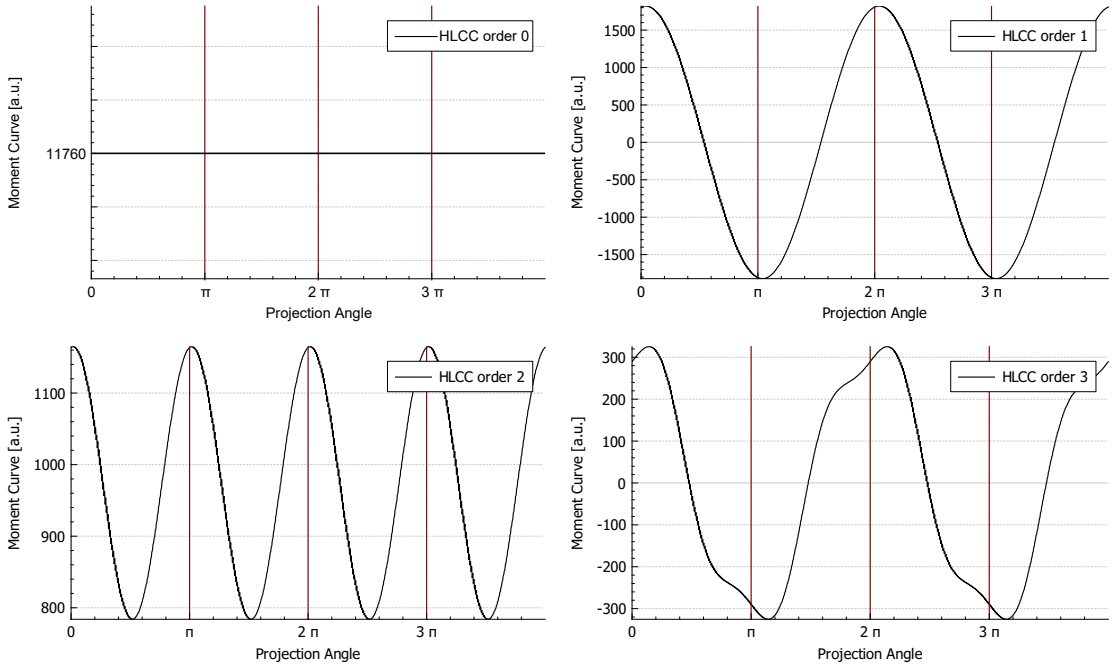

Figure 2.7: Moment curves $p_m(\alpha)$ extracted form the Radon transform shown in Figure 2.1. HLCC state that order 0 is a constant corresponding to the total mass of the object (top left). Order 1 (top right) is a sinusoid, which can be understood as the projection of the center of mass. Accordingly, order 2 and 3 are trigonometric polynomials of degree 2 (bottom left, even) and 3 (top right, odd) in projection angle θ. Observe the periodicity and symmetry $(\alpha, s) \leftrightarrow (\alpha + \pi, \pm s)$ for even respectively odd trigonometric polynomials.

are over-determined and must therefore fulfill certain constraints. HLCC can be seen as a continuous representation of the same condition for the 2D circular case.

From this point on, we will use the weighting function $q_m(s) = s^m$ instead of $w(s)$ in the generalized projection theorem of Equation 2.16. The function $p_m(\alpha)$ is then called the m-th *order moment curve*

$$p_m(\alpha) = \int (\mathcal{R}f^{2D})(\alpha, s) \cdot s^m \, \mathrm{d}s = \iint f^{2D}(u, v) \cdot (u \cdot \sin(\alpha) + v \cdot \cos(\alpha))^m \, \mathrm{d}u\mathrm{d}v. \quad (2.29)$$

It is the m-th moment of the Radon transform for projection with a fixed angle α. We have

$$p_m(\alpha) = \int (\mathcal{R}f^{2D})(\alpha, s) \cdot q_m(s) \, \mathrm{d}s \quad (2.30)$$

$$= \iint f^{2D}(u, v) \cdot (u \cdot \sin(\alpha) + v \cdot \cos(\alpha))^m \, \mathrm{d}u\mathrm{d}v. \quad (2.31)$$

The HLCC now state, slightly more generally that

$$p_m(\alpha) = \int (\mathcal{R}f^{2D})(\alpha, s) \cdot q_m(s) \, \mathrm{d}s, \quad m = 0, 1, 2, \ldots \quad (2.32)$$

is a trigonometric polynomial in θ of degree at most m when $q_m(s)$ is a polynomial of degree m in s [Lewi 83]. The most immediate result of this DCC is that the zero-order moment is constant over all angles

$$p_0(\alpha) = \int (\mathcal{R}f^{2D})(\alpha, s) \, \mathrm{d}s = \text{const.}. \quad (2.33)$$

In essence, this is a conservation of mass statement, as $p_0(\alpha)$ computes the integral over the whole support of f^{2D}, cf. Figure 2.7, left. Another direct consequence for $m = 1$ is Equation 2.29 describing the projection of the center of mass of the object function f^{2D},

$$p_1(\alpha) = u_{com} \cdot \cos(\alpha) + v_{com} \cdot \sin(\alpha), \quad (2.34)$$

with

$$u_{com} = \iint f^{2D}(u, v) \cdot u \, \mathrm{d}u\mathrm{d}v \text{ and } v_{com} = \iint f^{2D}(u, v) \cdot v \, \mathrm{d}u\mathrm{d}v. \quad (2.35)$$

In words, the projection of the center of mass is the center of mass of the projection. Because two and three sources always lie on a circle, these DCCs are not at all limited to circular trajectories. The only necessity is for the projection to the detector to be parallel. However, most HLCC-based artifact reduction methods rely on higher orders, cf. Figure 2.7, bottom, which also require $n + 1$ projections on an arc of a circle to be applicable, while most consider the coefficients of the Fourier series of $p_m(\alpha)$. In fact, $p_m(\alpha)$ is a trigonometric polynomial of degree m and can therefore be represented by a finite number $2 \cdot m + 1$ of Fourier coefficients. It should be noted that even functions for $n = 2, 4, 6...$ can be represented by all cosines, respectively odd functions for $n = 1, 3, 5...$ by all sines. Another popular choice of q_m is some orthogonal polynomial basis, such as Chebyshev polynomials [Lewi 83, Huan 17].

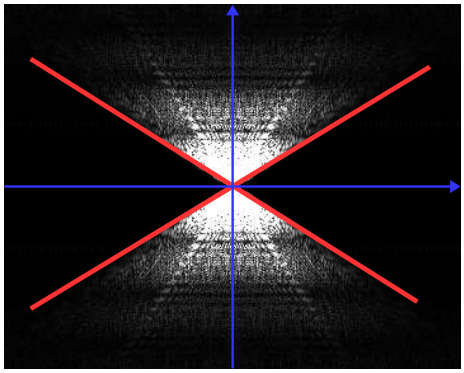

Figure 2.8: Sinogram in Fourier domain of sinogram for object in Figure 2.1, right.

HLCC are a complete set of conditions, meaning that they fully characterize data redundancy for the parallel circular case. HLCC and their extension to fan-beam geometries [Chen 05] have been used in a multitude of applications including data extrapolation [Erla 00, Huan 17, Xu 10], beam-hardening [Tang 11] and overexposure correction [Preu 15], as well as attenuation correction in nuclear imaging [Welc 98]. Note that fan-beam conditions like HLCC in two dimensions are not without problems: while HLCC order n moment curves can be evaluated on $n+1$ projections in the parallel case, a rebinning of fan-beam projections to the parallel case [Sybe 19] allows application of HLCC. However, data is spread over neighboring projections in a range related to the fan width, making a projection-domain evaluation more difficult [Clac 15]. Only in the so-called "projection form" data from one, two, three, etc. projections can be used to test order 0, 1, 2, etc. consistency conditions. This could be achieved, for example by curve fitting and computing a residual as a measure of inconsistency, cf. Figure 2.7. A drawback of HLCC are the strong assumptions made in their derivation: they apply only to 2D parallel an fan-beam projections with a circular trajectory. For the practically more relevant 3D case of the divergent X-ray transform, to our knowledge, no equivalent to HLCC has been found for general trajectories, although a set of necessary conditions was presented [Clac 16]. Complete conditions do exist for special trajectories like sources on a plane [Clac 13b]. In addition, HLCC are not the only way to characterize the range of the Radon transform. In the next section, a different characterization in Fourier domain will be mentioned.

2.3.2 Fourier Properties of Sinogram

The 2D Radon transform can be understood as a superposition of sine-waves. When the object is known to have a finite support $|x| < r$ with some radius r, then these sine-waves are known to have a maximum amplitude, and hence, a maximum slope. Intuitively, the sinogram cannot contain strong edges steeper than said slope, which puts constraints on the spatial frequencies of a sinogram. This intuition is expressed by the Fourier consistency conditions (FCC) which state that certain wedge-shaped regions in the Fourier domain of the projection images have negligible absolute value. The Fourier transform produces the typical wedge-shape in the frequency domain shown in Figure 2.8. Edholm et al. [Edho 86] have presented a description of the

wedge shape by considering the projection of a single point-shaped object. Let (r, ϕ) denote the polar coordinates of a point-shaped object in the u-v-plane

$$f^{\bullet}(u, v) = \delta\left(u - r{\cdot}\cos(\phi),\, v - r \cdot \sin(\phi)\right), \tag{2.36}$$

whose projection $p^{\bullet} = (\mathcal{R}f^{\bullet})$ is the sinusoid curve

$$p^{\bullet}(\alpha,\, s) = \delta\left(s - r \cdot \cos(\phi - \alpha)\right). \tag{2.37}$$

Taking the Fourier transform for the spectral variable $\sigma \leftrightarrow s$ we have

$$(\mathcal{F}_s p^{\bullet})(\alpha, \sigma) = \int \delta\left(s - r \cdot \cos(\phi - \alpha)\right) e^{-2\pi i \sigma s} \mathrm{d}s \tag{2.38}$$

$$= e^{-2\pi i \sigma r \cdot \cos(\phi - \alpha)} \tag{2.39}$$

and finally, the Fourier transform for $n \leftrightarrow \alpha$ yields

$$(\mathcal{F}p^{\bullet})(n, \sigma) = \int e^{-2\pi i(\sigma r \cdot \cos(\phi - \alpha) + n\alpha)} \mathrm{d}\alpha. \tag{2.40}$$

The wedge-shaped region becomes clear only when expressing Equation 2.40 in terms of a Bessel function of order n [Edho 86, Eq. 11]

$$(\mathcal{F}p^{\bullet})(n, \sigma) = J_n(\sigma r) e^{-in(\phi + \pi/2)}, \tag{2.41}$$

because it is a property of such Bessel functions $J_n(\sigma r)$ to decrease rapidly in magnitude, as $|\sigma r|$ decreases below $|n| - 1$ for large $|n|$. This leads to a wedge-shaped region of low absolute energy in the (σ, n) spectrum, with a demarcation defined by the two lines $n = \pm r\sigma$ shown in red in Figure 2.8.

Similar constraints apply for the Fourier transform of so-called *fanograms* [Mazi 10], i.e. the projections for a point-shaped X-ray source rotating about an object in the plane and approximately extended to 3D cone-beam data [Berg 17]. Comparison to other consistency-based cost-functions it has been found that a simple energy-minimization in the wedge-shaped region has problems, especially a bias towards moving the center of mass to the iso-center [Unbe 17b]. It should be noted that the consistency condition does not require the whole wedge to have exactly zero energy, especially for low frequencies (i.e. small n). The conditions have the disadvantage that there is no projection-domain form. Several methods address this problem in particular [Huan 17, Huan 18]

2.4 Consistency Conditions and the X-ray Transform

2.4.1 John's Equation

All consistency conditions are specific to the trajectory of detector and source during the acquisition. Typically, the linear and circular case are widely investigated, but even for these two cases, one may differentiate between parallel 2D, fan-beam and cone-beam geometries. For each of these cases, more than one fundamentally different

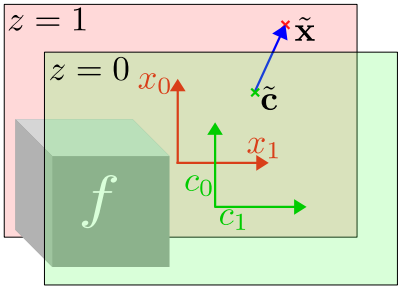

Figure 2.9: X-ray sources on a plane parallel to the detector.

formulation of the data redundancy exists. In the following, we present an introduction to DCCs, with practical applicability to cone-beam geometries in mind. We will rely on a basic redundancy which exists in all X-ray images, so as to be applicable in as many practical situations as possible. As early as 1938, John [John 38, John 04] presented a second-order elliptic partial differential equation (which expresses an inherent dependency in the arguments of the X-ray transform. Suppose all X-ray sources lie on a plane parallel to the detector. Think of $\boldsymbol{c} = (c_0, c_1)^\top$ as an X-ray source position on the $z = 0$ plane and of $\boldsymbol{x} = (x_0, x_1)^\top$ as a pixel on the detector plane with a distance of one, cf. Figure 2.9. The X-ray transform $(\mathcal{X}f)(\boldsymbol{c}, \boldsymbol{x})$ then takes four arguments c_0, c_1, x_0 and x_1 defining any ray that intersects the two planes. Except for rays parallel to the $z = 0$ plane, this is a full parametrization of lines in space which also have four degrees of freedom. This parametrization of lines in space is unusual for X-ray imaging, however, it is common to describe the plenoptic function in the theory of light fields, for instance [Levo 06]. We denote it

$$(\mathcal{X}f)(\boldsymbol{c}, \boldsymbol{x}) \overset{\text{def}}{=} (\mathcal{X}f)\left((c_0, c_1, 0)^\top, (x_0, x_1, 1)^\top\right) \tag{2.42}$$

$$= \int f\left((1-t)\cdot c_0 + t\cdot x_0,\ (1-t)\cdot c_1 + t\cdot x_1,\ t\right) \mathrm{d}t. \tag{2.43}$$

The object f is defined over only three spatial dimensions x, y and z. Since f fully defines the four-argument function $\tilde{g}$, there must be an inherent dependency of these arguments. In fact, it has been shown that the projection data $\tilde{g}\,(\boldsymbol{c}, \boldsymbol{x})$ fulfills the following PDE called John's equation, which we will now derive.

We denote the derivative of f after the first, second and both arguments respectively as f_x, f_y and f_{xy}. For $\frac{\partial}{\partial c_0}$ and $\frac{\partial}{\partial c_1}$ we have

$$\frac{\partial}{\partial c_0}(\mathcal{X}f)(\boldsymbol{c}, \boldsymbol{x}) = \int \frac{\partial}{\partial c_0} f((1-t)\cdot c_0 + t\cdot x_0,\ (1-t)\cdot c_1 + t\cdot x_1,\ t)\mathrm{d}t \tag{2.44}$$

$$= \int (1-t)\cdot f_x((1-t)\cdot c_0 + t\cdot x_0,\ (1-t)\cdot c_1 + t\cdot x_1,\ t)\mathrm{d}t, \tag{2.45}$$

and

$$\frac{\partial}{\partial c_1}(\mathcal{X}f)(\boldsymbol{c}, \boldsymbol{x}) = \int t\cdot f_y((1-t)\cdot c_0 + t\cdot x_0,\ (1-t)\cdot c_1 + t\cdot x_1,\ t)\mathrm{d}t. \tag{2.46}$$

Analogously for $\frac{\partial}{\partial x_0}$ and $\frac{\partial}{\partial x_1}$ we have

$$\frac{\partial}{\partial x_0}(\mathcal{X}f)(\boldsymbol{c},\boldsymbol{x}) = \int t \cdot f_x((1-t)\cdot c_0 + t\cdot x_0,\ (1-t)\cdot c_1 + t\cdot x_1,\ t)\mathrm{d}t, \tag{2.47}$$

$$\text{and} \quad \frac{\partial}{\partial x_1}(\mathcal{X}f)(\boldsymbol{c},\boldsymbol{x}) = \int (1-t)\cdot f_y((1-t)\cdot c_0 + t\cdot x_0,\ (1-t)\cdot c_1 + t\cdot x_1,\ t)\mathrm{d}t. \tag{2.48}$$

We can easily see that for mixed derivatives $\frac{\partial^2}{\partial c_0 \partial x_1}$ and $\frac{\partial^2}{\partial c_1 \partial x_0}$ we get identically

$$\frac{\partial^2}{\partial c_0 \partial x_1}(\mathcal{X}f)\boldsymbol{c},\boldsymbol{x}) = \frac{\partial^2}{\partial c_1 \partial x_0}(\mathcal{X}f)(\boldsymbol{c},\boldsymbol{x}) \tag{2.49}$$

$$= \int (1-t)t\cdot f_{x,y}((1-t)\cdot c_0 + t\cdot x_0,\ (1-t)\cdot c_1 + t\cdot x_1,\ t)\mathrm{d}t, \tag{2.50}$$

or

$$\frac{\partial^2}{\partial c_0 \partial x_1}(\mathcal{X}f)(\boldsymbol{c},\boldsymbol{x}) - \frac{\partial^2}{\partial c_1 \partial x_0}(\mathcal{X}f)(\boldsymbol{c},\boldsymbol{x}) = 0 \tag{2.51}$$

$$\left(\frac{\partial^2}{\partial c_0 \partial x_1} - \frac{\partial^2}{\partial c_1 \partial x_0}\right)(\mathcal{X}f)(\boldsymbol{c},\boldsymbol{x}) = 0. \tag{2.52}$$

This applies to the normalized X-ray transform, as measured in the form of cone-beam projection data

$$\tilde{g}(\boldsymbol{c},\boldsymbol{x}) = \sqrt{(x_0-c_0)^2 + (x_1-c_1)^2 + 1}\cdot(\mathcal{X}f)(\boldsymbol{c},\boldsymbol{x}) \tag{2.53}$$

in exactly the same manner

$$\left(\frac{\partial^2}{\partial c_0 \partial x_1} - \frac{\partial^2}{\partial c_1 \partial x_0}\right)\tilde{g}(\boldsymbol{c},\boldsymbol{x}) = 0. \tag{2.54}$$

This is a complete and quite general characterization of consistency and Patch et al. [Patc 02] used this formulation to synthesize projections by directly solving the PDE numerically. To our knowledge, however, the partial differential equation is not practical for use in motion correction applications in this form.

2.4.2 A Necessary Condition for Motion Parallel to the Detector

In this section we summarize the work by Patch et al. [Patc 02] and by Levine [Levi 10] to express a basic DCC, variations of which are used in this work. We start by establishing a relationship between John's equation to the wave equation. The 2D Fourier transform of the projection data $\hat{g} = (\mathcal{F}_X\tilde{g})$ of for spectral variable $\boldsymbol{\xi} \leftrightarrow \boldsymbol{x}$ is

$$\hat{g}(\boldsymbol{c},\boldsymbol{\xi}) \overset{\text{def}}{=} \mathcal{F}_{\boldsymbol{x}}\tilde{g}(\boldsymbol{c},\boldsymbol{\xi}) \tag{2.55}$$

$$= \int \tilde{g}(\boldsymbol{c},\boldsymbol{x})e^{-2\pi i\boldsymbol{\xi}\boldsymbol{x}}\mathrm{d}\boldsymbol{x} = 0. \tag{2.56}$$

For a fixed source positions $\boldsymbol{c}$, this can be interpreted as the Fourier transform of an X-ray projection image. A derivative of a function $h(x)$ can be written as a multiplication in Fourier space by the spectral variable $\xi \leftrightarrow x$ and a factor of $2\pi i$

$$\mathcal{F}_x\left(\frac{\partial h}{\partial x}\right)(\xi) = 2\pi i\xi \cdot \mathcal{F}h(\xi). \tag{2.57}$$

In Eq. 2.55 we have two partial derivatives, which can be expressed accordingly

$$\mathcal{F}_{\boldsymbol{x}}\left(\frac{\partial^2 \tilde{g}}{\partial c_0 \partial x_1} - \frac{\partial^2 \tilde{g}}{\partial c_1 \partial x_0}\right)(\boldsymbol{c}, \boldsymbol{\xi}) = 0, \tag{2.58}$$

$$2\pi i\xi_0 \frac{\partial}{\partial c_0}\hat{g}(\boldsymbol{c}, \boldsymbol{\xi}) - 2\pi i\xi_1 \frac{\partial}{\partial c_1}\hat{g}(\boldsymbol{c}, \boldsymbol{\xi}) = 0. \tag{2.59}$$

Note that the factor $2\pi i$ can be divided out. Let $\boldsymbol{\xi}^\perp = (\xi_1, -\xi_0)^\top$ denote the orthogonal to the vector of partial derivatives of $\mathcal{F}\tilde{g}$ for the first two arguments

$$\begin{pmatrix} \frac{\partial}{\partial c_0}\hat{g}(\boldsymbol{c}, \boldsymbol{\xi}) \\ \frac{\partial}{\partial c_1}\hat{g}(\boldsymbol{c}, \boldsymbol{\xi}) \end{pmatrix}^\top \boldsymbol{\xi}^\perp = 0, \tag{2.60}$$

or

$$\nabla_{\boldsymbol{c}}\hat{g}(\boldsymbol{c}, \boldsymbol{\xi})^\top \boldsymbol{\xi}^\perp = 0. \tag{2.61}$$

This can be read as a sum of two one-dimensional waves in the plane with the general solution

$$\forall\tau: \quad \hat{g}(\boldsymbol{c}, \boldsymbol{\xi}) = \hat{g}(\boldsymbol{c} + \tau\boldsymbol{\xi}^\perp, \boldsymbol{\xi}), \tag{2.62}$$

or identically

$$\forall\tau: \quad \hat{g}(\boldsymbol{c}, \tau\boldsymbol{t}^\perp) = \hat{g}(\boldsymbol{c} + \boldsymbol{t}, \tau\boldsymbol{t}^\perp). \tag{2.63}$$

This equation states that the Fourier transform of the normalized X-ray transform fulfills an intrinsic consistency property for shifts $\boldsymbol{t}$ of the X-ray source, which is, however, difficult to interpret in Fourier space. Levine et al. [Levi 10] later pointed out a direct consequence of Equation 2.62:

Let us assume we have acquired two cone-beam projections $\tilde{g}(\boldsymbol{c}, \cdot)$ and $\tilde{g}(\boldsymbol{c}+\boldsymbol{t}, \cdot)$ by moving an X-ray source $\boldsymbol{c}$ parallel to the detector plane. Without loss of generality, we can choose any particular coordinate system. Let the vector of motion $\boldsymbol{t} = (t, 0)^\top$ be aligned with the c_0 axis. Since the spectrum is identical in the $\boldsymbol{t}^\perp = (0, t)^\top$ direction, we have

$$\forall\xi_1: \quad \hat{g}\left(c_0 + t,\, c_1;\, 0,\, \xi_1\right) = \hat{g}\left(c_0,\, c_1;\, 0,\, \xi_1\right). \tag{2.64}$$

We can now invert the partial Fourier transform $\xi_1 \leftrightarrow x_1$ and consider only the zero-frequency $\xi_0 = 0$ in the other direction

$$\text{for } \xi_0{=}0: \quad \int \tilde{g}\left(c_0 + t,\, c_1;\, x_0,\, x_1\right) e^{-2\pi i\xi_0 x_0} \mathrm{d}x_0 = \int \tilde{g}\left(c_0,\, c_1;\, x_0,\, x_1\right) e^{-2\pi i\xi_0 x_0} \mathrm{d}x_0 \tag{2.65}$$

$$\iff \qquad \int \tilde{g}\left(c_0 + t,\, c_1;\, x_0,\, x_1\right) \mathrm{d}x_0 = \int \tilde{g}\left(c_0,\, c_1;\, x_0,\, x_1\right) \mathrm{d}x_0. \tag{2.66}$$

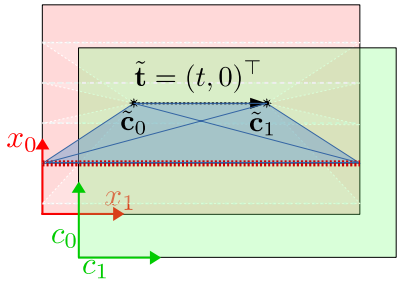

Figure 2.10: Several lines on the detector (white, dotted) parallel to the motion $\boldsymbol{t}$ (black, dotted).

Since these considerations are independent of an actual coordinate system, they apply to a general motion $\boldsymbol{t}$ and integration variable s along the detector line and its orthogonal $\boldsymbol{t}^\perp$

$$\forall u \in \mathbb{R}: \quad \int \tilde{g}\left(\boldsymbol{c}, s\boldsymbol{t} + u\boldsymbol{t}^\perp\right) \mathrm{d}s = \int \tilde{g}\left(\boldsymbol{c} + \boldsymbol{t},\ s\boldsymbol{t} + u\boldsymbol{t}^\perp\right) \mathrm{d}s. \tag{2.67}$$

Since a line-trajectory parallel to the detector might be found in a linear tomosynthesis application, we will refer to Equation 2.67 as *linear tomosynthesis condition* (LTC). We point out that Equation 2.67 implies an equality also of the partial derivatives in u-direction (respectively x_1-direction in Equation 2.66)

$$\forall u \in \mathbb{R}: \quad \frac{\partial}{\partial u} \int \tilde{g}\left(\boldsymbol{c}, s\boldsymbol{t} + u\boldsymbol{t}^\perp\right) \mathrm{d}s = \frac{\partial}{\partial u} \int \tilde{g}\left(\boldsymbol{c} + \boldsymbol{t},\ s\boldsymbol{t} + u\boldsymbol{t}^\perp\right) \mathrm{d}s. \tag{2.68}$$

The LTC in Equation 2.67 applies for arbitrary offsets on the detector u orthogonal to the direction of motion $\boldsymbol{t}$. There exists a one-parameter function of redundant information in two projections, cf. Figure 2.10. For each choice of u, the LTC uses information from a plane through the object f defined by the two source positions and any detector point $s\boldsymbol{t} + u\boldsymbol{t}^\perp$. In Figure 2.10, one such plane is highlighted in transparent blue and it belongs to the detector line highlighted in dotted red. These planes, called epipolar planes, will play an important role from Section 4.1.1 onward.

It is worth mentioning that Equation 2.65 and 2.66 are not equivalent to Equation 2.54, since only the $\xi_0 = 0$ frequency is taken into consideration. This ignores much of the redundant information and LTC are arguably weaker than Equation 2.54. We investigate this particular condition, because it avoids additional assumptions on the data that may impede practical application. However, Equation 2.66 does not express higher order dependencies due to a specific trajectory under consideration. If more prior information is available, e.g. more than one projection image along each line is given, one may obtain more complex conditions [Clac 13a, Clac 13b]

The power of the simple integral condition of LTC lies in the fact that it is a pairwise condition, meaning that *any two projections* necessarily fulfill it. Even if the sources move on a circle (or in fact any other trajectory) in the source plane, a line always passes through two sources. The condition does, however, require that the detectors are in the same plane, which is not the case for rotations CT. We will get back to this restriction in Section 4.1, where we will find that the LTC can be extended to such cases by virtually rotating and moving the detector.

CHAPTER 3

The Projective Geometry of Flat-Panel X-Ray Imaging

BEFORE WE BEGIN the analysis of images, it is mandatory to understand the geometric process underlying image generation. At this point, we choose to ignore all aspects of geometric interaction of electromagnetic rays with matter i.e., scattering and reflections to obtain an *ideal* model for X-ray imaging, identical to that of most visible light and infrared imaging applications – the central projection onto a planar detector. The latter is well understood and described in standard works of computer vision [Hart 00, Truc 98]. The object is placed between the detector and X-ray source position, but this is algebraically identical to a detector between the object and the camera center. In the context of this thesis, the "camera" is an X-ray imaging system, and the camera center is analog to the point-shaped X-ray source with the image being the flat-panel detector.

The common framework is real projective geometry for a good reason: Determinants of homogeneous coordinates of points, lines and planes of two and three dimensions compactly and elegantly describe all linear operations. The algorithms discussed in this thesis are based on (a) integrals over lines in a plane and (b) integrals over planes in space. All geometric relationships we require are union (join), intersection (meet) or linear transformation including central projection. Depending on the objects involved, the suitable geometric language may be complex, yet it is always linear. In this chapter, we will introduce the reader to operations on linear geometric objects in homogeneous coordinates of real projective two- and three-space. The way we describe geometry largely goes back to mathematicians of the late 19^{th} century, namely, Hermann G. Grassmann [Gras 62], Julius Plücker [Pluc 68] and Felix Klein [Klei 72]. The goal of this chapter is to introduce geometric concepts on such a level that the thesis is self-contained, assuming only basic linear algebra. A standard work on projective geometry is, for example Coxeter et al. [Coxe 87]. A concise introduction can be found in Hartley et al. [Hart 00].

3.1 Projective Geometry of Two- and Three-Space

3.1.1 Notation

At first sight, it is easy to introduce an algebraic framework for geometry. We refer to the classical approach simply as "Euclidean geometry" in this thesis. For instance, one may represent points in the plane by two real-valued coordinates, or lines by one such point and a direction, given, for example, by a unit two-vector. The same notation applies as in the previous chapters. This section introduces and motivates a projective representation based on homogeneous coordinates, which ultimately proves more concise [Rich 11].

In Table 3.1 and 3.2, a list of important notational conventions is introduced for this chapter. Homogeneous points in two-space (i.e. with three coordinates) are denoted in bold lowercase $\mathbf{a}, \mathbf{b}, \mathbf{c}$ not set in italic. Since homogeneous lines in two-space have the same representation as homogeneous three-vectors, we also use bold lowercase $\mathbf{l}, \mathbf{m}$ to denote lines. It should be straight forward to differentiate between the two meanings based on the context, but also on the characters used. Sometimes we also have to consider points and planes in the 3D world, which we represent with vectors in homogeneous three-space (i.e. with four components) denoted by bold lowercase decorated with a bar above the symbol $\bar{\mathbf{a}}, \bar{\mathbf{b}}, \bar{\mathbf{c}}$ ("one dimension up"). We use the letter $\bar{\mathbf{c}}$ exclusively for "center of projection" which in the context of this thesis is the point-shaped X-ray source. We use the letters $\bar{\mathbf{e}}$ and $\bar{\mathbf{f}}$ for planes exclusively. The only exception is the plane at infinity denoted as $\bar{\pi}^\infty$. Lines in three-space can be represented as Plücker coordinates. These will be denoted with calligraphic $\mathcal{L}$ for "line" and later frequently $\mathcal{R}$ for "ray" and $\mathcal{B}$ for "baseline". Note that these homogeneous vectors (i.e. defined up to scale) with six coordinates have must abide to an additional constraint, called the Grassmann-Plücker relation. The space of Plücker lines is therefore merely four-dimensional (six minus one for scale and another one for this ralation). The symbol $\cong$ will be used to denote equality up to positive scalar multiplication. For the geometric operation of intersection, we will use the function meet(...) which maps, for example, two lines in two-space to the common point or two planes in three-space to their common line. The dual operation is called join(...) and connects, for example, two points to the joining line or a line and a point in three-space to the common plane. We use the symbol $\in$ and $\notin$ on points, lines and planes to signify "(not) contains" or "(not) lies on" in the geometric sense.

Transformation of homogeneous quantities can be performed with general matrices called homographies, as well as projection matrices that map from three- to two-space. We use special characters to differentiate between these: $\mathbf{H} \in \mathbb{R}^{3\times3}$ for transformations of two-space, $\mathbf{T} \in \mathbb{R}^{4\times4}$ for transformations of three-space and $\mathbf{P} \in \mathbb{R}^{3\times4}$ for projection from three- to two-space. The character $\mathbf{R}$ is used in different spaces to denote rotation. Usually, this is an orthogonal matrix with determinant 1.

Table 3.1: Summary of notation used in this chapter.

Two-space	
$\mathbf{a}, \mathbf{b}, \mathbf{o}, \mathbf{x} \dots$	Homogeneous points in the plane $\mathbb{P}^2$ (typical names).
$\mathbf{l}, \mathbf{m}, \dots \in \mathbb{P}^2$	Homogeneous lines in the plane.
$\mathbf{l}^\infty \in \mathbb{P}^2$	Line at infinity.
Three-space	
$\bar{\mathbf{a}}, \bar{\mathbf{b}}, \bar{\mathbf{o}}, \bar{\mathbf{x}} \dots$	Homogeneous points in three-space $\mathbb{P}^3$ (typical names).
$\bar{\mathbf{e}}, \bar{\mathbf{f}} \dots \in \mathbb{P}^3$	Planes in three-space.
$\bar{\pi}^\infty \in \mathbb{P}^3$	Plane at infinity.
$\mathcal{L} \in \mathbb{P}^5$,$\tilde{\mathcal{L}} \in \mathbb{P}^5$	A line in space in Plücker coordinates and its dual.
$[\mathcal{L}]_\times$	4×4 Plücker matrix, composed from the six coordinates of $\mathcal{L}$.
Operators	
join(...)	Line connecting two points or plane through a line and a point.
meet(...)	Intersection of two lines in the plane or intersection of two planes.
$\cong$	Equality of homogeneous quantities. On the level of homogeneous coordinates this translated to equality up to (positive) scalar multiplication.
$\in$,$\notin$	Also used for "contains" resp. "does not contain"; e.g $\mathbf{x} \in \mathbf{l}$ reads "point $\mathbf{x}$ lies on line $\mathbf{l}$".

3.1.2 Homogeneous Coordinates and Infinite Points

3.1.2.1 Points and Lines in Two-Space

We define a 2D line $\mathbf{l} \subset \mathbb{R}^2$ as the set of solutions to a homogeneous equation (i.e. one which equates to zero) with three scalar parameters l_0, l_1, l_2

$$\mathbf{l} = \left\{ \begin{pmatrix} u \\ v \end{pmatrix} \in \mathbb{R}^2 \,:\, l_0 u + l_1 v + l_2 = 0 \right\}. \tag{3.1}$$

Just like any equality, we can multiply both sides of the linear equation with a non-zero scalar $\lambda \neq 0$ without changing its solution

$$\begin{pmatrix} u \\ v \end{pmatrix} \in \mathbf{l} \iff \lambda l_0 u + \lambda l_1 v + \lambda l_2 = 0. \tag{3.2}$$

The vector $\begin{pmatrix} l_1 \\ -l_0 \end{pmatrix}$ points in the direction of the line and $\begin{pmatrix} l_0 \\ l_1 \end{pmatrix}$ is normal to the line. The angle between the line and the u-axis is thus

$$\alpha = \operatorname{atan2}(-l_0, l_1). \tag{3.3}$$

Table 3.2: Naming conventions used throughout this thesis.

Naming conventions	(often used with additional indices and decorators)
$\mathbf{H} \in \mathbb{R}^{3\times3}$	Homography of the plane i.e. general 3×3 matrix defined up to positive scale.
$\mathbf{T} \in \mathbb{R}^{4\times4}$	Homography of three-space i.e. general 4×4 matrix defined up to positive scale.
$\mathbf{R}$	Rotation matrix (sometimes represented as homography).
$\mathbf{P} \in \mathbb{R}^{3\times4}$	Projection matrix.
$\mathbf{F} \in \mathbb{R}^{3\times3}$	Fundamental matrix.
$\bar{\mathbf{c}} \in \mathbb{P}^3$	"center of projection", e.g. camera center.
$\mathcal{R} \in \mathbb{P}^5$	Plücker coordinates of a projection ray.
$\mathcal{B} \in \mathbb{P}^5$	Plücker coordinates of the epipolar baseline.

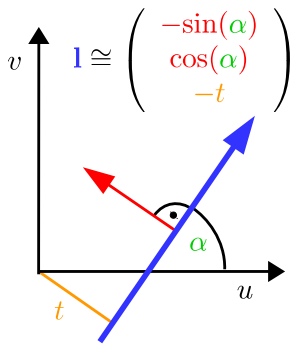

Figure 3.1: 2D line represented by angle to the u-axis α and distance to the origin t.

The signed distance of $\mathbf{l}$ to the origin is

$$t = \frac{-l_2}{\sqrt{l_0^2 + l_1^2}}. \tag{3.4}$$

This can be verified by checking the line equation for zero in the point $(t \cdot l_0, t \cdot l_1)^\top$.

Note that multiplications by scalars $\lambda < 0$ flip the sign of t and change the angle by π, see Equation 3.9. We therefore introduce the equality relation of positive scalar multiples of the vectors $\mathbf{a}, \mathbf{b} \in \mathbb{R}^n$

$$\mathbf{a} \cong \mathbf{b} \iff \exists\lambda > 0 \in \mathbb{R} \,:\, \lambda\mathbf{a} - \mathbf{b} = 0, \tag{3.5}$$

and, in the following, represent the line by the vector of its parameters

$$\mathbf{l} \cong \begin{pmatrix} l_0 \\ l_1 \\ l_2 \end{pmatrix} \in \mathbb{P}^2, \tag{3.6}$$

in a topological space

$$\mathbb{P}^n = \frac{\mathbb{R}^{n+1}\backslash\{\mathbf{0}\}}{\mathbb{R}^{+}\backslash\{0\}}. \tag{3.7}$$

This is the $\mathbb{R}^{n+1}$-space without the zero-vector, up to positive scalar multiples. The space $\mathbb{P}^2$ contains exactly one set of equivalent vectors for every directed line in $\mathbb{R}^2$ and additionally equivalents of the vector (and its negative)

$$\mathbf{l}^{\infty} = \begin{pmatrix} 0 \\ 0 \\ 1 \end{pmatrix}. \tag{3.8}$$

We call $\mathbf{l}^{\infty}$ the line at infinity, for reasons discussed later in Section 3.1.2.3. The line with angle α to the u-axis and signed distance to the origin t, as shown in Figure 3.1 is

$$\mathbf{l} \cong \begin{pmatrix} l_0 \\ l_1 \\ l_2 \end{pmatrix} \cong \text{line}(\alpha, t) = \begin{pmatrix} -\sin(\alpha) \\ \cos(\alpha) \\ -t \end{pmatrix} = \frac{1}{\sqrt{l_0^2 + l_1^2}} \begin{pmatrix} l_0 \\ l_1 \\ l_2 \end{pmatrix} \in \mathbb{P}^2, \tag{3.9}$$

compare Equations 3.3 and 3.4.

For a euclidian point $(u, v)^{\top}$, we have

$$\mathbf{x} \cong \begin{pmatrix} u \\ v \\ 1 \end{pmatrix} \in \mathbf{l} \iff \mathbf{x}^{\top}\mathbf{l} = 0. \tag{3.10}$$

Observe that we used the same space $\mathbb{P}^2$ and equivalence relation $\cong$ for the representation of both points and lines. We say that a line is in Hessian normal form, when its coordinates are scaled such that its normal is of unit length $\|(l_0, l_1)\| = 1$. For points not on the line (or generally $(n-1)$-dimensional subspace, e.g. plane in space) the dot-product in Hessian normal form yields the signed distance d

$$\mathbf{x} \cong \begin{pmatrix} u \\ v \\ 1 \end{pmatrix} \notin \mathbf{l} \iff \mathbf{x}^{\top}\mathbf{l} = d \neq 0. \tag{3.11}$$

In Figure 3.2 we present two common methods of representing homogeneous vectors. Since arbitrary scalar factors λ can be divided out, one may choose to normalize the last coordinate to one (Euclidean geometry). However, in this representation infinite points do not exist due to a division by zero. If on the other hand one chooses to normalize the homogeneous vector, one obtains the geometry on the unit sphere (see also Riemann geometry).

3.1.2.2 Join and Meet Operations

We would like to find the point of intersection $\mathbf{x} \in \mathbb{P}^2$ of the two lines $\mathbf{l}, \mathbf{m} \in \mathbb{P}^2$. We know that both lines contain the point $\mathbf{x}$

$$\mathbf{x} \cong \begin{pmatrix} u \\ v \\ 1 \end{pmatrix} \in \mathbb{P}^2 = \frac{\mathbb{R}^3 \backslash \{0\}}{\mathbb{R} \backslash \{0\}} \sim S^{2+}$$

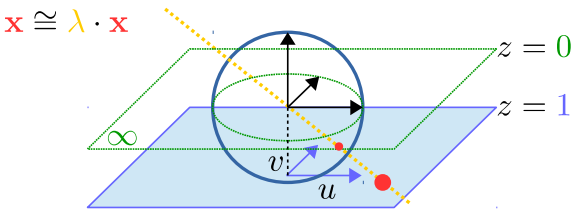

Figure 3.2: Relationship of the projective plane to the Riemann sphere. While only finite points can be represented in the $z = 1$ plane (ie. Euclidian geometry by division by homogeneous coordinate) all points including infinite points can be represented on the sphere (Riemann geometry by division by vector norm).

$$\mathbf{l}^\top \mathbf{x} = 0 \text{ and } \mathbf{m}^\top \mathbf{x} = 0. \tag{3.12}$$

In words, the vector representation of $\mathbf{x}$ is orthogonal to those of $\mathbf{l}$ and $\mathbf{m}$. An orthogonal vector in $\mathbb{R}^3$ is readily computed as the cross product. We have

$$\mathbf{x} \cong \mathbf{l} \times \mathbf{m} \overset{\text{(def)}}{=} \text{meet}(\mathbf{l}, \mathbf{m}). \tag{3.13}$$

Next, we would like to find the line $\mathbf{l} \in \mathbb{P}^2$ through two points $\mathbf{a}, \mathbf{b} \in \mathbb{P}^2$. We know that both points are on the line

$$\mathbf{a}^\top \mathbf{l} = 0 \text{ and } \mathbf{b}^\top \mathbf{l} = 0. \tag{3.14}$$

In words, the vector representation of $\mathbf{l}$ is orthogonal to those of $\mathbf{a}$ and $\mathbf{b}$. An orthogonal vector in $\mathbb{R}^3$ is readily computed as the cross product. We have

$$\mathbf{l} \cong \mathbf{a} \times \mathbf{b} \overset{\text{(def)}}{=} \text{join}(\mathbf{a}, \mathbf{b}). \tag{3.15}$$

Note that Equations 3.13 and 3.15 are equivalent with the roles of points and lines, as well as join and meet, exchanged. This principle is called *duality* and applies generally to d- and $(n-d-1)$-dimensional objects of n-dimensional projective space. In case of three-space, for instance, points ($d = 0$) and planes ($3 - 0 - 1 = 2$) will be dual to one another, compare Section 3.1.3.1. Interestingly, Lines ($d = 2$) are dual to themselves and we will find a primal-dual pair of coordinates of lines in space, compare Section 3.1.3.2 and Section 3.1.3.3.

3.1.2.3 Infinity, Orientation and Closest Point to Origin

Point at Infinity and Line Direction In the following, we will refer to points with homogeneous coordinate zero as ideal or infinite points. One way to think of

infinite points is as directions. A line contains the infinite point in the direction of the line (and its negative)

$$\begin{pmatrix} l_0 \\ l_1 \\ l_2 \end{pmatrix} \begin{pmatrix} l_1 \\ -l_0 \\ 0 \end{pmatrix}^\top = 0. \tag{3.16}$$

The line with direction $\boldsymbol{d} \in \mathbb{R}^2$ through the point $\boldsymbol{p} \in \mathbb{R}^2$ is thus

$$\text{join}\left(\begin{pmatrix} \boldsymbol{p} \\ 1 \end{pmatrix}, \begin{pmatrix} \boldsymbol{d} \\ 0 \end{pmatrix}\right). \tag{3.17}$$

The point of intersection of two parallel lines

$$\text{meet}(\mathbf{l}, \hat{\mathbf{l}}) = \begin{pmatrix} l_1(l_2 + c) - l_2 l_1 \\ l_0 l_2 - (l_2 + c) l_0 \\ l_0 l_1 - l_1 l_0 \end{pmatrix} = \begin{pmatrix} l_1 c \\ -l_0 c \\ 0 \end{pmatrix} \cong \begin{pmatrix} l_1 \\ -l_0 \\ 0 \end{pmatrix} \tag{3.18}$$

is an infinite point in the direction of the lines. More importantly, the meet with infinity, compare Equation 3.8, gives the direction

$$\mathbf{d} = \text{meet}\left(\mathbf{l}, \mathbf{l}^\infty\right) = \begin{pmatrix} l_1 \\ -l_0 \\ 0 \end{pmatrix}. \tag{3.19}$$

Closest Point to the Origin Recall that lines and points in projective two-space are dual to one another, and especially that they have identical algebraic representations. The three-vector $\mathbf{d} = (l_1, -l_0, 0)^\top$ can be seen not only as a point at infinity, but also as a line. This line is orthogonal to $\mathbf{l}$ (since its normal is the direction vector) and it passes through the origin, as its last element is zero. Geometrically, the path of shortest distance to the origin is also orthogonal to the line. Therefore, the closest point on the line to the origin can be computed via

$$\mathbf{o} = \text{meet}\left(\mathbf{l}, \mathbf{d}\right) \cong \begin{pmatrix} -l_2 l_0 \\ -l_2 l_1 \\ 1 \end{pmatrix}. \tag{3.20}$$

Orientation and Sign of Join and Meet A line and its negative contain the same points, but they point in opposite directions. The order of points in join and meet operations matters for the orientation of lines, for example

$$\text{join}(\mathbf{a}, \mathbf{b}) = -\text{join}(\mathbf{b}, \mathbf{a}). \tag{3.21}$$

Also note, that two lines may intersect in a "negative point" with negative homogeneous coordinate. We think of these points as normal Euclidian points with the additional property, that they invert orientations, for example

$$\text{join}(\mathbf{a}, \mathbf{b}) = \text{join}(-\mathbf{b}, \mathbf{a}) = -\text{join}(\mathbf{a}, -\mathbf{b}), \tag{3.22}$$

and meet accordingly.

3.1.2.4 Plücker Matrix in Two Dimensions

This subsection demonstrates that the cross-product can be re-written as a multiplication with a skew-symmetric matrix. We do this, firstly, because matrix notation allows for the concatenation of several operations into one by mere multiplication. Secondly, the cross-product is defined only for vectors of three components, while the following concepts apply to arbitrary dimension. It will become obvious in Section 3.1.3.2 that this is a general way to represent two-dimensional sub-spaces, using so-callled Plücker matrices. We begin with the join operation of two points

$$\mathbf{l} \cong \text{join}(\mathbf{a}, \mathbf{b}) = \mathbf{a} \times \mathbf{b} = \begin{pmatrix} a_1 b_2 - b_1 a_2 \\ b_0 a_2 - a_0 b_2 \\ a_0 b_1 - a_1 b_0 \end{pmatrix} = \begin{pmatrix} l_0 \\ l_1 \\ l_2 \end{pmatrix}. \tag{3.23}$$

and define an operator $[\cdot]_\times$ which assembles a skew-symmetric matrix according to

$$[\mathbf{l}]_\times = \mathbf{b}\mathbf{a}^\top - \mathbf{a}\mathbf{b}^\top = \begin{pmatrix} a_0 b_0 - b_0 a_0 & a_1 b_0 - b_1 a_0 & a_2 b_0 - b_2 a_0 \\ a_0 b_1 - b_0 a_1 & a_1 b_1 - b_1 a_1 & a_2 b_1 - b_2 a_1 \\ a_0 b_2 - b_0 a_2 & a_1 b_2 - b_1 a_2 & a_2 b_2 - b_2 a_2 \end{pmatrix} = \begin{pmatrix} 0 & -l_2 & l_1 \\ l_2 & 0 & -l_0 \\ -l_1 & l_0 & 0 \end{pmatrix}. \tag{3.24}$$

The meet with another line $\mathbf{m}$ can be written as matrix multiplication

$$\mathbf{x} \cong \text{meet}(\mathbf{l}, \mathbf{m}) = [\mathbf{l}]_\times \mathbf{m}. \tag{3.25}$$

3.1.2.5 Point and Line Homography

A linear (i.e. collinearity-preserving) transformation of $\mathbb{P}^n$ can be expressed by a general $n \times n$ matrix, up to scale. $\mathbf{H} \in \mathbb{R}^{3\times 3}$ is called a (planar) homography. Matrix multiplication $\mathbf{H}\mathbf{x} = \mathbf{x}'$ by points represents the largest set of linear transformations, including projective distortion. For example, a translation by $(t_x, t_y)^\top$ in projective two-space can be written as matrix multiplication

$$\begin{pmatrix} 1 & 0 & t_x \\ 0 & 1 & t_y \\ 0 & 0 & 1 \end{pmatrix} \begin{pmatrix} x \\ y \\ 1 \end{pmatrix} = \begin{pmatrix} x + t_x \\ y + t_y \\ 1 \end{pmatrix}. \tag{3.26}$$

A rigid transformation in $\mathbb{P}^2$ with rotation angle α and translation $\boldsymbol{t} = \begin{pmatrix} t_x \\ t_y \end{pmatrix}$ is

$$\mathbf{H} \cong \begin{pmatrix} \cos(\alpha) & \sin(\alpha) & t_x \\ -\sin(\alpha) & \cos(\alpha) & t_y \\ 0 & 0 & 1 \end{pmatrix} = \begin{pmatrix} \mathbf{R} & \boldsymbol{t} \\ 0\,0 & 1 \end{pmatrix}, \tag{3.27}$$

with a rotation matrix

$$\mathbf{R} = \begin{pmatrix} \cos(\alpha) & \sin(\alpha) \\ -\sin(\alpha) & \cos(\alpha) \end{pmatrix}. \tag{3.28}$$

In this work, we require that $\det(\mathbf{H}) > 0$, as to preserve orientation. A reflection, for instance, reverses orientations and has a negative determinant. Observe, that a line

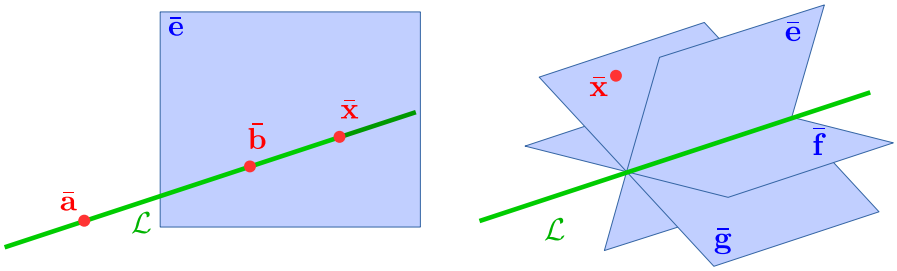

Figure 3.3: Primal and dual lines in three-space. Points shown in red, lines in green. planes in blue. Left: A line $\mathcal{L}$ in three-space defined by two points $\bar{\mathbf{a}}$, $\bar{\mathbf{b}} \in \mathbb{P}^3$ intersecting a plane in the point $\bar{\mathbf{x}} = [\mathcal{L}]_\times \bar{\mathbf{e}}$. Right: A line $\mathcal{L}$ in three-space defined by two planes $\bar{\mathbf{e}}, \bar{\mathbf{f}} \in \mathbb{P}^3$joined with the point $\bar{\mathbf{x}}$ by a common plane $\bar{\mathbf{g}} = [\tilde{\mathcal{L}}]_\times \bar{\mathbf{x}}$.

$\mathbf{l} \cong \mathbf{a} \times \mathbf{b} \in \mathbb{P}^2$ transforms with the inverse transpose of a homography (provided that the determinant is positive!)

$$(\mathbf{Ha}) \times (\mathbf{Hb}) = \det(\mathbf{H})\mathbf{H}^{-\top}(\mathbf{a} \times \mathbf{b}) \cong \mathbf{H}^{-\top}\mathbf{l}. \tag{3.29}$$

In case of the rigid transformation from Equation 3.27, we see that lines transform according to

$$\mathbf{H}^{-\top} \cong \begin{pmatrix} \mathbf{R} & 0 \\ \left(-\mathbf{R}^\top \boldsymbol{t}\right)^\top & 1 \end{pmatrix}. \tag{3.30}$$

A better intuition on transformations in projective spaces is beyond the scope of this thesis and we refer to Hartley and Zisserman [Hart 00] for further reading.

3.1.3 The Geometry of Lines in Three-Space

3.1.3.1 Points and Planes in Three-Space

Analogous to the line equation in Section 3.1.2.1, the equation of a plane in $\mathbb{R}^3$ can be written in Hessian normal form

$$\bar{\mathbf{e}} \cong \begin{pmatrix} E_0 \\ E_1 \\ E_2 \\ E_3 \end{pmatrix} \cong \begin{pmatrix} | \\ \mathring{\boldsymbol{n}} \\ | \\ -t \end{pmatrix} = \frac{1}{\sqrt{E_0^2 + E_1^2 + E_2^2}} \begin{pmatrix} E_0 \\ E_1 \\ E_2 \\ E_3 \end{pmatrix}, \tag{3.31}$$

that is, with a normal of unit length$\|\mathring{\boldsymbol{n}}\| = 1$. We can represent the euclidian point $(X, Y, Z)^\top \in \mathbb{R}^3$ as a vector $(X, Y, Z, 1)^\top \in \mathbb{P}^3$. A point $\bar{\mathbf{x}} \in \mathbb{P}^3$ is contained in a plane iff. $\bar{\mathbf{x}}^\top \bar{\mathbf{e}} = 0$. Observe that in $\mathbb{P}^3$, points are dual to planes.

3.1.3.2 Plücker Matrix

We can describe a line $\mathcal{L}$ in 3-space by two distinct points $\bar{\mathbf{a}}$ and $\bar{\mathbf{b}}$ that lie on it. Using the results of Section 3.1.2.4 we express the line as an anti-symmetric matrix

$$[\mathcal{L}]_\times = \bar{\mathbf{b}}\bar{\mathbf{a}}^\top - \bar{\mathbf{a}}\bar{\mathbf{b}}^\top \in \mathbb{R}^{4\times 4}, \tag{3.32}$$

and show in this section that it represents the line $\mathcal{L} = \text{join}(\bar{\mathbf{a}}, \bar{\mathbf{b}})$:

Meet with a plane. By multiplication with a plane $\bar{\mathbf{e}}$, we get

$$\bar{\mathbf{x}} = [\mathcal{L}]_\times \bar{\mathbf{e}} = \bar{\mathbf{b}} \underbrace{\bar{\mathbf{a}}^\top \bar{\mathbf{e}}}_{\alpha} - \bar{\mathbf{a}} \underbrace{\bar{\mathbf{b}}^\top \bar{\mathbf{e}}}_{\beta} = \bar{\mathbf{b}}\alpha - \bar{\mathbf{a}}\beta. \tag{3.33}$$

The plane $\bar{\mathbf{e}}$ either

- contains the line $\mathcal{L}$, in which case $\alpha = \beta = 0$ and $[\mathcal{L}]_\times \bar{\mathbf{e}} = \mathbf{0} \notin \mathbb{P}^3$.
- or $\bar{\mathbf{x}}$ is the point of intersection of the line $\mathcal{L}$ and the plane $\bar{\mathbf{e}}$ because
  - $\bar{\mathbf{x}}$ is on the line $\mathcal{L}$ as it is linear combination of $\bar{\mathbf{a}}$ and $\bar{\mathbf{b}}$ (see Equation 3.33),
  - and the plane $\bar{\mathbf{e}}$ contains the point $\bar{\mathbf{x}}$, since

$$\bar{\mathbf{e}}^\top \bar{\mathbf{x}} = \bar{\mathbf{e}}^\top [\mathcal{L}]_\times \bar{\mathbf{e}} = \beta\alpha - \alpha\beta = 0. \tag{3.34}$$

We define

$$\text{meet}(\mathcal{L}, \bar{\mathbf{e}}) = \bar{\mathbf{x}} = [\mathcal{L}]_\times \bar{\mathbf{e}}. \tag{3.35}$$

Uniqueness. Two arbitrary distinct points $\bar{\mathbf{a}}'$ and $\bar{\mathbf{b}}'$ on the line can be written as a linear combination of $\bar{\mathbf{a}}$ and $\bar{\mathbf{b}}$. Let

$$\bar{\mathbf{a}}' = \lambda_A \bar{\mathbf{a}} + \lambda_B \bar{\mathbf{b}} \tag{3.36}$$

$$\text{and } \bar{\mathbf{b}}' = \mu_A \bar{\mathbf{a}} + \mu_B \bar{\mathbf{b}}. \tag{3.37}$$

Then, the Plücker matrix of their joining line is identical up to scale with $[\mathcal{L}]_\times$ since[1]

$$[\mathcal{L}']_\times = \bar{\mathbf{b}}'\bar{\mathbf{a}}'^\top - \bar{\mathbf{a}}'\bar{\mathbf{b}}'^\top = \underbrace{(\lambda_A\mu_B - \lambda_B\mu_A)}_{\neq 0 \text{ for } \bar{\mathbf{a}} \not\simeq \bar{\mathbf{b}}} [\mathcal{L}]_\times. \tag{3.38}$$

Plücker Coordinates From Equation 3.32, we see that $[\mathcal{L}]_\times$is a skew-symmetric 4×4 matrix constituted by six distinct values

$$[\mathcal{L}]_\times = \bar{\mathbf{b}}\bar{\mathbf{a}}^\top - \bar{\mathbf{a}}\bar{\mathbf{b}}^\top \cong \begin{pmatrix} 0 & L_{01} & L_{02} & L_{03} \\ -L_{01} & 0 & L_{12} & L_{13} \\ -L_{02} & -L_{12} & 0 & L_{23} \\ -L_{03} & -L_{13} & -L_{23} & 0 \end{pmatrix} \tag{3.39}$$

with

$$\mathcal{L} \cong \begin{pmatrix} L_{01} \\ L_{02} \\ L_{03} \\ L_{12} \\ L_{13} \\ L_{23} \end{pmatrix} = \begin{pmatrix} a_0b_1 - a_1b_0 \\ a_0b_2 - a_2b_0 \\ a_0b_3 - a_3b_0 \\ a_1b_2 - a_2b_1 \\ a_1b_3 - a_3b_1 \\ a_2b_3 - a_3b_2 \end{pmatrix}, \tag{3.40}$$

[1] We ignore here, that the order of points $\bar{\mathbf{a}}'$ and $\bar{\mathbf{b}}'$ on the line affects orientation, when the scalar is negative.

where

$$L_{01}L_{23} - L_{02}L_{13} + L_{03}L_{12} = 0. \tag{3.41}$$

Since $\mathcal{L}$ is defined up to scale and abides by Equation 3.41, also called the Grassmann-Plücker relation, it has only four degrees of freedom, just like lines in three-space should have. This duality is visualized in Figure 3.3.

3.1.3.3 Dual Plücker Matrix

This subsection defines a dual line via the intersection of two planes $\bar{\mathbf{e}}$ and $\bar{\mathbf{f}}$. We then show that the representation comprises the same set of coordinates in a different arrangement, as if it were represented by two points on the line. We express the dual line $\tilde{\mathcal{L}} = \text{meet}(\bar{\mathbf{e}}, \bar{\mathbf{f}})$ as an anti-symmetric matrix

$$[\tilde{\mathcal{L}}]_\times = \bar{\mathbf{f}}\bar{\mathbf{e}}^\top - \bar{\mathbf{e}}\bar{\mathbf{f}}^\top \in \mathbb{R}^{4\times 4}, \tag{3.42}$$

and obtain a plane $\bar{\mathbf{g}}$, which contains both the line $\tilde{\mathcal{L}}$ and a point $\bar{\mathbf{x}}$ via

$$\bar{\mathbf{g}} = [\tilde{\mathcal{L}}]_\times \bar{\mathbf{x}} = \text{join}(\mathcal{L}, \bar{\mathbf{x}}). \tag{3.43}$$

Due to duality of points and planes in three-space, the same argumentation as in Section 3.1.3.2 applies. We now establish the relationship between the line $\mathcal{L}$ and its dual $\tilde{\mathcal{L}}$. As the vector $\bar{\mathbf{x}} = [\mathcal{L}]_\times \bar{\mathbf{e}}$ for an arbitrary plane $\bar{\mathbf{e}}$ is either the zero-vector or represents a point on the line, we have

$$\forall \bar{\mathbf{x}} = [\mathcal{L}]_\times \bar{\mathbf{e}} \in \mathbb{P}^3 : \quad [\tilde{\mathcal{L}}]_\times \bar{\mathbf{x}} = 0. \tag{3.44}$$

It follows that

$$\left([\tilde{\mathcal{L}}]_\times [\mathcal{L}]_\times\right)^\top = [\tilde{\mathcal{L}}]_\times [\mathcal{L}]_\times = \mathbf{0} \in \mathbb{R}^{4\times 4}. \tag{3.45}$$

The following product fullfills this property

$$\begin{pmatrix} 0 & L_{23} & -L_{13} & L_{12} \\ -L_{23} & 0 & L_{03} & -L_{02} \\ L_{13} & -L_{03} & 0 & L_{01} \\ -L_{12} & L_{02} & -L_{01} & 0 \end{pmatrix} \begin{pmatrix} 0 & L_{01} & L_{02} & L_{03} \\ -L_{01} & 0 & L_{12} & L_{13} \\ -L_{02} & -L_{12} & 0 & L_{23} \\ -L_{03} & -L_{12} & -L_{23} & 0 \end{pmatrix} = \mathbf{0}^{4\times 4}, \tag{3.46}$$

with the Grassmann-Plücker Relation from Equation 3.41. Due to uniqueness of line coordinates (up to scale) we get for the primal Plücker coordinates

$$\mathcal{L} = \left(L_{01}, L_{02}, L_{03}, L_{12}, L_{31}, L_{23}\right)^\top, \tag{3.47}$$

the dual Plücker coordinates

$$\tilde{\mathcal{L}} = \left(L_{23}, -L_{13}, L_{12}, L_{03}, -L_{02}, L_{01}\right)^\top. \tag{3.48}$$

3.1.3.4 Direction and Moment

Projective three-space contains a plane at infinity $\bar{\pi}^{\infty} \cong (0, 0, 0, 1)^{\top}$. The direction of the line is thus the intersection

$$\bar{\mathbf{d}} = \text{meet}(\mathcal{L}, \bar{\pi}^{\infty}) = [\mathcal{L}]_{\times} \cdot \bar{\pi}^{\infty} = \begin{pmatrix} \boldsymbol{d} \\ 0 \end{pmatrix}. \tag{3.49}$$

Dually, we can compute a plane which contains the line $\mathcal{L}$ and the origin via

$$\bar{\mathbf{m}} = \text{join}\left(\mathcal{L}, \begin{pmatrix} 0 \\ 0 \\ 0 \\ 1 \end{pmatrix}\right) = [\tilde{\mathcal{L}}]_{\times} \begin{pmatrix} 0 \\ 0 \\ 0 \\ 1 \end{pmatrix} = \begin{pmatrix} \boldsymbol{m} \\ 0 \end{pmatrix}. \tag{3.50}$$

We call the vectors

$$\boldsymbol{d} = \begin{pmatrix} L_{03} \\ L_{13} \\ L_{23} \end{pmatrix}, \tag{3.51}$$

the direction (sometimes called displacement) and

$$\boldsymbol{m} = \begin{pmatrix} L_{01} \\ -L_{02} \\ L_{12} \end{pmatrix}, \tag{3.52}$$

the moment of the line. The primal and dual Plücker matrices can be written as

$$[\mathcal{L}]_{\times} = \begin{pmatrix} [\boldsymbol{m}]_{\times} & \boldsymbol{d} \\ -\boldsymbol{d}^{\top} & 1 \end{pmatrix}, \tag{3.53}$$

and

$$[\tilde{\mathcal{L}}]_{\times} = \begin{pmatrix} [\boldsymbol{d}]_{\times} & \boldsymbol{m} \\ -\boldsymbol{m}^{\top} & 1 \end{pmatrix}. \tag{3.54}$$

The Grassmann-Plücker relation from Equation 3.41 states that $\boldsymbol{d}$ and $\boldsymbol{m}$ are orthogonal

$$L_{01}L_{23} - L_{02}L_{13} + L_{03}L_{12} = \boldsymbol{d}^{\top}\boldsymbol{m} = 0, \tag{3.55}$$

which is also the condition that $[\mathcal{L}]_{\times} \cdot [\tilde{\mathcal{L}}]_{\times} = \mathbf{0}^{4\times4}$.

3.1.3.5 Geometric Interpretation of Plücker Coordinates

Let $\bar{\mathbf{a}}$ and $\bar{\mathbf{b}}$ denote finite points with $B_3 = A_3 = 1$. Then $\boldsymbol{a} = (A_1, A_2, A_3)^{\top}$ are the coordinates in $\mathbb{R}^3$and $\boldsymbol{b}$ analogously. In this case, the direction can be written as the difference

$$\boldsymbol{d} = \boldsymbol{b} - \boldsymbol{a}, \tag{3.56}$$

and the moment as the cross-product

$$\boldsymbol{m} = \boldsymbol{a} \times \boldsymbol{b}. \tag{3.57}$$

$$[\mathcal{L}]_\times = \begin{pmatrix} 0 & L_{01} & L_{02} & L_{03} \\ -L_{01} & 0 & L_{12} & L_{13} \\ -L_{02} & -L_{12} & 0 & L_{23} \\ -L_{03} & -L_{13} & -L_{23} & 0 \end{pmatrix} = \begin{pmatrix} [\mathbf{m}]_\times & \mathbf{d} \\ -\mathbf{d}^\top & 0 \end{pmatrix}$$

$$\bar{\mathbf{o}} = [\mathcal{L}]_\times \underbrace{[\mathcal{L}]_\times \pi^\infty}_{\bar{\mathbf{d}}=(\mathbf{d}^\top,0)^\top} \cong \begin{pmatrix} [\mathbf{m}]_\times & \mathbf{d} \\ -\mathbf{d}^\top & 0 \end{pmatrix} \begin{pmatrix} \mathbf{d} \\ 0 \end{pmatrix} = \begin{pmatrix} \mathbf{m} \times \mathbf{d} \\ -\mathbf{d}^\top \mathbf{d} \end{pmatrix}$$

$$\bar{\mathbf{v}} = [\tilde{\mathcal{L}}]_\times \underbrace{[\tilde{\mathcal{L}}]_\times \pi^\infty}_{\bar{\mathbf{m}}=(\mathbf{m}^\top,0)^\top} \cong \begin{pmatrix} [\mathbf{d}]_\times & \mathbf{m} \\ -\mathbf{m}^\top & 0 \end{pmatrix} \begin{pmatrix} \mathbf{m} \\ 0 \end{pmatrix} = \begin{pmatrix} \mathbf{m} \times \mathbf{d} \\ \mathbf{m}^\top \mathbf{m} \end{pmatrix}$$

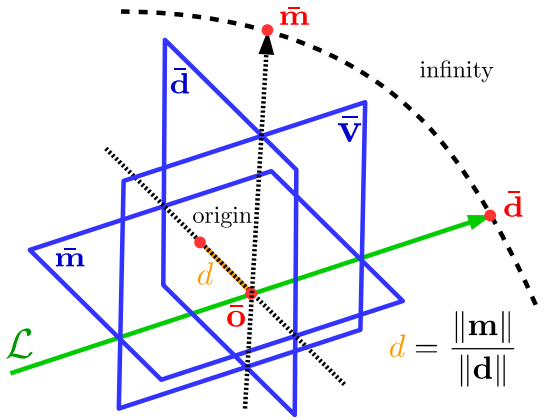

Figure 3.4: Summary of the geometry of lines in space using Plücker coordinates. Note that the line points in the direction $\boldsymbol{d} = (L_{02}, L_{13}, L_{23})^\top$ with moment $\boldsymbol{m} = (-L_{12}, L_{02}, -L_{01})^\top$. The colored symbols in this figure indicate how the vectors are to be interpreted: Green means line, red means point, while blue means plane. For example, the vector $\bar{\mathbf{d}} = (L_{02}, L_{13}, L_{23}, 0)^\top$ can be interpreted as the plane orthogonal to the line containing the origin (blue) or the point at infinity in the direction of the line (red). In other words, the homogeneous coordinates of these two geometric objects are the same. The vector $\bar{\mathbf{m}} = (-L_{12}, L_{02}, -L_{01}, 0)^\top$ can be interpreted as the common plane of the line and the origin, or the point at infinity in the direction of its normal. Finally, the point $\bar{\mathbf{o}}$ is the closest point on the line to the origin and $\bar{\mathbf{v}}$ represents the plane with maximum distance to the origin containing the line. The normal of $\bar{\mathbf{v}}$ points from the origin to the closest point $\bar{\mathbf{o}}$ on the line. In this case, the last coordinate of $\bar{\mathbf{o}}$ and $\bar{\mathbf{v}}$ differs. Interestingly, when we consider the Hessian normal form of the plane $\bar{\mathbf{v}}$, its last coordinate is also the distance of the line to the origin $d = \frac{\|\boldsymbol{m}\|}{\|\boldsymbol{d}\|}$.

From Equation 3.50, we understand that the moment is the normal to the plane, which contains the origin and the line. Observe, that the vector of the point $\bar{\mathbf{d}}$ in Equation 3.49 can also be interpreted as a plane $\bar{\mathbf{d}}$ orthogonal to a finite line through the origin. It follows, that its intersection with the line gives the closest point to the origin

$$\bar{\mathbf{t}} = [\mathcal{L}]_\times [\mathcal{L}]_\times \cdot \bar{\pi}^\infty = \begin{pmatrix} \boldsymbol{d} \times \boldsymbol{m} \\ \|\boldsymbol{d}\|^2 \end{pmatrix}. \tag{3.58}$$

The distance of the line to the origin is therefore

$$d = \frac{\|\boldsymbol{m}\|}{\|\boldsymbol{d}\|}. \tag{3.59}$$

3.2 The Pinhole Camera Model

3.2.1 Central Projection

The projective geometry of photo cameras and X-ray imaging follow the same model. In this work, we will not consider the case when the center of projection is at infinity (i.e. parallel projection) and summarize the information required to understand Chapters 3ff. . As both light rays and X-rays are straight lines, projection can be described by the intercept theorem, as shown in Figure 3.5. Here, a special coordinate system is assumed, where the world X- and Y-axes are parallel to the image plane. Since the pinhole, or focal point, is located between the object and the image plane, the image will appear flipped. We account for this by choosing the u- and v-axis to be parallel to world X- and Y- axis, only pointing in the opposite direction.

Focal Length We can express the mapping of any world point using the intercept theorem. Let f denote the focal length, which is the distance between the image plane and the pinhole. Further, let $(X,\, Y,\, Z)^\top \in \mathbb{R}^3$ be a world point that maps to the image point $(u, v)^\top \in \mathbb{R}^2$, then there exists a simple relationship (cf. Figure 3.5)

$$\begin{pmatrix} u \\ v \end{pmatrix} = \frac{f}{Z} \begin{pmatrix} X \\ Y \end{pmatrix}. \tag{3.60}$$

We can express said relationship as a projective transformation with $\bar{\mathbf{x}} = (X,\, Y,\, Z,\, 1)^\top \in \mathbb{P}^3$ and point $\mathbf{x} \cong (u,\, v,\, w)^\top \in \mathbb{P}^2$ as

$$\mathbf{x} \cong \begin{pmatrix} f \cdot X \\ f \cdot Y \\ Z \end{pmatrix} = \mathbf{P}_f \bar{\mathbf{x}}, \overset{\text{if } Z>0}{\cong} \begin{pmatrix} \frac{f \cdot X}{Z} \\ \frac{f \cdot Y}{Z} \\ 1 \end{pmatrix}, \tag{3.61}$$

with a projection matrix

$$\mathbf{P}_f = \begin{pmatrix} f & & & 0 \\ & f & & 0 \\ & & 1 & 0 \end{pmatrix}. \tag{3.62}$$

The condition $Z > 0$ is met if the point $\bar{\mathbf{x}}$ is in front of the pinhole camera. Note that the pinhole is the origin of three-space $\bar{\mathbf{c}}_f = (0,\, 0,\, 0,\, 1)^\top$ and maps to the zero-vector

$$\mathbf{0} = \mathbf{P}_f \bar{\mathbf{c}}_f. \tag{3.63}$$

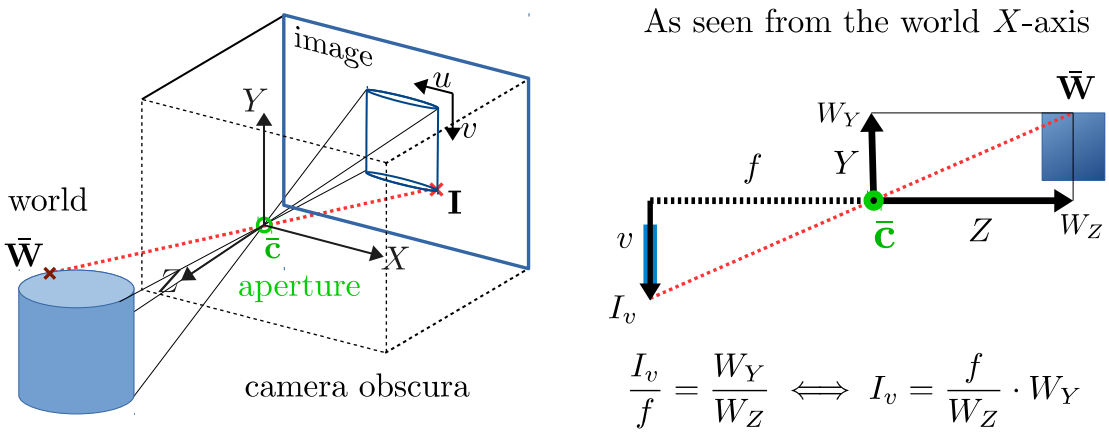

Figure 3.5: The Pinhole Camera. Left: A world point $\bar{\mathbf{x}}$ in coordinates relative to the camera is mapped to the image point $\mathbf{x}$. Right: The image depends linearly on the focal distance between the pinhole and the image plane, as well as the distance of the world point to the pinhole (visualized for the v-axis). Note that the image will be flipped, with the u- and v-axis oriented in the opposite direction as the $X-$ and Y-axes, because the image plane is on the opposite side of the pinhole than the object. Mathematically, however it makes no difference on which side of the pinhole we place a "virtual" image plane.

3.2.1.1 Transformation of a Projection Matrix

To this point we have assumed very specific coordinate systems shown Figure 3.5. In order to accommodate general projections, world and image can be transformed by homographies $\mathbf{T} \in \mathbb{R}^{4\times4}$ and $\mathbf{H} \in \mathbb{R}^{3\times3}$ with

$$\mathbf{x}' \cong \mathbf{H}\mathbf{x} \text{ and } \bar{\mathbf{x}}' \cong \mathbf{T}\bar{\mathbf{x}}, \tag{3.64}$$

where

$$\mathbf{x} = \mathbf{P}\bar{\mathbf{x}}. \tag{3.65}$$

The mapping from original 3D points to transformed image points can be expressed within a single matrix $\mathbf{P}'$

$$\mathbf{x}' = \mathbf{HPT}\bar{\mathbf{x}} = \mathbf{P}'\bar{\mathbf{x}} \text{ where } \mathbf{P}' = \mathbf{HPT} \in \mathbb{R}^{3\times4}. \tag{3.66}$$

However, the transformations are not entirely independent. The result is a 3×4 matrix defined up to positive scale with at most 11 degrees of freedom while $\mathbf{H}$ and $\mathbf{T}$ have 8, respectively, 15 degrees of freedom. The following sections briefly discuss a geometrically meaningful decomposition into 11 parameters of a projection matrix.

3.2.1.2 General Pinhole Camera Model

The RQ-decomposition, a variant of the well-known QR matrix decomposition can be used to quickly separate the so-called intrinsic and extrinsic parameters of a projection matrix. We have

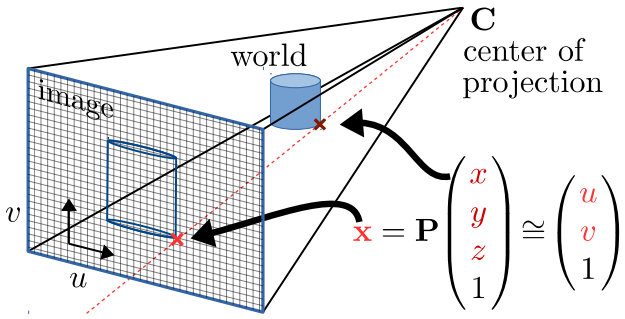

Figure 3.6: Projection of a world point $\bar{\mathbf{x}} \in \mathbb{P}^3$ in X-, Y-, Z-coordinates to the image point $\mathbf{x} \in \mathbb{P}^2$. If $\mathbf{x}$ is finite, it has the pixel coordinates $(u, v)^\top$. Note that the image plane is visualized on the opposite side of the object than the center of projection, which is the case for X-ray imaging.

$$\mathbf{P}{=}\mathbf{K}\,(\mathbf{R}\;\boldsymbol{t}) \;\text{ with }\; \mathbf{K} = \begin{pmatrix} \alpha_u & s & u_0 \\ & \alpha_v & v_0 \\ & & 1 \end{pmatrix}, \tag{3.67}$$

with an upper triangular matrix $\mathbf{K}$ and the rigid transformation $\begin{pmatrix} \mathbf{R} & \boldsymbol{t} \end{pmatrix}$ with a left 3×3 rotation matrix $\mathbf{R}$ (i.e. $\det(\mathbf{R}) > 0$) and right-most column translation vector $\boldsymbol{t}$. After transformation with $\mathbf{R}$ and $\boldsymbol{t}$, the center of projection has moved from the origin to

$$\bar{\mathbf{c}} = \begin{pmatrix} -\mathbf{R}^\top \boldsymbol{t} \\ 1 \end{pmatrix}. \tag{3.68}$$

From Equation 3.63, we can see that the center of projection is in the null space of the projection matrix and, further, that the null-space must be one-dimensional because both $\mathbf{K}$ and $\mathbf{R}$ have full rank

$$\bar{\mathbf{c}} \in \text{null}(\mathbf{P}) \tag{3.69}$$

This thesis will assume a positive center of projection (i.e. neither null nor negative values in the homogeneous coordinate). The remaining parameters are skew parameter s, which is zero for rectangular pixels, the focal length in pixels α_u and α_v, which are equal for square pixels and, finally, the principal point $\boldsymbol{p} = (u_0,\, v_0)^\top$, which is the orthogonal projection of the center of projection to the image. In case of flat-panel detectors and CCDs we can assume square pixels. The principal point is typically close to the center of the image. A detailed analysis of projection matrix composition and decomposition can be found in [Hart 00] and is beyond the scope of this thesis.

3.2.1.3 Backprojection of Image Points

Points on the same line through the center of projection map to the same image point. This line is also called the backprojection ray. It is defined by the center of projection $\bar{\mathbf{c}}$ and any 3D point. Given a pixel location $\mathbf{x} = (u, v, 1)^\top$ we can compute some point distinct from the center of projection $\bar{\mathbf{x}}^+ = \mathbf{P}^+\mathbf{x}$, where $\mathbf{P}^+$ denotes the pseudoinverse of the projection matrix. Its projection is the same image point $\mathbf{P}\bar{\mathbf{x}}^+ = \mathbf{P}\mathbf{P}^+\mathbf{x} = \mathbf{x}$. Thus the Plücker coordinates of the backprojection ray are given by $\mathcal{R} = \text{join}(\bar{\mathbf{x}}^+, \bar{\mathbf{c}})$.

3.2.1.4 Backprojection of Lines in the Image

Intuitively, the backprojection rays of points on a common line in the image are contained in a single backprojection plane. Let $\mathbf{P}$ denote a projection matrix with center of projection $\bar{\mathbf{c}} \in \text{null}(\mathbf{P})$ and let $\mathbf{l}$ denote a 2D line through two image points $\mathbf{a}$ and $\mathbf{b}$. Further, let $\bar{\mathbf{e}}$ denote a plane with the coordinates $\bar{\mathbf{e}} \cong \mathbf{P}^\top \mathbf{l}$. We now show that $\bar{\mathbf{e}}$ is the backprojection of the line $\mathbf{l}$. A plane in space is fully defined by three points that lie on it. The plane $\bar{\mathbf{e}}$ trivially contains the center of projection, since

$$\bar{\mathbf{e}}^\top \bar{\mathbf{c}} = \mathbf{l}^\top \underbrace{\mathbf{P}\bar{\mathbf{c}}}_{=\mathbf{0}} = 0. \tag{3.70}$$

Let $\bar{\mathbf{a}}^+ \cong \mathbf{P}^+\mathbf{a}$ and $\bar{\mathbf{b}}^+ \cong \mathbf{P}^+\mathbf{b}$ denote the backprojection of the image points. We have

$$\bar{\mathbf{e}}^\top \bar{\mathbf{a}}^+ = \mathbf{l}^\top \underbrace{\mathbf{P}\mathbf{P}^+}_{\mathbf{I}_3}\mathbf{a} = \mathbf{l}^\top \mathbf{a}, \tag{3.71}$$

and $\bar{\mathbf{b}}^+$ analogously. The plane $\bar{\mathbf{e}}$ thus contains all three points $\bar{\mathbf{a}}^+$, $\bar{\mathbf{b}}^+$and $\bar{\mathbf{c}}$ and thus both back-projection rays from $\mathbf{a}$ and $\mathbf{b}$. It must therefore be identical to the backprojection plane of the line $\mathbf{l}$.

3.2.2 Anatomy of the Projection Matrix

The geometry of a rotational computed tomography system is commonly described by distance measurements of source and detector. A typical set of parameters is the source-detector distance, the source-iso-center distance, which is the distance to the rotation center, and the detector geometry, as well as misalignment parameters, such as the detector offset and the iso-center offset. One such example can be found in the open-source library RTK[2], which relies on the international standard IEC 61217. The assembly of a projection matrix from a sequence of transformations is straightforward. This section, however, discusses the inverse of how to compute source and detector parameters given a projection matrix.

3.2.2.1 Axis Planes

In the following, let $\bar{\mathbf{p}}^{1\top}$, $\bar{\mathbf{p}}^{2\top}$ and $\bar{\mathbf{p}}^{3\top}$ denote the row 4-vectors of $\mathbf{P}$. We will interpret these three vectors as three planes:

$$\mathbf{x} = \begin{pmatrix} u \\ v \\ d \end{pmatrix} = \mathbf{P}\bar{\mathbf{x}} = \begin{pmatrix} - & \bar{\mathbf{p}}^{1\top} & - \\ - & \bar{\mathbf{p}}^{2\top} & - \\ - & \bar{\mathbf{p}}^{3\top} & - \end{pmatrix} \bar{\mathbf{x}} \tag{3.72}$$

and consider the three special cases, where

$$u = 0 \iff \bar{\mathbf{p}}^{1\top}\bar{\mathbf{x}} = 0, \tag{3.73}$$

$$v = 0 \iff \bar{\mathbf{p}}^{2\top}\bar{\mathbf{x}} = 0, \tag{3.74}$$

$$\text{and} \quad d = 0 \iff \bar{\mathbf{p}}^{3\top}\bar{\mathbf{x}} = 0. \tag{3.75}$$

[2] the reconstruction toolkit, http://www.openrtk.org

Further, let

$$\boldsymbol{m}^1 = (P_{11}, P_{12}, P_{13})^\top, \tag{3.76}$$
$$\boldsymbol{m}^2 = (P_{21}, P_{22}, P_{23})^\top, \tag{3.77}$$
$$\text{and} \quad \boldsymbol{m}^3 = (P_{31}, P_{32}, P_{33})^\top, \tag{3.78}$$

denote the normal vectors to these planes, which are also the row-vectors of the left 3×3 sub-matrix $\mathbf{M}$ of the projections matrix. The center of projection $\bar{\mathbf{c}}$ is the null-space of the projection matrix and lies on all three axis planes. This is visualized in Figure 3.7.

Observe, that the condition $u = 0$ corresponds to the case where $\mathbf{x}$ lies on the v-axis and $\bar{\mathbf{x}}$ could be anywhere along the corresponding backprojection rays. It follows, that $\bar{\mathbf{x}}$ is on the plane containing the image v-axis and the center of projection. Since there exists only one such plane and $\bar{\mathbf{p}}^{1\top}\bar{\mathbf{x}} = 0$ always holds, $\bar{\mathbf{p}}^1$ must be exactly the plane through the center of projection intersecting the image plane in the v-axis. Analogously, $\bar{\mathbf{p}}^2$ must be the plane through the center of projection intersecting the image in the u-axis.

3.2.2.2 Principal Plane

If a point $\bar{\mathbf{x}}$ maps to infinity it follows, first, that its view ray is parallel to the image plane and, second, that $\bar{\mathbf{x}}$ must lie on the plane $\bar{\mathbf{p}}^{3\top}$, the principal plane

$$\begin{pmatrix} u \\ v \\ 0 \end{pmatrix} \cong \mathbf{P}\bar{\mathbf{x}} = \begin{pmatrix} - & \bar{\mathbf{p}}^{1\top} & - \\ - & \bar{\mathbf{p}}^{2\top} & - \\ - & \bar{\mathbf{p}}^{3\top} & - \end{pmatrix} \bar{\mathbf{x}} \Rightarrow \bar{\mathbf{p}}^{3\top}\bar{\mathbf{x}} = 0. \tag{3.79}$$

Please note that in this equation, the projection matrix is decomposed into three homogeneous row vectors. However, the scale factor between these is not arbitrary in Eq. 3.79 as far as the components of the matrix are concerned. In other words, knowledge of the axis planes alone is not enough information to define a projection matrix. The last row $\bar{\mathbf{p}}^{3\top}$ is the principal plane and is parallel to the image passing through the center of projection. It forms and integral part of the projection matrix, since it is used to define depth and to discern points in front and points behind the camera, compare Section 3.2.3.Note that $\boldsymbol{m}^3 = (P_{31}, P_{32}, P_{33})$ is therefore orthogonal to the image plane.

3.2.2.3 Axis Vectors

In case of digital cameras, as well as digital X-ray detectors, the CCD is designed, such that the image u- and v-axes are orthogonal. In that case, the normal vectors to the planes $\bar{\mathbf{p}}^1$ and $\bar{\mathbf{p}}^2$ are

$$\boldsymbol{v} = \boldsymbol{m}^3 \times \boldsymbol{m}^1 \tag{3.80}$$

and

$$\boldsymbol{u} = \boldsymbol{m}^3 \times \boldsymbol{m}^2 \tag{3.81}$$

point in the direction of the image u- and v-axes in three-space. These vectors can be used to quickly find the 3D location of image points, by multiplying them with u and v coordinates and taking into account the origin of the image coordinates relative the the so-called principal point.

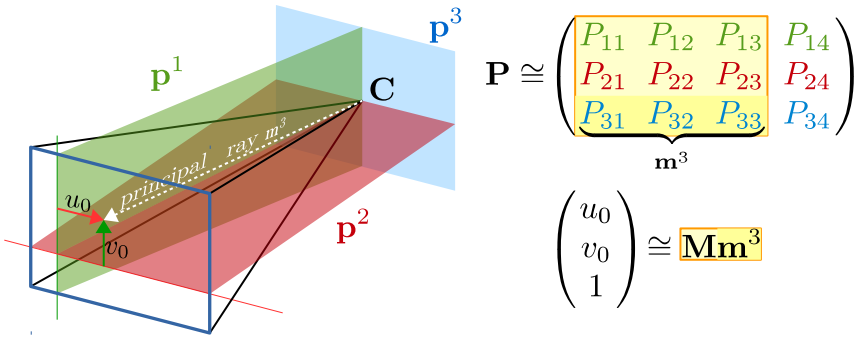

Figure 3.7: Special planes encoded in rows of the projection matrix. Since $\mathbf{P}\bar{\mathbf{c}} = \mathbf{0}$, all three planes contain the center of projection $\bar{\mathbf{c}}$. The $\bar{\mathbf{p}}^1$ plane also contains the image v-axis, while the $\bar{\mathbf{p}}^2$ plane also contains the image u-axis. The $\bar{\mathbf{p}}^3$ plane takes a special role and is also called the principal plane. Its normal $\boldsymbol{m}^3$ is orthogonal to the image plane which it intersects in the principal point $(u_0, v_0, 1)^\top = \mathbf{M}\boldsymbol{m}^3$, where $\mathbf{M} \in \mathbb{R}^{3\times3}$ is the left sub-matrix of $\mathbf{P}$.

3.2.2.4 Principal Point

We know that $\boldsymbol{m}^3$ is orthogonal to the image plane. To find the orthogonal projection of the center of projection to the image, we can compute

$$\mathbf{P} \cdot \left(\bar{\mathbf{c}} + \begin{pmatrix} \boldsymbol{m}^3 \\ 0 \end{pmatrix}\right) = \mathbf{P} \cdot \begin{pmatrix} \boldsymbol{m}^3 \\ 0 \end{pmatrix} = \mathbf{M}\boldsymbol{m}^3 \cong \begin{pmatrix} u_0 \\ v_0 \\ 1 \end{pmatrix}. \tag{3.82}$$

The principal point is typically located close to the center of a pixel representation of an image, unless the image plane is rotated. This may be the result of effect photography with unusual perspectives (such as tilt-shift) or misalignment of the detector.

3.2.3 Oriented Pinhole Camera

3.2.3.1 Depth of Points

Not all points in space are actually seen by a camera. In case of a visible light camera only points in front of the camera are imaged, while in case of X-ray imaging, only objects between X-ray source and detector are imaged. In order to transport these concepts, we need to introduce a notion of oriented distance, which is not projective by nature. For example, depth is not defined for cameras at infinity (i.e. parallel projection). From Section 3.2.2 we know that the principal ray with direction $\boldsymbol{m}^3$ points towards the image plane. As a homogeneous quantity, the projection matrix can be multiplied by scalars. Negative scalars flip the orientation of the vector $\boldsymbol{m}^3$.

To resolve orientation ambiguity, we exploit the determinant $\det(\mathbf{M})$ of the left 3×3 sub-matrix of $\mathbf{P}$. A 3×3 determinant is multi-linear alternating and changes sign when the matrix multiples by -1. Therefore $\det(\mathbf{M})$ changes sign when $\mathbf{P}$ is

multiplied with a negative scalar. This allows us to express the signed distance to the principal plane of a finite world point $\bar{\mathbf{x}} = (X, Y, Z, 1)$

$$\text{depth}(\bar{\mathbf{x}}, \mathbf{P}) = \frac{\text{sign}\left(\det(\mathbf{M})\right)}{\|\boldsymbol{m}^3\|} \cdot \boldsymbol{p}^{3\top}\mathbf{X}, \tag{3.83}$$

where $\text{sign}(\cdot)$ is the signum function and returns $+1$ for a positive argument and -1 for a negative argument. Notice, that $w = \boldsymbol{p}^{3\top}\mathbf{X}$ is the homogeneous coordinate of the image point, which can be found in the last component of the respective vector representation.

We introduce a normalized projection matrix of the form

$$\mathbf{P}^\star = \frac{\text{sign}\left(\det(\mathbf{M})\right)}{\|\boldsymbol{m}^3\|} \cdot \mathbf{P}. \tag{3.84}$$

A finite world point $\bar{\mathbf{x}}$ not on the principal plane projects to

$$\mathbf{x} = \begin{pmatrix} d \cdot u \\ d \cdot v \\ d \end{pmatrix} = \mathbf{P}^\star \bar{\mathbf{x}}. \tag{3.85}$$

where $(u, v)^\top$ are the pixel coordinates of $\mathbf{x}$ and the depth of the world point $\bar{\mathbf{x}}$ is the distance of $\bar{\mathbf{x}}$ to the principal plane $\bar{\mathbf{p}}^3$ of the projection matrix $\mathbf{P}$

$$\text{depth}(\bar{\mathbf{x}}, \mathbf{P}) = d, \tag{3.86}$$

We now have the means to defined that points "in front of a camera" shall be those with positive depth.

3.2.3.2 Detector Plane

If the pixel spacing m (i.e. the distance between pixel centers in millimeters) is known and pixels are square, this information can be used to find the equation of the image plane. W.l.o.g. let $\|\boldsymbol{m}^3\| = 1$, then the last element in $\bar{\mathbf{p}}^3$ is the distance of the principal plane to the origin. To get the image plane, we have to move the principal plane by the focal length in world units. The focal length in pixels α_u or α_v can be obtained via RQ decomposition of $\mathbf{P}$ or directly [Truc 98]

$$\alpha_u = \sqrt{\|\boldsymbol{m}^1\|^2 - u_0}, \tag{3.87}$$

or α_v accordingly. To compute the actual focal distance, we need to divide by the pixel spacing m

$$f = \frac{\alpha_u}{m}. \tag{3.88}$$

The detector plane is thus

$$\bar{\mathbf{i}} = \begin{pmatrix} P_{31} \\ P_{32} \\ P_{33} \\ P_{34} + f \end{pmatrix}. \tag{3.89}$$

3.2.3.3 Detector Coordinate System

The origin of the detector can be found by intersection of the backprojection ray of the image origin and the detector plane. We have

$$\bar{\mathbf{s}} = \text{meet}\left(\text{join}(\mathbf{P}^{+}\,(0,0,1)^{\top}, \bar{\mathbf{c}}), \bar{\mathbf{i}}\right). \tag{3.90}$$

Let the detector have square pixel with spacing m and let the vectors of the points at infinity in the direction of the axis vectors $\bar{\mathbf{u}} \cong \begin{pmatrix} \boldsymbol{u} \\ 0 \end{pmatrix}$ and $\bar{\mathbf{v}} \cong \begin{pmatrix} \boldsymbol{v} \\ 0 \end{pmatrix}$ conveniently scaled to length m and, further, let $\bar{\mathbf{s}}$ have homogeneous coordinate equal to one, then the location of any detector pixel (u, v) can be computed directly via linear combination

$$\bar{\mathbf{x}}_{(u,v)} = \bar{\mathbf{s}} + u \cdot \bar{\mathbf{u}} + v \cdot \bar{\mathbf{v}}. \tag{3.91}$$

We can use this result to visualize the source detector geometry using only the information of a projection matrix, in addition to the spacing m and number of pixels of the detector.

3.3 Epipolar Geometry

3.3.1 Two-View Computer Vision

3.3.1.1 Stereo Vision

The problem of recovering geometric information from two pinhole cameras with different center of projection is called stereo vision. Such images may arise from two cameras looking a the same scene simultaneously (for example the human eye) or by moving a single camera and acquiring two images of a static scene over time (for example a CT scan). In any case, the geometry between the two cameras puts certain constraints on the images of points. See Figure 3.8 for a visualization of this situation. Suppose we have two images with known projection matrices $\mathbf{P}_0$ and $\mathbf{P}_1$ with centers of projection $\bar{\mathbf{c}}_0 \in \text{null}(\mathbf{P}_0)$ and $\bar{\mathbf{c}}_1 \in \text{null}(\mathbf{P}_1)$.

Suppose the point $\mathbf{x}_0 = \mathbf{P}_0\bar{\mathbf{x}}$ in image 0 shows a specific feature of unknown 3D location $\bar{\mathbf{x}}$, perhaps the corner of an object. We may ask, where the corresponding point $\mathbf{x}_1 = \mathbf{P}_1\bar{\mathbf{x}}$ showing the same feature in image 1 is located. Although we do not know the exact location of the world point $\bar{\mathbf{x}}$, we know that it must be located somewhere on the backprojection ray $\mathcal{R} = \text{join}(\mathbf{P}^{+}\bar{\mathbf{x}}, \bar{\mathbf{c}}_0)$, shown in Figure 3.8 in dashed orange. We can forward project all candidate points for $\bar{\mathbf{x}}$ on that ray to image 1, which gives us a line $\mathbf{l}_1$(blue, left). The point $\mathbf{x}_1$ must then be on that line, algebraically $\mathbf{l}_1^{\top}\mathbf{x}_1 = 0$. This section discusses several ways of how to compute such a line $\mathbf{l}_1$, called epipolar line.

3.3.1.2 Epipolar Plane

Note that the construction is symmetric for the two views. We might instead start with a point $\mathbf{x}_1$ in image 1 and end up with an epipolar line $\mathbf{l}_0$ in image 0. Interestingly, the backprojection rays from $\mathbf{x}_0$ and $\mathbf{x}_1$ intersect in the point $\bar{\mathbf{x}}$ and therefore define

a common plane, which also contains both centers of projection $\bar{\mathbf{c}}_0$ and $\bar{\mathbf{c}}_1$. This plane is called epipolar plane. Its intersection with the image planes yields the two corresponding epipolar lines $\mathbf{l}_0$ and $\mathbf{l}_1$. Algebraically, we can represent the epipolar plane via backprojection of the lines, cf. Section 3.2.1.4

$$\bar{\mathbf{e}} = \mathbf{P}_0^\top \mathbf{l}_0 \cong \mathbf{P}_1^\top \mathbf{l}_1. \tag{3.92}$$

Since we can freely choose the world point $\bar{\mathbf{x}}$, there must exist a pencil of epipolar planes. Each of these planes must contain both source positions, therefore, the pencil is defined around the 3D line

$$\mathcal{B} = \mathrm{join}(\bar{\mathbf{c}}_0, \bar{\mathbf{c}}_1), \tag{3.93}$$

which is the line connecting the two camera centers and is contained in any epipolar plane, cf. Figure 3.8. This line is called stereo baseline.

3.3.1.3 Invariance of Epipolar Lines to Transformation of the World

Let $\mathbf{T} \in \mathbb{R}^{4\times4}$ with $\det(\mathbf{T}) > 0$ represent a linear transformation of points in world coordinates (i.e. the object). Further, let $\mathbf{l}_0$ and $\mathbf{l}_1$ denote two corresponding lines in the sense of Equation 3.92. We can apply the transformation $\mathbf{T}$ to the projection matrices directly, according to Section 3.2.1.1. For the transformed epipolar plane $\bar{\mathbf{e}}'$ we have

$$\begin{aligned}
&(\mathbf{P}_0\mathbf{T})^\top \mathbf{l}_0 \cong (\mathbf{P}_1\mathbf{T})^\top \mathbf{l}_1 && (3.94)\\
\iff &\mathbf{T}^\top\mathbf{P}_0^\top \mathbf{l}_0 \cong \mathbf{T}^\top\mathbf{P}_1^\top \mathbf{l}_1 && (3.95)\\
\overset{\mathbf{T}^{-\top}\cdot}{\iff} &\mathbf{P}_0^\top \mathbf{l}_0 \cong \mathbf{P}_1^\top \mathbf{l}_1, && (3.96)
\end{aligned}$$

and pairs of corresponding epipolar lines are invariant to such a transformation. However the corresponding epipolar plane is now the inverse transpose of the original plane

$$\begin{aligned}
&\bar{\mathbf{e}}' \cong \mathbf{T}^\top\mathbf{P}_1^\top \mathbf{l}_1 && (3.97)\\
\iff \quad &\mathbf{T}^{-\top}\bar{\mathbf{e}}' \cong \mathbf{P}_1^\top \mathbf{l}_1 = \bar{\mathbf{e}}. && (3.98)
\end{aligned}$$

Planes in three-space, just like lines, transform with the inverse transpose of point homographies [Coxe 87] (compare Section 3.1.2.5).

3.3.1.4 Invarance of Epipolar Planes to Transformation of the Images

Let $\mathbf{H} \in \mathbb{R}^{3\times3}$ with $\det(\mathbf{H}) > 0$ represent a linear transformation of points in coordinates of image 0. Further, let $\mathbf{l}_0$ and $\mathbf{l}_1$ denote two corresponding lines in the sense of Equation 3.92. From Section 3.1.2.5 we know that the transformed epipolar line $\mathbf{l}_0'$ is

$$\mathbf{l}_0' = \mathbf{H}^{-\top}\mathbf{l}. \tag{3.99}$$

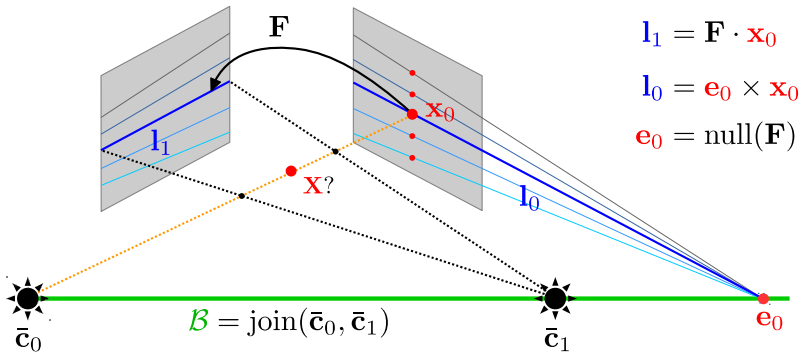

Figure 3.8: Action of the fundamental matrix $\mathbf{F}$ in the epipolar geometry of two pinhole cameras. The baseline $\mathcal{B}$ connects the source positions $\bar{\mathbf{c}}_0$ and $\bar{\mathbf{c}}_1$. By intersection of the baseline with the image planes (shaded gray), we obtain the epipoles (intersection visualized only for $\mathbf{e}_0$). The joining lines of any image point $\mathbf{x}_0$ produces an epipolar line. The corresponding epipolar line $\mathbf{l}_1$ can be obtained by multiplication of $\mathbf{x}_0$ with the fundamental matrix $\mathbf{F}$. Note how the orange dashed line and the baseline form an epipolar plane. By intersection of that plane with the image planes, one obtains the corresponding epipolar lines in three-space.

We can apply the transformation $\mathbf{H}$ to the projection matrix $\mathbf{P}_0$ directly, according to Section 3.2.1.1. For the transformed epipolar plane $\bar{\mathbf{e}}'$ we have

$$\begin{aligned} \bar{\mathbf{e}}' &\cong (\mathbf{H}\mathbf{P}_0)^\top \mathbf{l}'_0 && (3.100)\\ &\cong \mathbf{P}_0^\top \mathbf{H}^\top \mathbf{H}^{-\top} \mathbf{l} && (3.101)\\ &\cong \mathbf{P}_0^\top \mathbf{l}_0 && (3.102)\\ &\cong \bar{\mathbf{e}}. && (3.103) \end{aligned}$$

3.3.2 Geometry of the Stereo Baseline

3.3.2.1 Fundamental Matrix

Epipolar geometry is usually described by a single 3×3 matrix $\mathbf{F}$, called fundamental matrix, which maps any point $\mathbf{x}_0$ on one detector to a line $\mathbf{l}_1$ on the other detector, cf. Figure 3.8. This matrix is commonly used in computer vision to search for corresponding points and triangulate 3D geometry. We present a brief derivation, which takes our special definition of oriented pinhole cameras into account and establish the relationship to the Plücker coordinates of the baseline.

Suppose that the same world point is seen by two cameras as $\mathbf{x}_0 \cong \mathbf{P}_0\bar{\mathbf{x}}$ and $\mathbf{x}_1 \cong \mathbf{P}_1\bar{\mathbf{x}}$. The epipolar line $\mathbf{l}_1$ is the projection of the backprojection ray $\mathcal{R} \cong \text{join}(\mathbf{P}_0^+\mathbf{x}_0, \bar{\mathbf{c}}_0)$ to the other detector. Any line is fully defined by two distinct points that lie on it. Since every backprojection ray necessarily passes through the center of projection, we immediately know one point $\mathbf{e}_1 \cong \mathbf{P}_1\bar{\mathbf{c}}_0$ on the line $\mathbf{l}_1$. We call this point epipole. A second point is obtained by backprojection of $\mathbf{x}_0$ according to $\bar{\mathbf{x}}^+ \cong \mathbf{P}^+\mathbf{x}_0$. By definition of the pseudoinverse $\mathbf{I}_3 = \mathbf{P}\mathbf{P}^+$ the point $\bar{\mathbf{x}}^+$ must be located on the backprojection ray $\mathbf{x}_0 \cong \mathbf{P}\bar{\mathbf{x}}^+$ and it must also be distinct from from $\bar{\mathbf{c}}_0$, since $\bar{\mathbf{c}}_0$ is in the null-space of $\mathbf{P}_0$.

We have just found two points on the backprojection ray, namely $\bar{\mathbf{c}}_0$ and $\bar{\mathbf{x}}^+$. We call the join of their projections the epipolar line

$$\mathbf{l}_1 \cong \mathbf{P}_1\bar{\mathbf{c}}_0 \times \mathbf{P}_1\mathbf{P}_0^+\mathbf{x}_0 = \left([\mathbf{P}_1\bar{\mathbf{c}}_0]_\times \mathbf{P}_1\mathbf{P}_0^+\right)\mathbf{x}_0 \tag{3.104}$$

for the fundamental matrix for the projections $(\mathbf{P}_0, \mathbf{P}_1)$

$$\mathbf{F}_0^1 \cong [\mathbf{P}_1\bar{\mathbf{c}}_0]_\times \mathbf{P}_1\mathbf{P}_0^+. \tag{3.105}$$

Likewise, the corresponding epipolar line is

$$\mathbf{l}_0 \cong \left([\mathbf{P}_0\bar{\mathbf{c}}_1]_\times \mathbf{P}_0\mathbf{P}_1^+\right)\mathbf{x}_1. \tag{3.106}$$

An oriented epipolar plane $\bar{\mathbf{e}}$ is readily computed via the backprojection of the corresponding epipolar lines $\mathbf{l}_0$ or $\mathbf{l}_1$ respectively as

$$\bar{\mathbf{e}} \cong \mathbf{P}_0^\top \mathbf{l}_0 \cong \mathbf{P}_1\mathbf{l}_1 \tag{3.107}$$

$$\iff \forall \bar{\mathbf{x}} \in \mathbb{P}^{3+} : \ \mathbf{P}_0^\top [\mathbf{P}_0\bar{\mathbf{c}}_1]_\times \mathbf{P}_0\bar{\mathbf{x}} \cong \mathbf{P}_1^\top [\mathbf{P}_1\bar{\mathbf{c}}_0]_\times \mathbf{P}_1\bar{\mathbf{x}}. \tag{3.108}$$

Using the epipolar plane for any world point $\bar{\mathbf{x}}$, we can express the relationship between the epipoles

$$\mathbf{P}_0^\top [\mathbf{P}_0\bar{\mathbf{c}}_1]_\times \mathbf{P}_0 \cong \mathbf{P}_1^\top [\mathbf{P}_1\bar{\mathbf{c}}_0]_\times \mathbf{P}_1 \tag{3.109}$$

$$\mathbf{P}_1^{+\top}\mathbf{P}_0^\top [\mathbf{P}_0\bar{\mathbf{c}}_1]_\times \mathbf{P}_0\mathbf{P}_1^+ \cong [\mathbf{P}_1\bar{\mathbf{c}}_0]_\times. \tag{3.110}$$

Substitution yields

$$\begin{aligned} \mathbf{F}_0^1 &\cong [\mathbf{P}_1\bar{\mathbf{c}}_0]_\times \mathbf{P}_1\mathbf{P}_0^+ \\ &\cong \mathbf{P}_1^{+\top}\mathbf{P}_0^\top [\mathbf{P}_0\bar{\mathbf{c}}_1]_\times \underbrace{\mathbf{P}_0\mathbf{P}_1^+\mathbf{P}_1\mathbf{P}_0^+}_{\mathbf{I}_3} \\ &\cong -\mathbf{F}_1^{0\top}. \end{aligned} \tag{3.111}$$

As a result and in accordance to Laveau et al. [Lave 96], we see that the oriented fundamental matrix for the cameras $(\mathbf{P}_0, \mathbf{P}_1)$ is the negative transpose of the fundamental matrix for the cameras $(\mathbf{P}_1, \mathbf{P}_0)$. According to Section 3.2.3, the epipolar $\mathbf{P}_1\bar{\mathbf{c}}_0$ is positive exactly if $\bar{\mathbf{c}}_0$ is in front of $\mathbf{P}_1$. From our definition of the pinhole camera model, it follows directly that a positive $\bar{\mathbf{x}}^+ = \mathbf{P}_0^+\mathbf{x}_0$ is in front of the camera if and only if $\mathbf{x}_0$ is positive. In any case $\mathcal{R}$ consistently points towards the detector.

3.3.2.2 Fundamental Matrix and Dual Plücker Matrix of the Baseline

The orientation of epipolar lines determines the orientation of the epipolar plane. For a discussion of orientation and epipoles not limited to the oriented pinhole camera used in this thesis see the paper by Chum et al. [Chum 03]. Via the fundamental matrix we get for $\mathbf{l}_0$ and $\mathbf{l}_1$ consistently

$$\bar{\mathbf{e}} \cong \mathbf{P}_0^\top \mathbf{l}_0 \cong \mathbf{P}_0^\top \mathbf{F}_1^0 \mathbf{x}_1, \cong \underbrace{\mathbf{P}_0^\top \mathbf{F}_1^0 \mathbf{P}_1}_{[\tilde{\mathcal{B}}]_\times} \bar{\mathbf{x}} \tag{3.112}$$

$$\cong \mathbf{P}_1^\top \mathbf{l}_1 \cong \mathbf{P}_1^\top \mathbf{F}_0^1 \mathbf{x}_0 \cong \overbrace{\mathbf{P}_1^\top \mathbf{F}_0^1 \mathbf{P}_0} \bar{\mathbf{x}}, \tag{3.113}$$

where the anti-symmetric 4×4 matrix $[\tilde{\mathcal{B}}]_\times$ maps points in $\mathbb{P}^3$ to planes in $\mathbb{P}^3$. It is a Plücker representation according to Section 3.1.3.3 of a dual line through the camera centers, also called the baseline in stereo vision. It can be represented as a 6-vector of Plücker coordinates $\mathcal{B}$ according to Equation 3.40 with

$$[\tilde{\mathcal{B}}]_\times \cong \mathbf{P}_1^\top \mathbf{F}_0^1 \mathbf{P}_0 = -\mathbf{P}_0^\top \mathbf{F}_0^{1\top} \mathbf{P}_1 = \mathbf{P}_0^\top \mathbf{F}_1^0 \mathbf{P}_1, \tag{3.114}$$

which is the dual to $[\mathcal{B}]_\times \cong \bar{\mathbf{c}}_1 \bar{\mathbf{c}}_0{}^\top - \bar{\mathbf{c}}_0 \bar{\mathbf{c}}_1{}^\top$, compare Equation 3.39. We have not been able to find this derivation in literature.

CHAPTER 4

Epipolar Consistency

We have discussed in Section 2.4.1 how John's equation can be used to express a cone-beam consistency condition for linear motion of the source, compare the LTC in Equation 2.67. Section 3.3.1.1 discussed how certain lines in projection images of two source-detector geometries are related through a common plane. This chapter will bring these two seemingly independent topics together. Firstly, the geometry of the mentioned consistency condition is an instance of epipolar geometry. Secondly, the consistency condition generalizes to arbitrary cone-beam geometries by using the geometrical tools discussed in Chapter 3 and addressing the following restrictions of LTC:

1. The source position lies in the $z = 0$ plane, parallel to the detector in the $z = 1$ plane.
2. The redundant line integral in Equation 2.67 is in special coordinates, where the direction of integration is parallel to the direction of motion $\boldsymbol{t}$.
3. The projection data is weighted by the inverse distance of each detector pixel to the source, in Equation 2.53.

The following Sections 4.1.1.2 and 4.1.1.3 show that a detector can be virtually rotated and translated by distortion of existing images. Section 4.1.2.3 thus derives an algorithm for fan-beam consistency condition to re-project an arbitrary pair of X-ray images into the special configuration of Equation 2.67. We present a practical implementation of this algorithm by means of a weighted integration on the original images, without a re-projection step that is expensive in terms of both time and memory.

Finally in Section 4.2.1, we review Grangeat's theorem which states that a certain derivative of a line integral in a projection image is related to a corresponding derivative of a plane integral through the object. The theorem was initially applied to reconstruct a 3D object via Radon intermediate functions (i.e., filtered line-integrals over projection images). Since corresponding epipolar lines are related via exactly

the same such plane, we can use the theorem to express a very similar consistency condition to the latter. Again, we present a practical algorithm that benefits from the elegance of epipolar geometry and extraordinarily fast evaluation time due to the pre-computation of Radon intermediate functions. In this context, a third option of epipolar consistency using the ramp filter is presented and all three variants are compared.

4.1 Stereo Rectification for Cone-Beam Consistency

4.1.1 John's Equation and Stereo Rectification

4.1.1.1 Fan-Beam Consistency within Epipolar Planes

We begin with a derivation of the transformations required to make the condition in Section 2.4.1 applicable to arbitrary cone-beam projections. A re-projection to a virtual detector for evaluation of this DCC has been suggested already by Levine at al. [Levi 10] and first implemented by Lesaint et al. [Lesa 17a]. A similar approach even considering epipolar lines has been used already by Brandt et al. [Bran 13]. Since the DCC then applies to a plane intersecting two general cone-beam projections, it will be referred to as fan-beam consistency (FBCC) in the following. This is intuitive, since epipolar planes intersect each cone in a 2D fan of rays. Aichert et al. [Aich 18b] later made the connection to the well-understood algorithm in stereo computer vision called rectification. Rectification is the first step for the computation of a depth-map from two visible-light images [Laza 08] and simplifies disparity estimation to a correspondence search along the horizontal image axis. Stereo rectification is the process by which two rectifying homographies are applied to a pair of general projection images to produce identical corresponding epipolar lines which are parallel to the horizontal image axis. In other words, rectification is determined up to a shearing transformation which leaves horizontal lines constant [Loop 99]. This case is the epipolar geometry for motion parallel to the image plane up to horizontal shearing of both images. If no shearing were applied, this would be exactly the geometry of the X-ray transform as it was introduced by John assumes X-ray sources moving on a plane parallel to a single static detector.

The consistency condition for a linear source motion is applicable to any detector plane parallel to the line of motion (baseline) which was assumed to coincide with the u-axis. In this case, we are dealing with a special instance of the rectification problem, where line integrals are not invariant to shearing and we want pixels on the virtual detector to be square. This leaves only two degrees of freedom: the orthogonal direction to the baseline which defines the v-axis of the virtual detector and the distance of the virtual detector plane. The moment of the stereo baseline (cf. Section 3.3.2) is a good choice for the virtual v-axis, since the object is typically centered in the origin. In case of a circular trajectory, it coincides with the rotation axis, which has been suggested by Lesaint et al. [Lesa 17a].

The following sections express a rectification algorithm via translation and rotation in 3D, which aligns the image u-axis with the baseline direction and the v-axis with the baseline moment. We thereby show that we can virtually re-position the

detector, while preserving pixel shape and source positions. All of this can be done virtually by projectively distorting an existing projection image. This section is loosely based on Aichert et al. [Aich 18b], but extended by expressing the rectification as a 3D similarity transformation and by using an elegant way to compute the Jacobian [Lesa 18b].

4.1.1.2 Rotation of the Detector about the Center of Projection

The following section shows that re-projection to a virtual detector plane is in fact a rotation of the detector. This fact is obvious considering that such rotated images share the same source position and thus represent the same bundle of light rays. Virtual rotation can be applied to an existing projection image, after acquisition. Consider a source-detector geometry given by RQ-decomposition of the projection matrix (cf. Section 3.2.1.2)

$$\mathbf{P} = \mathbf{K}\,[\mathbf{R}|\boldsymbol{t}] \in \mathbb{R}^{3\times 4}. \tag{4.1}$$

Let the homography of three-space $\mathbf{T}^\star \in \mathbb{R}^{4\times 4}$ with $\det(\mathbf{T}^\star) > 0$ describe a rotation $\mathbf{R}^\star \in \mathbb{R}^{3\times 3}$ about the center of projection $\boldsymbol{c} = -\mathbf{R}^\top \boldsymbol{t} \in \mathbb{R}^3$. We have

$$\mathbf{T}^\star = \begin{pmatrix} \mathbf{R}^\star & \boldsymbol{t}^\star \\ & 1 \end{pmatrix}, \tag{4.2}$$

where $\boldsymbol{t}^\star$ shall be chosen such that it leaves $\bar{\mathbf{c}}$ constant

$$\begin{aligned} & \mathbf{T}^\star \bar{\mathbf{c}} = \bar{\mathbf{c}} \\ \iff\ & \boldsymbol{t}^\star = \boldsymbol{c} - \mathbf{R}^\star \boldsymbol{c} \\ & \quad = \mathbf{R}^\star \mathbf{R}^\top \boldsymbol{t} - \mathbf{R}^\top \boldsymbol{t}. \end{aligned} \tag{4.3}$$

In other words, the transformed projection matrix

$$\begin{aligned} \mathbf{P}^\star =& \mathbf{K}\,[\mathbf{R}|\boldsymbol{t}]\,\mathbf{T}^\star \\ \overset{(4.3)}{=}& \mathbf{K}\left[\mathbf{R}\mathbf{R}^\star|\mathbf{R}\mathbf{R}^\star\mathbf{R}^\top\boldsymbol{t} - \mathbf{R}\mathbf{R}^\top\boldsymbol{t} + \boldsymbol{t}\right] \\ =& \mathbf{K}\left[\mathbf{R}\mathbf{R}^\star|\mathbf{R}\mathbf{R}^\star\mathbf{R}^\top\boldsymbol{t}\right], \end{aligned} \tag{4.4}$$

preserves the center of projection

$$\begin{aligned} \boldsymbol{c}^\star &= -\left(\mathbf{R}\mathbf{R}^\star\right)^\top \mathbf{R}\mathbf{R}^\star\mathbf{R}^\top\boldsymbol{t} \\ &= -\mathbf{R}^\top\boldsymbol{t} \\ &= \boldsymbol{c}. \end{aligned}$$

When two projection images share a common center of projections, it follows that each backprojection ray for a pixel from an image acquired by one, has a corresponding pixel in the image of the other. We will now establish the mapping from pixels in one projection image to the other. There exists a linear transformation $\mathbf{H} \in \mathbb{R}^{3\times 3}$ for which we can write

$$\begin{aligned}\mathbf{P}^\star =& \mathbf{K}\left[\mathbf{R}\mathbf{R}^\star|\mathbf{R}\mathbf{R}^\star\mathbf{R}^\top\boldsymbol{t}\right]\\ =& \mathbf{K}\left[\mathbf{R}\mathbf{R}^\star\mathbf{R}^\top\mathbf{R}|\mathbf{R}\mathbf{R}^\star\mathbf{R}^\top\boldsymbol{t}\right]\\ =& \mathbf{K}\mathbf{R}\mathbf{R}^\star\mathbf{R}^\top\left[\mathbf{R}|\boldsymbol{t}\right]\\ =& \underbrace{\mathbf{K}\mathbf{R}\mathbf{R}^\star\mathbf{R}^\top\mathbf{K}^{-1}}\mathbf{K}\left[\mathbf{R}|\boldsymbol{t}\right]\\ =& \qquad \mathbf{H}\cdot\mathbf{P},\end{aligned} \tag{4.5}$$

with

$$\mathbf{H} = \mathbf{K}\mathbf{R}\mathbf{R}^\star\mathbf{R}^\top\mathbf{K}^{-1}. \tag{4.6}$$

In other words, a rotation about the image center can be simulated by a distortion of an existing projection image with the homography $\mathbf{H}$ according to Equation 4.6.

4.1.1.3 Translation of the Detector In- and Out-of-plane

Given intrinsic parameters

$$\mathbf{K} = \begin{pmatrix} \alpha_u & & u_0 \\ & \alpha_v & v_0 \\ & & 1 \end{pmatrix}, \tag{4.7}$$

we now consider the effect of a similarity transformation of the image

$$\mathbf{H} = \begin{pmatrix} s & & t_u \\ & s & t_v \\ & & 1 \end{pmatrix}, \tag{4.8}$$

according to

$$\begin{aligned}\mathbf{H}\mathbf{P} =& \mathbf{H}\mathbf{K}\left[\mathbf{R}|\boldsymbol{t}\right]\\ =& \begin{pmatrix} s\alpha_u & & su_0 + t_u \\ & s\alpha_v & sv_0 + t_v \\ & & 1 \end{pmatrix}\left[\mathbf{R}|\boldsymbol{t}\right].\end{aligned}$$

While t_u and t_v obviously translate the detector within the detector plane (in pixels), the scaling s can be interpreted according to Section 3.2.3.2 as motion of the detector in the direction of the principal ray, i.e., orthogonal to the detector plane and by a distance of

$$t_Z = f - sf. \tag{4.9}$$

In conclusion, can simulate both arbitrary rotation, see Section 4.1.1.2, and arbitrary translation of the detector by distortion, respectively similarity transformation of an existing image. This proves the existence of a rectifying transformation as suggested in Section 4.1.1 by simulating projections of the same object from the same source position, merely with a different detector pose. In the following subsection, we will achieve the same result by actual re-projection onto a virtual detector. This demonstrates the connection to Lesaint et al. [Lesa 17a].

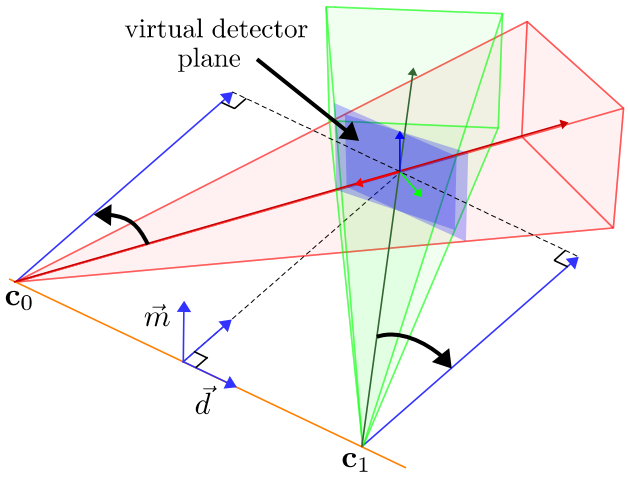

Figure 4.1: The stereo baseline connecting $\bar{\mathbf{c}}_0$ and $\bar{\mathbf{c}}_1$ and its relation to the virtual detector plane (blue). Note how the pincipal axes are rotated (black arrow) to become orthogonal to the virtual detector. The virtual image plane is parallel to the baseline Plücker moment and direction.

4.1.2 Pairwise Fan-beam Consistency (FBCC)

4.1.2.1 Rectification by Re-Projection

In the following we show how central projection from a point $\bar{\mathbf{c}} \in \mathbb{P}^3$ to a virtual detector plane $\bar{\mathbf{e}} \in \mathbb{P}^3$ can be written as single matrix $\mathbf{T}_{\bar{\mathbf{c}}}^{\bar{\mathbf{e}}} \in \mathbb{R}^{4\times4}$ acting on homogeneous three-points. We go on to define a coordinate system on that plane and compute rectifying homographies from two projection matrices.

We express the projection of a point $\bar{\mathbf{x}} \in \mathbb{P}^3$ to a point $\bar{\mathbf{x}}' = \mathbf{T}_{\bar{\mathbf{c}}}^{\bar{\mathbf{e}}}\bar{\mathbf{x}} \in \mathbb{P}^3$ as the intersection of the plane $\bar{\mathbf{e}}$ with the line $\mathcal{R}$ through the points $\bar{\mathbf{c}}$ and $\bar{\mathbf{x}}$. Using the Plücker matrix from Section 3.1.3.2 of the line $[\mathcal{R}]_\times = \bar{\mathbf{x}}\bar{\mathbf{c}}^\top - \bar{\mathbf{c}}\bar{\mathbf{x}}^\top$ we can immediately compute the intersection

$$\begin{aligned}[\mathcal{R}]_\times\bar{\mathbf{e}} &= \bar{\mathbf{c}}\bar{\mathbf{x}}^\top\bar{\mathbf{e}} - \bar{\mathbf{x}}\bar{\mathbf{c}}^\top\bar{\mathbf{e}} \\ &= \left(\mathbf{I}_4(\bar{\mathbf{c}}^\top\bar{\mathbf{e}}) - \bar{\mathbf{c}}\bar{\mathbf{e}}^\top\right)\bar{\mathbf{x}} \\ &= \mathbf{T}_{\bar{\mathbf{c}}}^{\bar{\mathbf{e}}}\bar{\mathbf{x}}.\end{aligned}$$

Note that $\mathbf{I}_4(\bar{\mathbf{c}}^\top\bar{\mathbf{e}})$ is simply a 4×4 diagonal matrix of $\bar{\mathbf{c}}^\top\bar{\mathbf{e}}$. We obtain the projection

$$\mathbf{T}_{\bar{\mathbf{c}}}^{\bar{\mathbf{e}}} = \mathbf{I}_4\bar{\mathbf{c}}^\top\bar{\mathbf{e}} - \bar{\mathbf{c}}\bar{\mathbf{e}}^\top, \tag{4.10}$$

where $\mathbf{I}_4$ denotes the 4×4 identity matrix. Note that $\mathbf{T}_{\bar{\mathbf{c}}}^{\bar{\mathbf{e}}}$ is rank-deficient and is not a homography. Neither is $\mathbf{T}_{\bar{\mathbf{c}}}^{\bar{\mathbf{e}}}$ a projection matrix, for we have not established a 2D image coordinate system on the plane $\bar{\mathbf{e}}$.

4.1.2.2 Rectification by Re-Projection

Before we define the detector coordinate axes, we need to discuss how to choose a virtual detector plane $\bar{\mathbf{e}}$. Consider two X-ray source-detector geometries defined

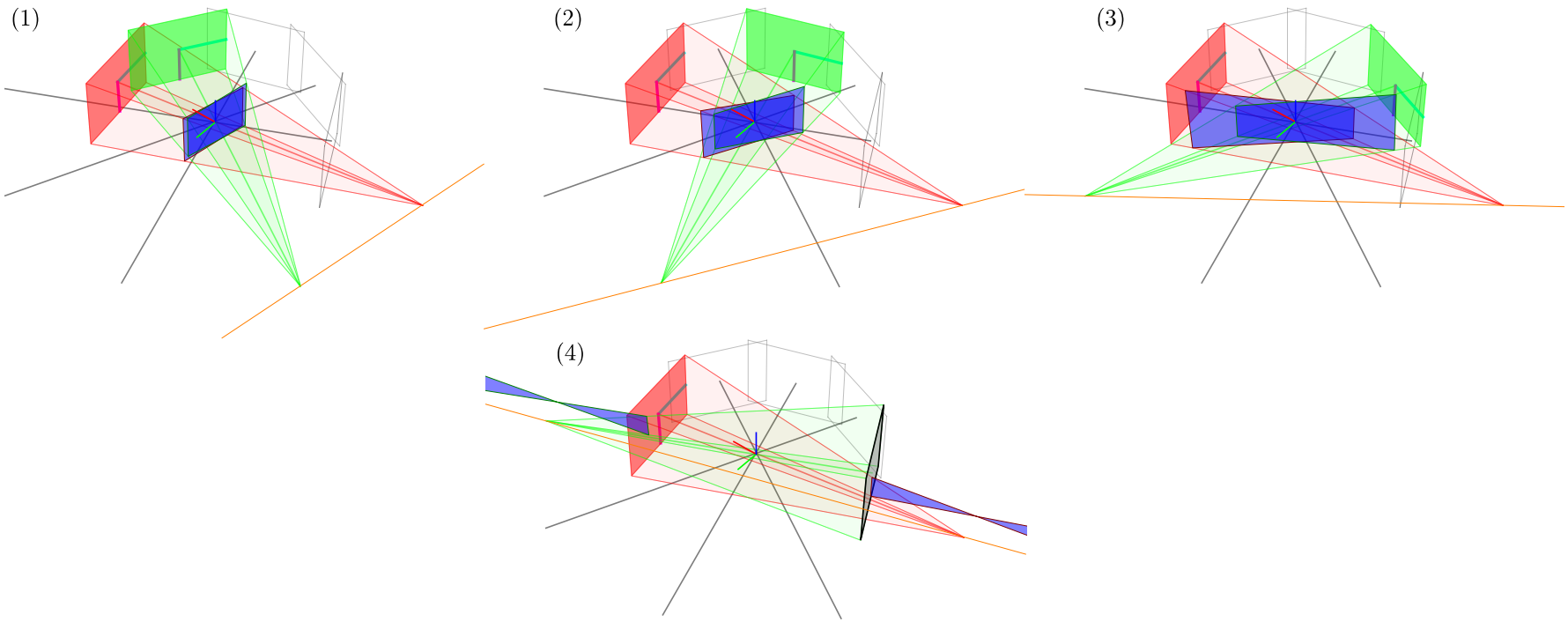

Figure 4.2: Rectified projection data is subject to increasingly strong distortion as the primary angle difference between the two projections increases. Example of a typical circular CT trajectory of a Siemens Artis Zeego from left to right: (1) little distortion up to $\approx 45°$, (2) considerable distortion at $\approx 90°$, (3) method is beginning to break down after $\approx 135°$, and (4) rectification not sensible for opposing views.

by the projection matrices $\mathbf{P}_0, \mathbf{P}_1 \in \mathbb{R}^{3\times4}$. Recall that two rectified homographies $\mathbf{H}_0, \mathbf{H}_1 \in \mathbb{R}^{3\times3}$ shall be applied to projection images $\mathbf{H}_0\mathbf{P}_0$ and $\mathbf{H}_1\mathbf{P}_1$ such that their virtual image planes are parallel to the baseline and corresponding epipolar lines are equal and parallel to the u-axis.

Assuming that the iso-center is approximately in the coordinate origin, then a good choice of virtual detector plane is when the v-axis points in the direction of the baseline moment. This virtual detector plane is

$$\bar{\mathbf{e}} \cong \begin{pmatrix} \mathring{\boldsymbol{d}} \times \mathring{\boldsymbol{m}} \\ 0 \end{pmatrix} \in \mathbb{P}^3, \tag{4.11}$$

where

$$\mathring{\boldsymbol{m}} = \frac{\boldsymbol{m}}{\|\boldsymbol{m}\|} \in \mathbb{S}^2 \tag{4.12}$$

is the unit vector in the direction of the Plücker line moment of the baseline and

$$\mathring{\boldsymbol{d}} = \frac{\boldsymbol{d}}{\|\boldsymbol{d}\|} \in \mathbb{S}^2 \tag{4.13}$$

the unit vector in the direction of the baseline, accordingly. Note that $\mathring{\boldsymbol{m}}$ is also the normal of the plane containing both line and origin. In case of a circular trajectory, this would also be the normal to the plane of rotation, for which the v-axis typically points in the direction of the v-axis of all original projection images. Since the u-axis must point in the direction of the baseline, we establish a 2D coordinate frame for points in the plane $\bar{\mathbf{e}}$ with 3D coordinate axis directions $\mathring{\boldsymbol{d}}$ and $\mathring{\boldsymbol{m}}$ according to

$$\mathbf{S} = \begin{pmatrix} \mathring{\boldsymbol{d}}^\top & 0 \\ \mathring{\boldsymbol{m}}^\top & 0 \\ \mathbf{0} & m \end{pmatrix} \in \mathbb{R}^{3\times4}. \tag{4.14}$$

with some virtual pixel size m in mm. From Section 3.2.3.2 we know that the pixel size effectively defines the distance of the detector plane to the source. In this manner, $m = \frac{\|\boldsymbol{m}\|}{\|\boldsymbol{d}\|}$ would scale the pixel to the same size and the distance of the origin to the baseline. This corresponds exactly to the geometry described in 2.4.1. In our experiments we choose $m = 1$ and note that Equation 2.67 uses a normalized X-ray transform according to Equation 2.2. Recall that LTC acts on the normalized X-ray transform which is weighted by the distance of each pixel to the source. Since this distance is measured in units of the image (i.e., pixels), we can move the detector forward and backward in this manner while the scale factors (i.e., pixel size) can be found on both sides of an equality and thus cancel out.

Given an original image with projection matrix $\mathbf{P}_0$ and source position $\bar{\mathbf{c}}_0 \in \operatorname{null}(\mathbf{P}_0)$, let $\mathbf{T}_{\bar{\mathbf{c}}}^{\bar{\mathbf{e}}} \in \mathbb{R}^{4\times4}$ denote the central projection through $\bar{\mathbf{c}}_0$ to 3D points on the virtual detector plane $\bar{\mathbf{e}}$ and $\mathbf{S}$ defined its 2D coordinate system. We understand that a point on the backprojection ray of a pixel $\mathbf{x}$ can be computed by multiplication with the pseudo-inverse $\mathbf{P}^+$. In consequence, the homography

$$\mathbf{H}_0 = \mathbf{S}\mathbf{T}_{\bar{\mathbf{c}}_0}^{\bar{\mathbf{e}}}\mathbf{P}_0^+ \in \mathbb{R}^{3\times3}, \tag{4.15}$$

directly relates pixels from the original image to pixels in the virtual detector plane $\bar{\mathbf{e}}$. This situation is visualized in Figure 4.1. We can rectify two projections by application of the homographies

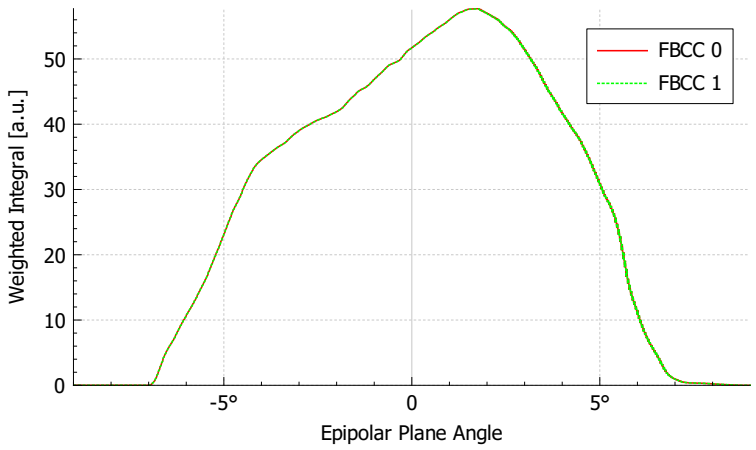

Figure 4.3: Fan-beam consistency condition [Levi 10] as implemented in the original images. The computation of the rectified images in Figure 4.4 is avoided, but the curves are identical to a weighted summation over the intensity in these images. The two curves overlap almost perfectly (hence the difficult visualization).

$$\mathbf{H}_0 \text{and } \mathbf{H}_1 = \mathbf{S}\mathbf{T}_{\bar{\mathbf{c}}_1}^{\bar{\mathbf{e}}}\mathbf{P}_1^{+}, \tag{4.16}$$

accordingly.

4.1.2.3 Rectification by Re-Projection

Figure 4.2 shows 3D visualizations of source-detector geometries for several examples. Note that the images are increasingly distorted. While it is correct to apply the homographies to the pixel representation of projection images and compare sums over horizontal images lines, this algorithm remains inefficient [Aich 18b]. The rectified images must have small pixel size for proper sampling and the process requires considerable amounts of time and memory. Also note, that rectification must be applied to each and every pair of projection images. For $n = 133$ projections, there are as many as $\frac{(133-1)\cdot 133}{2} = 8778$ pairs of projections.

In the following, we present a practical algorithm to compute FBCC. Recall from Section 3.1.2.5 that lines transform with the inverse transpose of point homographies

$$\mathbf{l}' \cong \mathbf{H}^{-\top}\mathbf{l}. \tag{4.17}$$

Since we sample in the domain of epipolar lines (α', τ') the virtual detector plane

$$\mathbf{l} \cong \mathbf{H}^{\top}\mathbf{l}' = \mathbf{H}^{\top}\begin{pmatrix}\sin(\alpha')\\ -\cos(\alpha')\\ -\tau'\end{pmatrix}. \tag{4.18}$$

While the results shown in this work rely on the algorithm described in Aichert et al. [Aich 18b], we note that Lesaint et al. [Lesa 18b] has since shown that the Jacobian determinant of integrating over lines in a perspective distorted image can be computed more simply

$$J_{\mathbf{H}}(u,v) = \frac{\det(\mathbf{H})}{\left|\boldsymbol{h}_3^{\top}(u,v,1)^{\top}\right|}, \tag{4.19}$$

where $\boldsymbol{h}_3$ is the last row-vector of $\mathbf{H}$ and u, v is the current pixel position on the line. The two formulations are numerically identical but Lesaint et al. is considerably more compact. On top of that, Lesaint et al. [Lesa 18a] has since shown that $J_{\mathbf{H}}(u, v)$ is an additional weight inside the integrals with the distance of each pixel to the epipoles. This does not affect algorithm complexity but further simplifies implementation.

Algorithm 4.1: Radon transform of a projectively distorted image $\mathbf{H}f$ for a line $\mathbf{l}' = \mathbf{H}^{-\top}\mathbf{l}$ from the original image f.

- **input**
  - Line $\mathbf{l}' = (\sin(\alpha'), -\cos(\alpha'), -\tau)^\top$
  - Homography $\mathbf{H} \in \mathbb{R}^{3\times3}$ (as in Equation 4.16).

---

1. Compute $\mathbf{l}$ according to Equation 4.18, its closest point $\mathbf{o}$ and direction $\mathbf{d}$ (Recall Section 3.1.2.3).
2. Normalize $\|\mathbf{n}\| = \|\mathbf{d}\| = 1$ and dehomogenize $o_2 = 1$.
3. Compute values t_{min} and t_{max}, such that $\mathbf{x}_{min} = \mathbf{o} + t_{min} \cdot \mathbf{d}$ and $\mathbf{x}_{max} = \mathbf{o} + t_{max} \cdot \mathbf{d}$ are the intersections of the line with the image border with $t_{min} < t_{max}$.
4. Initialize summation variable s.
5. **for** ($t = t_{min}$; $t \leq t_{max}$; $t \leftarrow t + \Delta t$)
   (a) Compute pixel location $(u, v, 1)^\top \cong \mathbf{x} \leftarrow \mathbf{o} + t \cdot \mathbf{d}$.
   (b) Compute $j \leftarrow J_{\mathbf{H}}(u, v)$.
   (c) Compute distance w of 3D location of $\mathbf{x}$ (on the virtual detector) to the source position.
   (d) Increment $s \leftarrow s + f(\mathbf{x}) \cdot j \cdot w \cdot \Delta t$.

- **return** Variable s, which is the Radon transform of projectively distorted image $\mathbf{H}f$ for a line $\mathbf{l}'$.

Algorithm 4.1 computes an integral along a line $\mathbf{l}'$ over an image which has been projectively transformed by a homography $\mathbf{H}$. The algorithm also contains an additional distance weight from each pixel to the source, since Equation 2.67 assumes a normalized X-ray transform. For validation, we present in Figure 4.3, top, the redundant signals extracted from two X-ray shots of a pumpkin shown in Figure 4.6, along with the warped images in Figure 4.4. The fan-beam consistency condition can be computed explicitly as a sum over these rectified images weighted by the distance of each point to the stereo baseline. Integration in the original images,

Figure 4.4: Rectified projection images of a pumpkin phantom in case of a primary angle difference of 120°. The green cube is intended to visualize the distortion introduced by rectification.

while taking into account the Jacobian according to Algorithm 4.1 is identical. The method breaks down for large primary angle difference, once the epipoles lie within the images, compare Figure 4.2, bottom.

4.2 Epipolar Consistency and Radon Intermediate Functions

4.2.1 Radon Intermediate Functions

The following section is rooted in analytic reconstruction theory. The derivation of various reconstruction formulas is well beyond the scope of this work. We point the reader to books such as [Zeng 10, Buzu 08, Natt 86]. While the connection between Grangeat's theorem and epipolar geometry was first established by Aichert et al. [Aich 14, Aich 15a], the following sections rely on the more general and concise presentation by Jérôme Lesaint [Lesa 18b]. We begin by summarizing the results of Clack(doyle) et al. [Clac 94], who first presented a common reconstruction framework using so-called Radon intermediate functions, including that of Smith [Smit 85] and Grangeat [Gran 91], as well as Tuy [Tuy 83]. At the core of these reconstruction techniques is a direct link between the 2D Radon space of projection images and the 3D Radon space of the object. While most of this thesis addresses specifically two projection images, literature considers a CT trajectory under continuous motion of the source, which is parametrized by a single parameter (typically named λ). For our purposes, it suffices to start with the divergent X-ray transform

$$g\left(\mathring{\boldsymbol{\theta}}, \boldsymbol{c}\right) = \int_0^\infty f(\boldsymbol{c} + \mathring{\boldsymbol{\theta}} t)\, \mathrm{d}t, \tag{4.20}$$

where $\boldsymbol{c} \in \mathbb{R}^3$ is the source position and $\mathring{\boldsymbol{\theta}} \in \mathbb{S}^2$ points in the direction of a specific ray. Any point $\boldsymbol{x} \in \mathbb{R}^3$ on such a ray can be denoted $\boldsymbol{x} = \boldsymbol{c} + t\mathring{\boldsymbol{\theta}}$, where t is the distance from the source position $\boldsymbol{c}$. Note that practical use in FDCT of this representation of projections still requires a change of variables to flat-panel detector pixels. The divergent X-ray transform $g\left(\mathring{\boldsymbol{\theta}}, \boldsymbol{c}\right)$ can be obtained from a flat-panel detector image $I(u, v)$ with the same source position by a per-ray division by the cosine of the angle of the respective ray and the detector plane. This means the following results directly apply to cosine-weighted FDCT projection images.

We present two filters that link both 3D Radon space and 2D Radon space of projections. These filters are the derivative (Grangeat) and ramp filter (Smith), both

of which have been used for epipolar consistency [Lesa 16]. The two filters can be written as the derivative of the Dirac impulse δ' and the ramp filter in Fourier domain

$$\delta'(s) = 2\pi i \int \sigma e^{2\pi i \sigma s} \, \mathrm{d}\sigma \tag{4.21}$$

and

$$\rho(s) = \int |\sigma| e^{2\pi i \sigma s} \, \mathrm{d}\sigma. \tag{4.22}$$

We refer to the function $\epsilon_\tau(s)$ simply as the filter and define it as a linear combination of the two

$$\epsilon_\tau(s) = (1-\tau)\delta'(s) + \tau\rho(s). \tag{4.23}$$

We will be most interested in the filter $\epsilon_0 = \delta'$ (Grangeat) but we do note that $\epsilon_1 = \rho$ (Smith) has been used in the contex of consisteny as well [Lesa 16]. Both δ' and ρ are homogeneous functions of degree -2, meaning that

$$\forall \alpha \in \mathbb{R}: \quad \epsilon_\tau(\alpha s) = \frac{1}{\alpha^2}\epsilon_\tau(s). \tag{4.24}$$

The two filters differ in that one is even and the other is odd

$$\delta'(-s) = -\delta'(s) \text{ and } \rho(-s) = \rho(s). \tag{4.25}$$

The following paragraph summarizes Lemma 1 in Clackdoyle et al. [Clac 94] and can also be found in context of epipolar consistency in Ch. I 1.6 Eq. 57 ff. in Lesaint et al. [Lesa 18b]. We begin with the definition of the Radon intermediate function

$$G\left(\mathring{\boldsymbol{\beta}}, \boldsymbol{c}\right) = \int_{\mathbb{S}^2} g\left(\mathring{\boldsymbol{\theta}}, \boldsymbol{c}\right) \epsilon_\tau\left(\mathring{\boldsymbol{\theta}}^\top \mathring{\boldsymbol{\beta}}\right) \, \mathrm{d}\mathring{\boldsymbol{\theta}}. \tag{4.26}$$

Here, $\boldsymbol{c}$ denotes the X-ray source position and the unit vector $\mathring{\boldsymbol{\beta}}$ is interpreted as the normal to a plane through the source position. Then $\mathring{\boldsymbol{\theta}}^\top \mathring{\boldsymbol{\beta}}$ can be interpreted as the cosine of the angle of a projection ray to the plane. The remainder of this section shows that for a fixed $\boldsymbol{c}$, this function is a filtered projection image. Due to the particular importance of the result for this thesis, all steps [Lesa 18b] are reproduced here. First, we consider the ray

$$\mathring{\boldsymbol{\theta}} = \frac{\boldsymbol{x} - \boldsymbol{c}}{\|\boldsymbol{x} - \boldsymbol{c}\|}, \tag{4.27}$$

belonging to a 3D detector position $\boldsymbol{x}$. We can thus perform a polar-to-cartesian change of variables, which introduces a Jacobian of $t^2 = \|\boldsymbol{x} - \boldsymbol{c}\|^{-2}$

$$G\left(\mathring{\boldsymbol{\beta}}, \boldsymbol{c}\right) = \int_{\mathbb{R}^3} \epsilon_\tau\left(\frac{\boldsymbol{x} - \boldsymbol{c}}{\|\boldsymbol{x} - \boldsymbol{c}\|} \cdot \mathring{\boldsymbol{\beta}}\right) \frac{1}{\|\boldsymbol{x} - \boldsymbol{c}\|^2} \, \mathrm{d}\boldsymbol{x}. \tag{4.28}$$

Pulling out a factor of $\frac{1}{t}$ from underneath a homogeneous function of degree -2 produces t^2 which cancels out with the Jacobian

$$G\left(\mathring{\boldsymbol{\beta}}, \boldsymbol{c}\right) = \int_{\mathbb{R}^3} \epsilon_\tau\left(\boldsymbol{x} \cdot \mathring{\boldsymbol{\beta}} - \boldsymbol{c} \cdot \mathring{\boldsymbol{\beta}}\right) f(\boldsymbol{x}) \, \mathrm{d}\boldsymbol{x}. \tag{4.29}$$

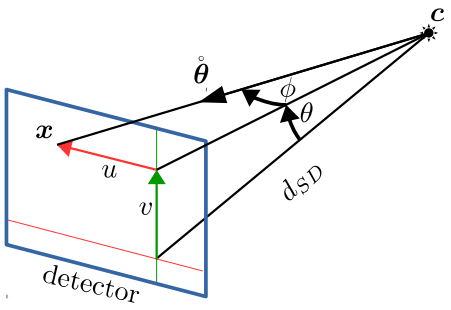

Figure 4.5: Definition of coordinate systems. The principal ray meets the detector at a right angle and defines the u-v coordinate center. The angles ϕ and θ define the ray direction $\mathring{\boldsymbol{\theta}}$.

Next, it is a property of the Dirac function that the integral of a function $f(s)$ multiplied with $\delta(s-x)$ over the whole domain s evaluates the function at x

$$f(x) = \int f(s)\delta(s-x)\ \mathrm{d}s. \tag{4.30}$$

We can write

$$G\left(\mathring{\boldsymbol{\beta}}, \boldsymbol{c}\right) = \int_{\mathbb{R}^3} \int \epsilon_\tau \left(s - \boldsymbol{c}\cdot\mathring{\boldsymbol{\beta}}\right) \delta\left(\boldsymbol{x}\cdot\mathring{\boldsymbol{\beta}} - s\right)\ \mathrm{d}s\, f(\boldsymbol{x})\ \mathrm{d}\boldsymbol{x}. \tag{4.31}$$

Now we can move $f(x)$ into the integral over s and change the order of integration

$$G\left(\mathring{\boldsymbol{\beta}}, \boldsymbol{c}\right) = \int \epsilon_\tau \left(s - \boldsymbol{c}\cdot\mathring{\boldsymbol{\beta}}\right) \left(\int_{\mathbb{R}^3} \delta\left(\boldsymbol{x}\cdot\mathring{\boldsymbol{\beta}} - s\right) f(\boldsymbol{x})\ \mathrm{d}\boldsymbol{x}\right)\ \mathrm{d}s. \tag{4.32}$$

Using the property of the Dirac function from Equation 4.30, one finally obtains filtered versions of the 3D Radon transform over a particular plane

$$G\left(\mathring{\boldsymbol{\beta}}, \boldsymbol{c}\right) = \int \left((1-\tau)\delta' + \tau\rho\right)\left(s - \boldsymbol{c}\cdot\mathring{\boldsymbol{\beta}}\right)\left((\mathcal{R}f)(\mathring{\boldsymbol{\beta}}, s)\right)\ \mathrm{d}s. \tag{4.33}$$

Note that the filter is actually a convolution of $(\mathcal{R})$ in the s-variable with the function $((1-\tau)\delta' + \tau\rho)$, which finally gives us

$$G\left(\mathring{\boldsymbol{\beta}}, \boldsymbol{c}\right) = \tau(\rho * (\mathcal{R}f))(\boldsymbol{c}\cdot\mathring{\boldsymbol{\beta}}) - (1-\tau)(\delta' * (\mathcal{R}f))(\boldsymbol{c}\cdot\mathring{\boldsymbol{\beta}}). \tag{4.34}$$

4.2.2 Grangeat's Theorem

Grangeat [Gran 91] has shown that the Radon intermediate function for $\tau = 0$ can be computed directly from projection images. To show this, we follow the calculations by Lesaint [Lesa 18b] and define a coordinate system (u, v) representing the detector axes with the origin in the principal point (projection of $\boldsymbol{c}$ along w). The origin shall be located in the source position $\boldsymbol{c} = (0,0,0)^\top$ and without loss of generality, the

detector u-axis is parallel to the plane $\bar{\mathbf{e}}^{\kappa}$ defined by the normal $\mathring{\boldsymbol{\beta}}$. A sketch of this coordinate system can be found in Figure 4.5. We change variables from the ϕ-θ sphere to the u-v detector, where d_{SD} is the source detector distance. We begin by parametrizing the ray direction $\mathring{\boldsymbol{\theta}}$ on the sphere with two angles ϕ, θ

$$\mathring{\boldsymbol{\theta}} = (\sin(\phi), \sin(\theta)\cos(\phi), \cos(\theta)\cos(\phi))^{\top}, \tag{4.35}$$

$$d\mathring{\boldsymbol{\theta}} = \cos(\phi)\mathrm{d}\phi\mathrm{d}\theta. \tag{4.36}$$

In this particular spherical coordinate system, the direction $\mathring{\boldsymbol{\beta}}$ simply becomes $(\beta, 0)$. We express the detector pixel coordinates in terms of the ray direction and source-detector distance:

$$v = d_{SD}\tan(\theta), \tag{4.37}$$

$$u = \sqrt{v^2 + d_{SD}^2}\tan(\phi). \tag{4.38}$$

The distance of the pixel $\boldsymbol{x}$ with coordinates u, v to the source $\boldsymbol{c}$ (located in the origin) is now

$$\|\boldsymbol{x} - \boldsymbol{c}\| = \sqrt{u^2 + v^2 + d_{SD}^2}. \tag{4.39}$$

By differentiating Equations 4.37 and 4.38 we have

$$\mathrm{d}\theta\mathrm{d}\phi = \frac{d_{SD}}{\|\boldsymbol{x} - \boldsymbol{c}\|^2\sqrt{v^2 + d_{SD}^2}}\mathrm{d}u\mathrm{d}v. \tag{4.40}$$

Using trigonometry, we can express $\cos(\phi)$ via u and d_{SD}

$$\cos(\phi) = \frac{\sqrt{u^2 + d_{SD}^2}}{\|\boldsymbol{x} - \boldsymbol{c}\|}, \tag{4.41}$$

and we can express the dot-product

$$\mathring{\boldsymbol{\theta}}^{\top}\mathring{\boldsymbol{\beta}} = v\cos(\beta) - d_{SD}\sin(\beta). \tag{4.42}$$

Putting Equations 4.40 and 4.41 into Equation 4.36, we obtain

$$\begin{aligned} d\mathring{\boldsymbol{\theta}} &= \frac{\sqrt{u^2 + d_{SD}^2}}{\|\boldsymbol{x} - \boldsymbol{c}\|} \cdot \frac{d_{SD}}{\|\boldsymbol{x} - \boldsymbol{c}\|^2\sqrt{v^2 + d_{SD}^2}}\mathrm{d}u\mathrm{d}v \\ &= \frac{d_{SD}}{\|\boldsymbol{x} - \boldsymbol{c}\|^3}\mathrm{d}u\mathrm{d}v. \end{aligned}$$

Finally, setting $\tau = 0$ and changing the variables in Equation 4.26 gives

$$\begin{aligned} G\left(\mathring{\boldsymbol{\beta}}, \boldsymbol{c}\right) &= \int_{\mathbb{S}^2} g\left(\mathring{\boldsymbol{\theta}}, \boldsymbol{c}\right) \delta'\left(\mathring{\boldsymbol{\theta}}^{\top}\mathring{\boldsymbol{\beta}}\right)\, \mathrm{d}\mathring{\boldsymbol{\theta}} \\ &= \iint I_{\boldsymbol{c}}(u, v) \cdot \delta'\left(v\cos(\beta) - d_{SD}\sin(\beta)\right) \frac{d_{SD}}{\|\boldsymbol{x} - \boldsymbol{c}\|^3}\, \mathrm{d}u\mathrm{d}v. \end{aligned}$$

Here, $I_{\boldsymbol{c}}$ denotes the cosine-weighted flat-panel detector projection image. The equation $v\cos(\beta) - d_{SD}\sin(\beta) = 0$ actually defines a line on the detector with the only

information contributing to $G_0\left(\mathring{\boldsymbol{\beta}}, \boldsymbol{c}\right)$. To make this more explicit, we can pull out the $\cos(\beta)$ from the Dirac derivative and make the line integral explicit without the Dirac notation

$$\begin{aligned} G\left(\mathring{\boldsymbol{\beta}}, \boldsymbol{c}\right) &= \iint I_{\boldsymbol{c}}(u,v) \cdot \frac{1}{\cos(\beta)^2} \cdot \delta'\left(v - d_{SD}\tan(\beta)\right) \frac{d_{SD}}{\|\boldsymbol{x}-\boldsymbol{c}\|^3}\, \mathrm{d}u\mathrm{d}v \\ &= \frac{1}{\cos(\beta)^2} \frac{\partial}{\partial v} \int I_{\boldsymbol{c}}(u,v)\, \mathrm{d}u \Big|_{v=d_{SD}\tan(\beta)} . \end{aligned} \tag{4.43}$$

This is known as Grangeat's theorem. Its importance lies in the fact that a quantity from the 3D Radon transform can be computed using just a cone-beam projection image. Note that the coordinate system was chosen to prove the theorem for lines with $v = \text{const.}$ without loss of generality, i.e., the general case differs by only a rigid transformation and the theorem holds for any choice of $\mathring{\boldsymbol{\beta}}$. Debbeler et al. [Debb 13] pointed out that Grangeat's theorem actually connects certain plane integrals, i.e., the 3D Radon transform, with line integrals of the projection, i.e., the 2D Radon transform. In Equation 4.43 we can see that the filtering occurs in an orthogonal direction to the line. We can compute all values of $G\left(\mathring{\boldsymbol{\beta}}, \boldsymbol{c}\right)$ in one go by computing the 2D Radon transform of the cosine-weighted projection image (actually a discrete version thereof) and taking the derivative in the second variable

$$\frac{\partial}{\partial t}(\mathcal{R}I)(\alpha, t), \tag{4.44}$$

and multiplying a weight of $\frac{1}{\cos(\beta)^2}$ that depends on the plane normal $\mathring{\boldsymbol{\beta}}$. Here, the Radon intermediate function is parametrized by a line $\mathbf{l} = \text{line}(\alpha, t)$ instead of $\mathring{\boldsymbol{\beta}}$. So far, we have computed the line from the plane normal $\mathring{\boldsymbol{\beta}}$ but the inverse will be discussed in the following section.

4.2.3 Relation to Epipolar Geometry

The intermediate function has been used for reconstruction, however in this work, we are particularly interested in a property of Equation 4.34. The source position $\boldsymbol{c}$ appears only in the dot-product $\boldsymbol{c} \cdot \mathring{\boldsymbol{\beta}}$. As a consequence, we have an identity for shifting the source position inside the plane orthogonal to $\mathring{\boldsymbol{\beta}}$

$$\forall \boldsymbol{t} \in \mathbb{R}^3 \text{ s.t. } \boldsymbol{t} \cdot \mathring{\boldsymbol{\beta}} = 0: \quad G\left(\mathring{\boldsymbol{\beta}}, \boldsymbol{c}\right) = G\left(\mathring{\boldsymbol{\beta}}, \boldsymbol{c} + \boldsymbol{t}\right). \tag{4.45}$$

Note that both sides of the equation have identical weight $\frac{1}{\cos(\beta)^2}$, so it divides out. This is an almost identical expression to the derivative of the LTC condition from Equation 2.68 of Section 4.1.1. The formulation by Grangeat is more powerful because it does not require the source to move in parallel to the detector.

Interestingly, Equation 4.45 holds only for motion vectors $\boldsymbol{t}$ with $\boldsymbol{t} \cdot \mathring{\boldsymbol{\beta}} = 0$. In practice, we have a given set of projections, say two cosine-weighted projections I_0 and I_1 with projection matrices $\mathbf{P}_0$ and $\mathbf{P}_1$ source positions $\boldsymbol{c}_0$ and $\boldsymbol{c}_1$. The choice of a direction $\mathring{\boldsymbol{\beta}}$ is no longer free, since $\boldsymbol{t} = \boldsymbol{c}_1 - \boldsymbol{c}_0$ is the translation between the

Figure 4.6: Pumpkin phantom. Left: Two slices through a CT reconstruction. Center: Photograph. Right: Iso-surface rendering of the air interface.

two X-ray source positions. This takes away one degree of freedom. The direction $\mathring{\boldsymbol{\beta}}$ is now fully defined by a single angle around the translation vector $\boldsymbol{t}$. Recall that the 3D Radon transform is a plane integral over a plane defined by normal vector $\mathring{\boldsymbol{\beta}}$ and signed distance to the origin s. The plane $\bar{\mathbf{e}}^{\kappa} \cong (\mathring{\boldsymbol{\beta}}, -s)^{\top}$ thus contains $\boldsymbol{c}_0$ and due to $\boldsymbol{t} \cdot \mathring{\boldsymbol{\beta}} = 0$ also contains the source position $\boldsymbol{c}_1 = \boldsymbol{c}_0 + \boldsymbol{t}$. Finally, $\boldsymbol{t}$ takes the role of the stereo baseline an the line on the detector as identified in equation 4.26 is an epipolar line, since it is the intersection of $\bar{\mathbf{e}}^{\kappa}$ and the detector. Evidently, the underlying geometry is exactly epipolar geometry. This realization is an important step in expressing and quantifying all redundant information in two X-ray projections based on what we will now call epipolar consistency. For any plane $\bar{\mathbf{e}}^{\kappa} \cong (\mathring{\boldsymbol{\beta}}, -s)^{\top}$ we have

$$\mathfrak{G}_0(\mathbf{l}_0) = \mathfrak{G}_1(\mathbf{l}_1), \tag{4.46}$$

where $\mathbf{l}_0$ and $\mathbf{l}_1$ are epipolar lines with

$$\mathbf{l}_0 = \mathbf{P}_0^{\top} \bar{\mathbf{e}}^{\kappa} \tag{4.47}$$

$$\text{and } \mathbf{l}_1 = \mathbf{P}_1^{\top} \bar{\mathbf{e}}^{\kappa}, \tag{4.48}$$

with

$$\mathfrak{G}_i(\mathbf{l}) \overset{\text{def}}{=} \mathfrak{G}_i(\alpha, t) = \frac{\partial}{\partial t} (\mathcal{R} I_i)(\alpha, t). \tag{4.49}$$

This is the main result of this section. Note that Lesaint et al. [Lesa 16] has shown that the same also works for the case of $\tau = 1$ with the Ramp filter and we have already introduced FBCC, both of which are also types of epipolar consistency. All three are discussed in the coming sections, however practical experiments usually use the derivative, in the following called Grangeat cosistency condition (GCC).

4.3 Implementation of Consistency Metrics

In Sections 4.1 and 4.2 three different conditions on epipolar lines have been presented. The first, called FBCC, is a weighted integral over intensities on epipolar lines. The

second, GCC is an orthogonal derivative of an integral along the lines. The third, was not derived entirely but instead of the derivative $\tau = 0$ uses a ramp filter $\tau = 1$ in the orthogonal direction to the line integrals[Lesa 16]. The underlying geometry is the same. In this section, we define a way to measure inconsistency between two projection images. The metric should be irrespective of the order of views and it should be fast to evaluate.

4.3.1 Epipolar Lines from Projection Matrices and Angle

The conditions we have established hold for each pair of corresponding lines. Since there exists a pencil of epipolar planes, each of which induces a corresponding line pair, this section first addresses the geometric aspect of computing corresponding epipolar lines $\mathbf{l}_0^\kappa$ and $\mathbf{l}_1^\kappa$ from two projections matrices $\mathbf{P}_0$ and $\mathbf{P}_1$ and an epipolar plane angle κ. We will solve this geometric problem using the tools from Chapter 3 and condense the algorithm from the following steps into two small matrix multiplications

1. Parametrize epipolar planes by epipolar plane angle κ.
2. Compute from an epipolar plane $\bar{\mathbf{e}}^\kappa$ the epipolar lines $\mathbf{l}_0^\kappa$ and $\mathbf{l}_1^\kappa$.
3. (only for Radon intermediate GCC and SCC) Compute sample locations in filtered Radon transforms such that $\mathbf{l}_0^\kappa = \text{line}(\alpha_0, t_0)$.

We begin by computing the source positions

$$\bar{\mathbf{c}}_0 = (C_0^0, C_0^1, C_0^2, C_0^3,)^\top \in \text{null}(\mathbf{P}_0), \tag{4.50}$$

and $\bar{\mathbf{c}}_1$ accordingly. The Plücker coordinates of the baseline are then

$$\mathcal{B} \cong (B_{01}, B_{02}, B_{03}, B_{12}, B_{13}, B_{23})^\top, \tag{4.51}$$

where

$$B_{ij} = C_0^i C_1^j - C_1^i C_0^j. \tag{4.52}$$

We can use the insights from Section 3.1.3.3 to construct any epipolar plane in the pencil around the baseline $\mathcal{B}$ from a single angle κ. To do so, we need to single out an arbitrary plane from the bundle as reference (i.e., angle $\kappa = 0°$). We will assume that the origin is somewhere in the object, so that none of the source positions coincides with the origin. This is a safe assumption, since it is common practice to have the coordinate origin located in the iso-center for circular CT trajectories. Using the notation from Section 3.1.3.4, let $\boldsymbol{d}$ denote the line direction

$$\boldsymbol{d} = \begin{pmatrix} -B_{03} \\ -B_{13} \\ -B_{23} \end{pmatrix}, \tag{4.53}$$

and $\boldsymbol{m}$ denote the line moment

$$\boldsymbol{m} = \begin{pmatrix} B_{12} \\ -B_{02} \\ B_{01} \end{pmatrix}. \tag{4.54}$$

For most practical purposes the source positions are finite (i.e., non-parallel projections) and we could compute $\boldsymbol{d}$ and $\boldsymbol{m}$ according to

$$\boldsymbol{d} = \boldsymbol{c}_1 - \boldsymbol{c}_0, \tag{4.55}$$

and

$$\boldsymbol{m} = \boldsymbol{c}_0 \times \boldsymbol{c}_1, \tag{4.56}$$

where $\boldsymbol{c}_0$ and $\boldsymbol{c}_1$ denote the source positions in $\mathbb{R}^3$. Assuming that the the baseline does not contain the world origin

$$d_{\mathcal{B}} = \frac{\|\boldsymbol{m}\|}{\|\boldsymbol{d}\|} \neq 0, \tag{4.57}$$

we can w.l.o.g. select a scale of $\mathcal{B}$ such that $\|\boldsymbol{d}\| = 1$ and use a reference plane which contains the origin

$$\bar{\mathbf{e}}^0 = [\tilde{\mathcal{B}}]_\times \begin{pmatrix} 0 \\ 0 \\ 0 \\ 1 \end{pmatrix} = \begin{pmatrix} \boldsymbol{m} \\ 0 \end{pmatrix}. \tag{4.58}$$

In the unlikely case that that origin is exactly contained in $\mathcal{B}$, one can offset the reference point or the whole trajectory without changing the epipolar geometry. Later in this work we discuss using $d_{\mathcal{B}}$ as a weight, in which case the exact case $d_{\mathcal{B}} = 0$ is simply ignored. If we go back to Figure 3.4, we see that an orthogonal plane is conveniently given by

$$\bar{\mathbf{e}}^{90^\circ} = \begin{pmatrix} \boldsymbol{m} \times \boldsymbol{d} \\ \boldsymbol{m}^\top \boldsymbol{m} \end{pmatrix}. \tag{4.59}$$

4.3.2 From Epipolar Planes to Lines

It is easy to see that any linear combination of $\bar{\mathbf{e}}^0$ and $\bar{\mathbf{e}}^{90^\circ}$ also contains the baseline $\mathcal{B}$. Note that we have fixed the scale of $\bar{\mathbf{e}}^0$ and $\bar{\mathbf{e}}^{90^\circ}$, so we can perform metric operations. This enables us to define a plane by linear combination of the planes

$$\bar{\mathbf{e}}^\kappa = \frac{1}{\|\boldsymbol{m}\|} \left(\cos(\kappa) \bar{\mathbf{e}}^0 + \sin(\kappa) \bar{\mathbf{e}}^{90^\circ} \right). \tag{4.60}$$

If we scale w.l.o.g. $\|\boldsymbol{d}\| = 1$, then $\bar{\mathbf{e}}^\kappa$ is in Hessian normal form. Its normal then forms an angle of exactly κ to the reference plane $\bar{\mathbf{e}}^0$. The whole operation can be written as a single matrix multiplication

$$\bar{\mathbf{e}}^\kappa = \mathbf{K} \begin{pmatrix} \cos(\kappa) \\ \sin(\kappa) \end{pmatrix}, \tag{4.61}$$

with

$$\mathbf{K} = \frac{1}{\|\boldsymbol{m}\|} \begin{pmatrix} \boldsymbol{m} & \boldsymbol{m} \times \boldsymbol{d} \\ 0 & \boldsymbol{m}^\top \boldsymbol{m} \end{pmatrix} \in \mathbb{R}^{4 \times 2}. \tag{4.62}$$

The matrix $\mathbf{K}$ maps unit vectors to epipolar planes. Recall Equation 3.107

$$\bar{\mathbf{e}}^\kappa \cong \mathbf{P}_0^\top \mathbf{l}_0^\kappa \cong \mathbf{P}_1 \mathbf{l}_1^\kappa. \tag{4.63}$$

Using the pseudoinverse-transpose $\mathbf{P}_0^{+\top}$ we obtain

$$\mathbf{l}_0^\kappa = \mathbf{K}_0 \begin{pmatrix} \cos(\kappa) \\ \sin(\kappa) \end{pmatrix}, \tag{4.64}$$

with

$$\mathbf{K}_0 = \mathbf{P}_0^{+\top}\mathbf{K} \in \mathbb{R}^{3\times 2}, \tag{4.65}$$

and accordingly for the other line $\mathbf{K}_1$, where the image size is $n_u \times n_v$ and $\mathbf{l}_0^\kappa$ is assumed to be in Hessian normal form. In Algorithm 4.2 we present a MATLAB implementation of the geometric part of the EC algorithm. A C++/CUDA implementation of the same if available on GitHub[1].

Algorithm 4.2: Geometry for epipolar consistency. Computation of $\mathbf{K}_0 \in \mathbb{R}^{3\times 2}$ according to Equation 4.64, and $\mathbf{K}_1$ accordingly.

```
% Compute a mapping from an angle k to epipolar lines.
% Usage: l0_k=K0*[cos(k); sin(k)];
%        l1_k=K1*[cos(k); sin(k)];
function [K0 K1]=ecc_computeK(P0, P1);
  % Source positions
  C0=null(P0); C1=null(P1);
  % Plücker Coordinates of the baseline
  [B01 B02 B03 B12 B13 B23]=join(C0,C1);
  a2=[B12;-B02;B01];   % Plücker line moment
  a3=[-B03;-B13;-B23]; % Plücker direction of line

  % Normalization
  s2=norm(a2); s3=norm(a3);
  % Mapping from [cos(k) sin(k)]' to epipolar plane
  K=[[ a2/s2 ; 0], [ cross(a3,a2)/(s3*s2); -s2/s3 ] ];
  % Mappings from k to corresponding epipolar lines
  K0=pinv(P0)'*K; K1=pinv(P1)'*K;
end % function
```

4.3.3 Epipolar Lines in Radon Space

If Radon intermediate functions are used, we still need to convert the lines into angle and signed distance. Let us denote the line coordinates of $\mathbf{l}_0^\kappa = (l_{0,0}^\kappa, l_{0,1}^\kappa, l_{0,2}^\kappa)^\top$. Then recall the computation of the sample locations in the Radon transforms from Eq. 3.3 and 3.4

$$\alpha_0^\kappa = \operatorname{atan2}(-l_{0,0}^\kappa, l_{0,1}^\kappa) \text{ and } t_0^\kappa = \frac{-l_{0,2}^\kappa}{\sqrt{\left(l_{0,0}^\kappa\right)^2 + \left(l_{0,1}^\kappa\right)^2}}, \tag{4.66}$$

and $\alpha_1^\kappa, t_1^\kappa$ accordingly.

Two practical notes in this context are firstly, that the periodicity of the Radon transform should be taken into account at this point. Especially for GCC, where the filter is odd, note that we have

$$\frac{\partial}{\partial t}(\mathcal{R}I)(\alpha, t) = -\frac{\partial}{\partial t}(\mathcal{R}I)(\alpha + \pi, -t). \tag{4.67}$$

[1] https://github.com/aaichert/EpipolarConsistency/

Secondly, the coordinate systems of the projection matrices is typically based on an image corner, whereas the Radon transform usually assumes the center of the image as the coordinate origin. This does not affect the angle, but the sample location in t-direction (exemplary for $\mathbf{l}_0^\kappa$) should be

$$t_0^\kappa - \frac{n_u}{2} l_{0,0}^\kappa - \frac{n_v}{2} l_{0,1}^\kappa. \tag{4.68}$$

The sampling process should be done on the GPU, since most computational effort of the EC algorithm is spent sampling epipolar planes. Algorithm 4.3 presents simplified C++/CUDA source code of the sampling process. It assumes the Radon intermediate function has been computed for an odd (Grangeat) or even (Smith) filter and has been stored in a texture.

The samples drawn from Radon space according to Equation 4.66 are not arbitrary. We know that all epipolar lines contain a common point called the epipole. Suppose for the moment that this epipole be a finite point $\mathbf{e}_0 = (e_u, e_v, 1)^\top$. We can then represent all epipolar lines by a direction α_0, written as an infinite point $\mathbf{d}_0 = (\cos(\alpha_0), \sin(\alpha_0), 0)^\top$ joined with the epipole. We have

$$\mathbf{l}_0 = \mathbf{e}_0 \times \mathbf{d}_0 = \begin{pmatrix} -\sin(\alpha_0) \\ \cos(\alpha_0) \\ e_u \sin(\alpha_0) - e_v \cos(\alpha_0) \end{pmatrix}, \tag{4.69}$$

a line in Hessian normal form. We can express the signed distance t_0 as a function of the angle α_0 according to

$$t_0(\alpha_0) = -e_u \sin(\alpha_0) + e_v \cos(\alpha_0). \tag{4.70}$$

This is a sinusoid curve whose amplitude depends on the distance of the epipole from the image center. The epipoles are contained in the image only in case of forward/backward motion or for two projections from opposite directions. In the usual case, however, epipolar lines intersect the image for only a very small range of α_0. For these intersecting lines, we see only a small part of the sinusoidal $t_0(\alpha_0)$ with very high amplitude, so it appears almost like a line in Radon space. For an infinite epipole, the location of epipolar lines in Radon space is obvious: all epipolar lines are parallel and therefore form a straight line $\alpha = const.$ in Radon space. t_0 in this case can no longer be written as a function f α_0.

4.4 Comparison of Epipolar Consistency Conditions

4.4.1 Example Images

This section presents examples for the three presented epipolar consistency metrics, Grangeat (derivative), Smith (ramp) and FBCC (rectified, distance-weighted, compare Figures 4.4 and 4.3). We present the pumpkin phantom, which has already been shown in Figure 4.6. This time, we provide two real X-ray images, which have been pre-processed to line-integral data. The images are shown in Figure 4.7, left and center. In the same figure, right, the relative geometry of the projections is shown.

Algorithm 4.3: Sampling process assuming that the Radon transform is stored as a texture for lines with a distance $t \in \left[-\frac{r_t}{2}, +\frac{r_t}{2}\right]$, where r_t is the range of the distance parameter. Sampling occurs in normalized texture coordinates.

```
/// Compute location to be sampled within Radon intermediate transform.
/// Output: Radon bin coordinates stored in line[0] and line[1].
inline bool lineToSampleDtr(float line[3], float range_t)
{
	// Length of normal vector
	float length=sqrtf(line[0]*line[0]+line[1]*line[1]);
	// Angle between line normal and u-axis (scaled from 0 to +2)
	line[0]=atan2f(line[1],line[0])/Pi;
	if (line[0]<0) line[0]+=2;
	// Distance to the origin (scaled to Radon bins)
	line[1]=-(line[2]/length)/range_t+0.5f;
	// Account for periodicity
	if (line[0]>1)
	{
		line[0]=line[0]-1.f;
		line[1]=1.f-line[1];
		return true;
	}
	return false;
}

/// Compute Epipolar line and convert to (angle, distance).
/// Then sample pre-computed Radon intermediate function
template <bool is_odd>
float getRedundancy(const float *K, Texture tradonIntermediate, float range_t,
		    float cos_k, float sin_k)
{
	// Find corresponding epipolar lines for plane at angle kappa.
	float line[]={
		K[0]*cos_k+K[3]*sin_k,
		K[1]*cos_k+K[4]*sin_k,
		K[2]*cos_k+K[5]*sin_k};

	// Convert line to angle distance and compute texture coordinates to be sampled.
	bool angle_moved_by_pi=lineToSampleDtr(line,range_t);

	// Sample Radon intermediate function.
	// Account for symmetry up to sign in case of Grangeat (odd).
	if (is_odd && angle_moved_by_pi)
		return -tex2D(radonIntermediate, line[0],line[1]);
	return +tex2D(radonIntermediate, line[0],line[1]);
}
```

Figure 4.7: Two exemplar X-ray images of the pumpkin in Figure 4.6. Left: Projection images (top: red, bottom: green). Right: perspective visualization of their source-detector geometries. The black line shows the stereo baseline connecting the source positions. Note how the epipolar is a point on the baseline in 3D, where the detector plane would intersect. The green box is intended to visualize the different rotation. Several epipolar lines are indicated in all sub-figures (in sequence red, turquoise, magenta, blue, yellow, each going back to an epipolar line) and one epipolar plane (magenta) is shaded.

The red source-detector geometry corresponds to the left projection image, the green, respectively, to the right projection image. The stereo baseline (black) connects the two source positions and is contained in all epipolar planes. Several exemplar planes are visualized by their intersections with the two detector planes as red, turquoise, magenta, blue and yellow lines. These lines are epipolar lines visualized in 3D. The same lines can also be seen in the left and right images as 2D lines in the domain of the projection images.

The presented data shows several common imperfections. The pumpkin is resting on a table. Although it is barely visible in the projection images, it is truncated in both directions and therefore contributes some inconsistent image content. In the left/red image, a hint of the edge of that table is visible in the top-right corner of the projection image. Besides, due to imperfect pre-processing, the projection images are affected by the so-called heel-effect. This effect goes back to the shape of the X-ray anode [Buzu 08] and leads, in this case, to a slightly stronger illumination of the top of the projection images compared to the bottom. The projection geometry is computed, in this case, by acquisition of a calibration phantom in the same scanner positions. While the computation of the projection geometry using such a phantom is sub-pixel accurate if done correctly, the scanner may well be unable to repeat the exact same geometries. These projection are taken in an arbitrary position using a fluoroscopy setting, which disables some of the usual pre-processing done by the vendor, for example, when reconstructing 3D images. The example presents two reasonable arbitrary projection images to demonstrate that the methods described in this chapter are not restricted to any special trajectory and that they are robust even under these conditions.

4.4.2 Computational Complexity

The evaluation of the epipolar consistency conditions based on Radon intermediate functions (cf. Section 4.2) and weighted integration in the projection images (FBCC, compare 4.1.2) are very similar DCCs. All three cases rely on epipolar geometry and use similar data. Their computational complexity, however, is quite different. FBCC relies on a weighted integration in projection images, which depends on the Source-Detector geometry. Rectification depends mostly on orientation, while an additional distance weight measures distance from each image pixel to the source position. As a result, the per-pixel weights within each image within a pair are never the same. Grangeat (GCC) and Smith (SCC) consistency conditions rely on a filtered Radon transform of the projection images that can be re-used irrespective of which images are being compared. This is an important advantage, since the evaluation of the consistency metric among a set of n images is much more efficient for Radon intermediate functions. The DCC is verified for any pair of images is merely by sampling of these pre-computed line integrals. For FBCC, on the other hand, such a pre-computation is not possible and integrals over projection data has to be computed for each epipolar line and each of the $\frac{n(n-1)}{2}$ pairs anew. Generally, the more images are involved and the more often the DCC should be evaluated, the slower FBCC will be in comparison to GCC and SCC.

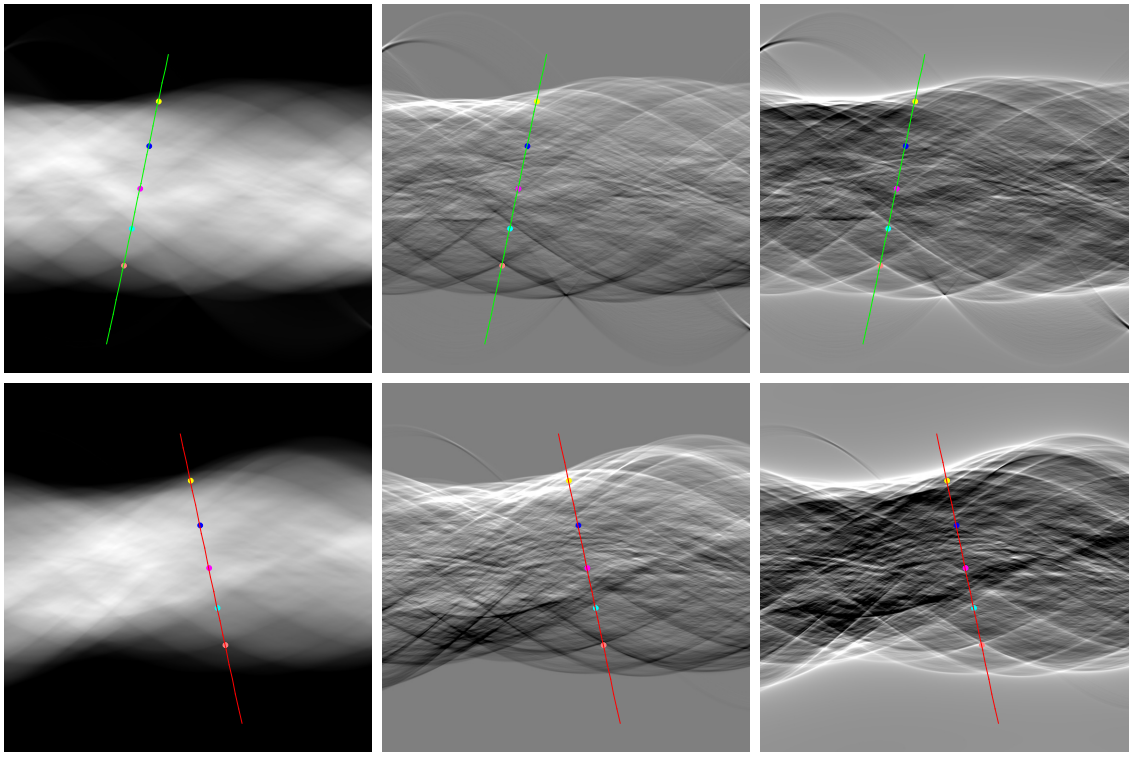

Figure 4.8: Radon intermediate functions. Top row: Left image (red) from Figure 4.7. Bottom row: Right image (green) from Figure 4.7. From left to right: Radon transform of the projection images (without any filter); Derivative in t-direction (vertical direction in figure) of Radon transform and Ramp filter in t-direction of Radon transform. The red/green lines represent the samples drawn to produce Figures 4.9, where the colored dots (in sequence red, turquoise, magenta, blue, yellow) each go back to a specific epipolar plane. The corresponding epipolar lines are shown on the projection images in Figure 4.7.

4.4.3 Comparing Redundant Signals

The samples that are drawn from Radon intermediate functions are sinusoidal, see Figure 4.8. The reason for their sinusoidal shape is that all epipolar lines contain the epipole, cf. Section 4.3.3. We present the plain, unfiltered Radon transform on the left, its derivative in t-direction (vertical) in the center and after application of the ramp filter on the right. Note that the Radon transform, by itself, as shown on the left, does not contain redundant values. Sampling along the same sinusoidal curves does not produce the fan-beam consistency conditions. We present the samples through all three cases in addition to the true FBCC in Figure 4.9. These curves are plots of the intensities sampled along the sinusoidal curves in Figure 4.9, except for the top-right plot, which is the actual FBCC. Note that the graph in Figure 4.8, top, goes back to the unfiltered Radon transform shown in Figure 4.8, left and is not a DCC at all - unweighted line integrals in the detector do not constitute a consistency condition. We find the difference between unfiltered line integrals and true FBCC to be smaller than the inconsistency introduced by acquisition inaccuracies for the presented data set

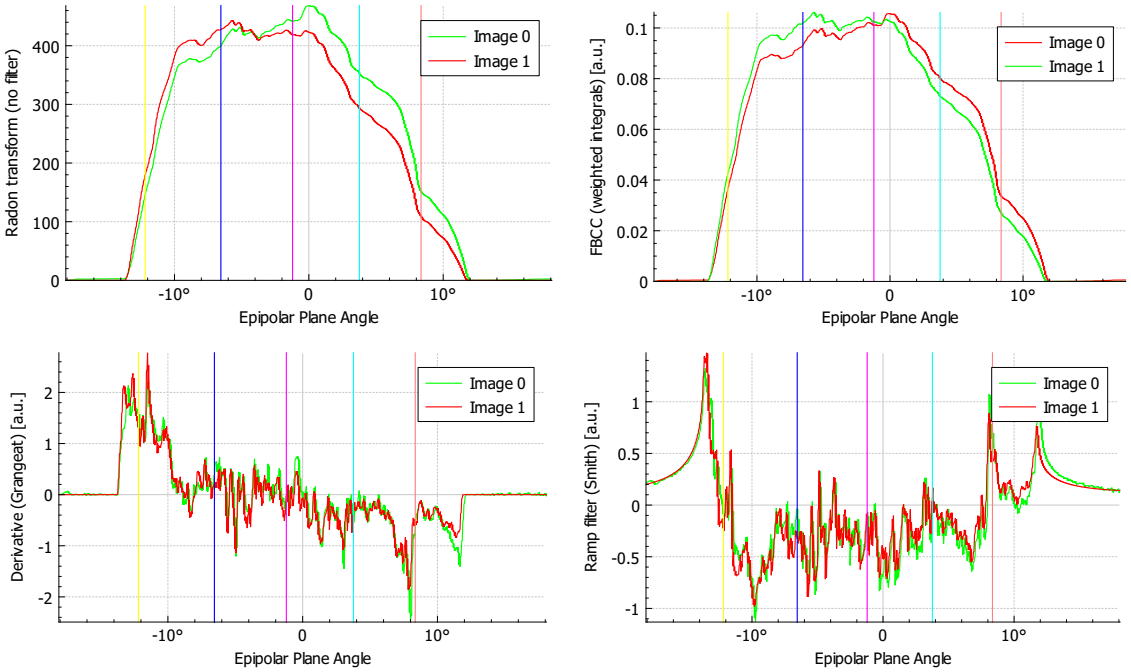

Figure 4.9: Example plots for real data. Top left: integrals on the detector without any weighting (this is not an accurate consistency condition). Top right: FBCC, bottom left GCC, bottom right SCC. Due to automatic exposure control the intensities in the projection images vary slightly. It seems the inconsistency introduced by this effect, as well as some truncation of the table on which the pumpkin has been resting is most evident in FBCC, while GCC and SCC follow the higher-frequency components.

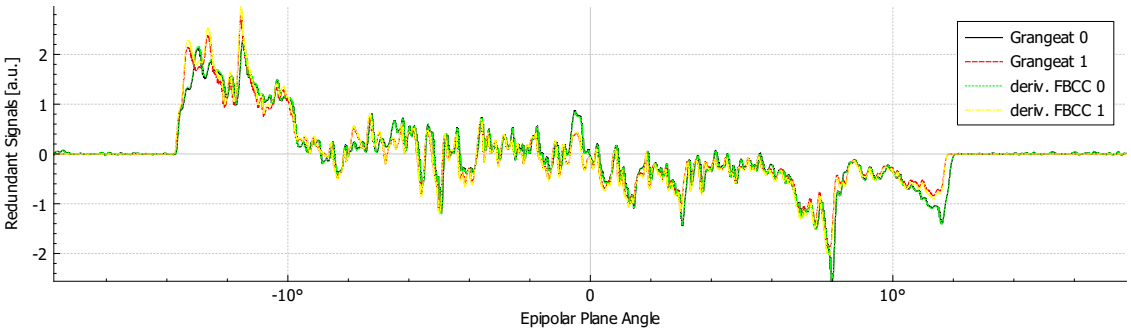

Figure 4.10: Comparison of a derivative of FBCC and Grangeat consistency. The scale has been adjusted so that maxium absolute value matches between the curves.

4.4.4 Relationship between FBCC and GCC

We present a comparison of Grangeat DCC and the derivative in κ-direction of the FBCC in Figure 4.10, which was computed via forward difference method. We observe that the curves for GCC and FBCC overlap almost perfectly for both image 0 and image 1. Thier equality has recently been shown in Lesaint et al. [Lesa 18a]. In the following applications, GCC will be preferred for two reasons. GCC is computationally much cheaper to evaluate then FBCC and in addition, many algorithms which align signals geometrically (i.e., registration) use the derivative for emphasizing high-frequency features. Variations in absolute intensity make similarity metrics like the sum of squares unreliable. In the presented data, such variation occurs due to varying exposure and/or incorrect pre-processing. Additionlly, missing mass due to extinction or truncation may be problematic. When the derivatives of the redundant signals are considered, alignment will focus more on image edges. This is desirable because localization of edges is more reliable, leading to higher accuracy. The derivative also removes constant offsets, which may explain away much of the missing mass.

CHAPTER 5

Calibration and Motion in Computed Tomography

MOTION ESTIMATION using epipolar consistency is the main application investigated in this work. We focus on the efficient implementation of EC [Aich 16] to allow for motion estimation, even in large CT data sets. Depending on the application at hand, the transformations apply globally to all projections (2D detector alignment for turn-table based computed tomography [Maas 14], 3D rigid motion in FDCT short scans [Frys 15]), to individual projections (3D motion compensation in CT or tomosynthesis [Grul 15], 1D heart and respiratory signal extraction from rotational angiography [Unbe 17a]) or to groups of projections relative to one-another (raw-data domain 3D-3D registration (a contribution of this thesis in Section 5.3), 2D and 3D tracking in fluoroscopy [Aich 15b]). We also developed a technique to apply consistency conditions in case of truncated angiography applications, by segmenting the vessels and computing a virtual subtraction angiography of the heart [Unbe 16c]. EC was also used to extract respiratory information in mouse scans [Luo 18]. Other applications include beam hardening [Wurf 17, Wurf 18, Abdu 18] and scatter correction [Hoff 18]. This chapter first presents a framework for motion compensation and calibration correction. Generally speaking, the following three ingredients constitute a motion compensation algorithm

- a motion model which transforms the object based on parameters,
- a cost function which measures the quality of an alignment,
- and an optimization algorithm to find parameters that minimize the cost.

We have suggested a new cost function based on epipolar consistency and use simple linear motion models and simple optimization algorithms, namely grid-search or a Simplex variant [John 14], and focus on the behavior of the cost function. Recently, the cost function has also been optimized with better, gradient-based optimizers[Preu 19], although this is not yet reflected in the experiments in this thesis. Assuming the correct alignment is known, either because the data was simulated

(ground truth) or because a reference solution was obtained by another method, we have some intuitive expectations for a "good cost function". Most importantly, the cost function should have a "good" local minimum, meaning that it should be smooth and "locally convex" in some meaningful region. In other words, starting from a reasonable initial guess, the optimization should be able always to find the same minimum and the minimum should represent a set of parameters close to the correct alignment.

5.1 Tracking in Fluoroscopy

5.1.1 General Problem Formulation

The following applications involve many more than two projections, so the pairwise consistency metric we introduced in the last chapter needs to be computed for all pairs. An acquisition of n projections can form $\frac{n(n-1)}{2}$ unordered pairs $\{i,j\} \in \{0,\dots,n-1\}^2$ of two distinct projections. In this chapter, we will use epipolar consistency based on Grangeat's theorem, unless otherwise stated. For a line $\mathbf{l} = \text{line}(\alpha, t)$ and some projection image I_i the Radon intermediate function for Grangeat consistency is $\mathfrak{G}_i(\mathbf{l}) \overset{\text{def}}{=} \mathfrak{G}_i(\alpha,t) = \frac{\partial}{\partial t}(\mathcal{R}I_i)(\alpha,t)$. We then define the metric of epipolar consistency using the squared difference over all epipolar plane angles κ as

$$\text{EC}(\mathbf{P}_0,\mathbf{P}_1,I_0,I_1) = \int_{-\pi}^{+\pi} \left(\mathfrak{G}_0(\mathbf{l}_0^\kappa) - \mathfrak{G}_1(\mathbf{l}_1^\kappa)\right)^2 \,\mathrm{d}\kappa, \tag{5.1}$$

where $\mathbf{l}_0^\kappa$ and $\mathbf{l}_1^\kappa$ are corresponding epipolar lines for a plane angle κ, as defined in Section 4.3.2. In the following, we will investigate motion of the object and/or the detector in particular. In this work, we restrict ourselves to the estimation of rigid motion and affine transformation. These transformations can all be modeled as a matrix multiplication to the projection matrix with some parametrization $\boldsymbol{\varphi}_i$

$$\mathbf{P}_i^{\boldsymbol{\varphi}} = \mathbf{H}_i^{\boldsymbol{\varphi}} \mathbf{P}_i \mathbf{T}_i^{\boldsymbol{\varphi}}, \tag{5.2}$$

where $\mathbf{H}_i^{\boldsymbol{\varphi}} \in \mathbb{R}^{3\times3}$ is some linear transformation of the 2D image and $\mathbf{T}_i^{\boldsymbol{\varphi}} \in \mathbb{R}^{4\times4}$ is some linear transformation of the 3D object. The index i refers to a certain projection index. The applications presented all have different parametrizations $\boldsymbol{\varphi}_i$ and these will be described in context in the following sections. This approach has the advantage that the image data (and their Radon intermediate functions) need not be changed, since the cost function depends only on the projection geometry. Repeated computation of the cost function can be achieved with milliseconds, when implemented on the GPU, allowing for non-linear optimization of a cost function for the consistency over all pairs. The cost function has an inherent symmetry

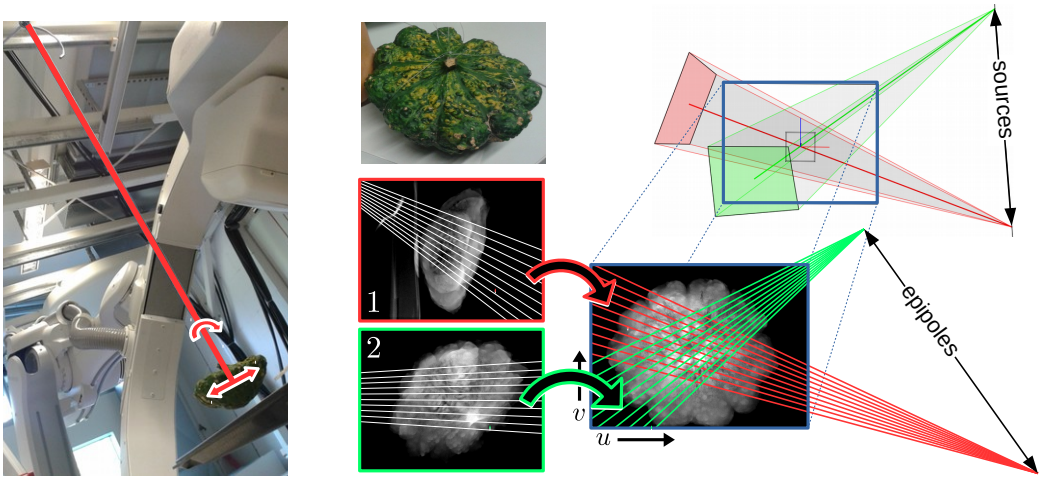

Figure 5.1: A simple fluoroscopy tracking study involving two reference projections (red, green) and detector motion in an input projection image (dark blue). On the top right one may observe the source-detector geometries from the point of view of the input projection. Note how the direction of the epipolar lines depends mostly on the location of the source position. On the left you can see how the pumpkin was suspended from the ceiling to simulate different amounts of swaying and (in a different experiment) rotations.

$\forall \mathbf{P}_i, \mathbf{P}_j : \ \mathrm{EC}(\mathbf{P}_i, \mathbf{P}_j, I_i, I_j) = \mathrm{EC}(\mathbf{P}_j, \mathbf{P}_i, I_j, I_i)$. For a set of n projections, we have the optimization problem

$$\boldsymbol{\varphi}^\star = \frac{1}{2}\underset{\boldsymbol{\varphi}}{\operatorname{argmin}} \sum_{i \neq j}^{n} \mathrm{EC}(\mathbf{P}_i^{\boldsymbol{\varphi}}, \mathbf{P}_j^{\boldsymbol{\varphi}}, I_i, I_j) \tag{5.3}$$

$$= \underset{\boldsymbol{\varphi}}{\operatorname{argmin}} \sum_{i=0}^{n-1} \sum_{j=i+1}^{n} \mathrm{EC}(\mathbf{P}_i^{\boldsymbol{\varphi}}, \mathbf{P}_j^{\boldsymbol{\varphi}}, I_i, I_j). \tag{5.4}$$

Note that in some applications, certain pairs of projections never change their relative 3D geometry i.e. they always move together or do not move at all. These pairs would then be constant in the optimization and should not be computed. This is why we will present slightly different definitions of the cost function - for each application, the constant terms are removed from the sum.

5.1.2 Parametrization

The following section addresses tracking in fluoroscopy using epipolar consistency. Image guidance in interventional radiology typically relies on both preoperative CT and real-time fluoroscopic images. The alignment of the current patient position and the CT can be established using 2D-3D registration [Mark 12]. However, as a fluoroscopy sequence is taken during surgery, both respiration and heartbeat, as well as other patient movements, deteriorate overlays. The question raised by our work in consistency conditions is whether, instead of a computationally expensive registration, a consistency-based optimization may help track patient movements.

This section investigates epipolar consistency for motion tracking, compared to the performance of full 2D-3D registration approaches, as presented by Aichert et al. [Aich 15b]. The goal is rather ambitious: unlike in 2D-3D registration, there is not nearly enough data to reconstruct a 3D representation of the object. In that sense, the goal is to tack an *unknown* object, merely by the assumption that it is the same object we see in a few projections.

We investigate a simplistic model of this scenario by suspending the pumpkin phantom from the ceiling and tracking its motion, cf. Figure 5.1, left. We begin our study of motion compensation by plotting the EC cost function over motion observed in a single projection with respect to a set of n reference projections $\mathcal{R} = \{1, \dots, n\}$. Suppose that $n = 2$ reference X-ray shots are acquired of the pumpkin phantom, cf. Figure 5.1 red and green image frames. The C-arm is then moved to a third position, see Figure 5.1 the dark blue image frame in the top right wireframe visualization. In this position, a fluoroscopy sequence is acquired while the pumpkin is swaying slightly. We first consider a simplistic motion model of 2D detector shifts $\boldsymbol{\varphi} = \{t_u, t_v\}$ of a single detector by left-multiplication of the input projection matrix $\mathbf{P}_0$ with a 2D homography $\mathbf{H}^{\boldsymbol{\varphi}}$

$$\mathbf{P}_0^{\boldsymbol{\varphi}} = \mathbf{H}^{\boldsymbol{\varphi}} \mathbf{P}_0, \tag{5.5}$$

with

$$\mathbf{H}^{\boldsymbol{\varphi}} \cong \begin{pmatrix} 1 & & t_u \\ & 1 & t_v \\ & & 1 \end{pmatrix} \in \mathbb{R}^{3\times 3}. \tag{5.6}$$

We consider the cost function F_{2D} which should be minimal for optimal consistency

$$F_{2D}(\boldsymbol{\varphi}) = \sum_{j=1}^{n} \mathrm{EC}(\mathbf{H}^{\boldsymbol{\varphi}} \mathbf{P}_0, \mathbf{P}_j, I_0, I_j). \tag{5.7}$$

Note that only one projection matrix changes. For $n = 2$ we have

$$F_{2D}(t_u, t_v) = \mathrm{EC}(\mathbf{P}_0^{\boldsymbol{\varphi}}, \mathbf{P}_1, I_0, I_1) + \mathrm{EC}(\mathbf{P}_0^{\boldsymbol{\varphi}}, \mathbf{P}_2, I_0, I_2). \tag{5.8}$$

5.1.3 Cost Function and Observable Motion

In Figure 5.2 we present the plot of F_2 by its summands. All plots are shown in a range of ± 50 px for t_u and t_v, while the ground truth (i.e. correct) position is shown in the center of the plot. The projection images are 2480×1920 pixels in size with a spacing of $0.154 \frac{\mathrm{mm}}{\mathrm{px}}$. On the left, $\mathrm{EC}(\mathbf{P}_0^{\boldsymbol{\varphi}}, \mathbf{P}_1, I_0, I_1)$ represents consistency with the red image in Figure 5.1, while on the right, $\mathrm{EC}(\mathbf{P}_0^{\boldsymbol{\varphi}}, \mathbf{P}_2, I_0, I_2)$ represents consistency with the green image separately. The sum of these two plots is the plot of the final cost function F_2 shown in the center. While the red/left and green/right plots both exhibit an elongated valley, their sum has a much more clearly defined minimum. The location of that minimum is in fact located in the center of the plot where the correct alignment can be found. This means that any 2D misalignment of up to least 50 px can be recovered by this method.

The figure visualizes an important issue with epipolar consistency. The location of the epipoles determines the direction of epipolar lines. Recall the consideration in

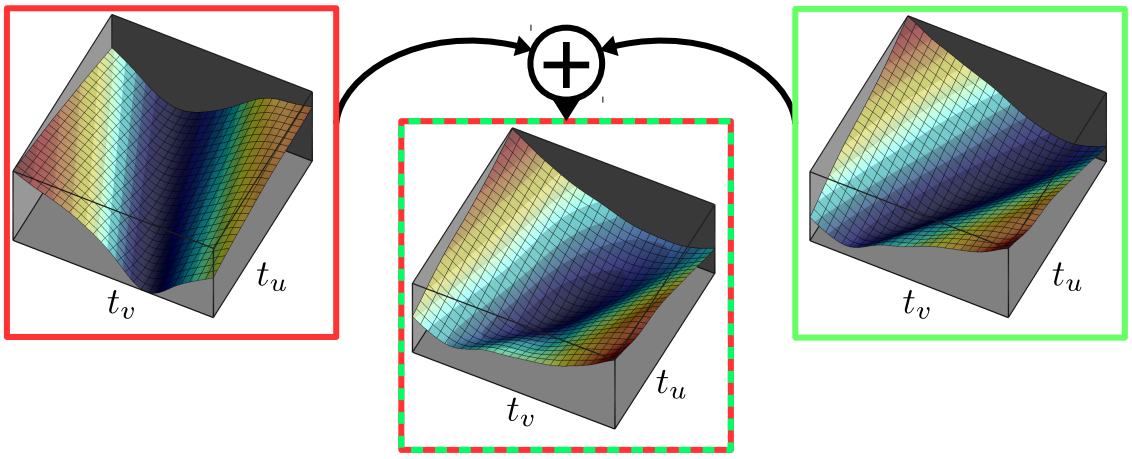

Figure 5.2: Plots of $\mathrm{EC}(\mathbf{P}_0^{\boldsymbol{\varphi}}, \mathbf{P}_1, I_0, I_1)$ (left) and $\mathrm{EC}(\mathbf{P}_0^{\boldsymbol{\varphi}}, \mathbf{P}_2, I_0, I_2)$ (right) in arbitrary units over detector shifts $t_u, t_v \in [-50\text{ px}, +50\text{ px}]$. The plot over their sum F_2 is shown in the center.

Chapter 3: The epipole is the projection of the other source position to the detector, cf. Figure 5.1. The epipole is therefore contained in the image exactly if the other source position "can be seen". This occurs e.g, when (a) when the two projection images are related through a "forward-/backward translation" (i.e. toward or away from the detector) or, when (b) a rotation of about 180° has occurred. Rotations of about 180° between projections. The latter case is typical for computed tomography: A small portion for near-opposite views exhibit epipoles within the detector. However, epipoles are far outside the image for the much more frequent case where the angle between two projections is between 10° and 150°. In the latter case epipolar lines are "almost parallel" to the plane of rotation.

EC is based on line integrals in direction of epipolar lines. Such an integral, however, is invariant to translations in the direction of the line, meaning that when the image is shifted in direction of the line, this integral does not change. The change of the integral is expected to be fastest, when the shift occurs in the orthogonal direction. This is the reason for the valley shape in Figure 5.2, red/left and green/right. Comparing the direction of the two sets of epipolar lines shown in red and green, respectively, in the projection image I_0 in Figure 5.1 (dark blue), they correspond to the directions of the valleys seen in Figure 5.2. Evidently, the center of the plot shows the only minimum within the plotted range. It is therefore possible to reliably recover the correct alignment when a translation parallel to the detector occurs within this range.

5.1.4 Random Study and Tracking

In the following, we generalize the problem

$$\boldsymbol{\varphi}^\star = \operatorname*{argmin}_{\boldsymbol{\varphi}} F_{3D}(\boldsymbol{\varphi}) = \operatorname*{argmin}_{\boldsymbol{\varphi}} \sum_{j=1}^{n} \mathrm{EC}(\mathbf{P}_0 \mathbf{T}^{\boldsymbol{\varphi}}, \mathbf{P}_j, I_0, I_j). \tag{5.9}$$

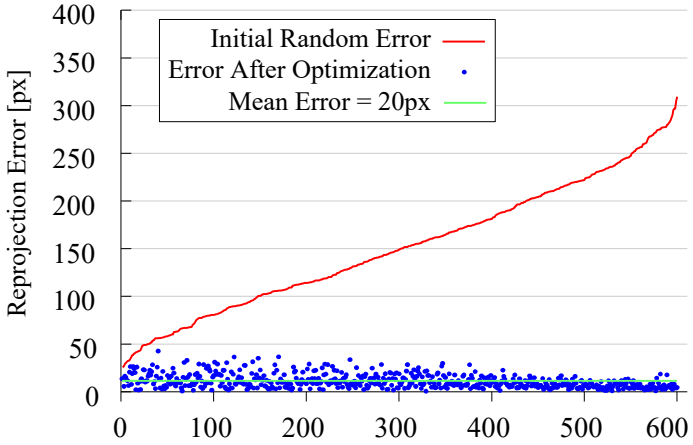

Figure 5.3: Random study of 10 samples per 60 frames of the first sequence over random disturbances of 10° and 25 mm using three reference images.

with a rigid body motion with 6 degrees of freedom

$$\mathbf{T}^{\boldsymbol{\varphi}} \cong \begin{bmatrix} \mathbf{R}_{\boldsymbol{\varphi}} & \boldsymbol{t}_{\boldsymbol{\varphi}} \\ \mathbf{0}^\top & 1 \end{bmatrix} \in \mathbb{R}^{4\times4}, \tag{5.10}$$

defined by the 6D parameter vector

$$\boldsymbol{\varphi} = (r_X,\, r_Y,\, r_Z,\, t_X,\, t_Y,\, t_Z)^\top, \tag{5.11}$$

where r_X, r_Y, and r_Z are three Euler angles defining a rotation matrix $\mathbf{R}_{\boldsymbol{\varphi}}$ and a translation vector $\boldsymbol{t}_{\boldsymbol{\varphi}} = (t_X,\, t_Y,\, t_Z)^\top$. The rigid transformation of the object $\mathbf{T}^{\boldsymbol{\varphi}}$ is a homography in projective three-space which can be right-multiplied to the respective projection matrix $\mathbf{P}_0^{\boldsymbol{\varphi}} = \mathbf{P}_0\mathbf{T}^{\boldsymbol{\varphi}}$. The idea is that a rigid movement of the swinging pumpkin can be recovered by optimization of epipolar consistency, without knowing what the pumpkin looks like in 3D. Please note that the parametrization is intended for relatively small transformations between consecutive frames. Therefore, the typical issues related to Euler angles, namely ambiguity and gimbal lock are avoided.

Plotting the cost function is not straight-forward in 6D space. To investigate the stability of this method, we thus employ a random study. The study is designed to repeatedly and randomly introduce a misalignment to the projection matrix $\mathbf{P}_0^{\tilde{\boldsymbol{\varphi}}} = \mathbf{H}^{\tilde{\boldsymbol{\varphi}}}\mathbf{P}_0$ and then try to recover the ground truth. It can be easily seen that the parameters we seek to recover represent the inverse transformation

$$\mathbf{P}_0^\star = \mathbf{P}_0^{\tilde{\boldsymbol{\varphi}}}\mathbf{T}^{\boldsymbol{\varphi}\star} \approx \mathbf{P}_0^{\tilde{\boldsymbol{\varphi}}}\left(\mathbf{T}^{\tilde{\boldsymbol{\varphi}}}\right)^{-1} = \mathbf{P}_0, \tag{5.12}$$

The approximate sign illustrates the fact that the study compares the numerically achieved result $\boldsymbol{\varphi}^\star$ with the ideal inverse of $\tilde{\boldsymbol{\varphi}}$. In practice, a non-linear local optimization strategy is used, the result of which strongly depends on the starting guess. The study estimates within which maximum parameter range the optimization succeeds in finding the correct minimum. Success is determined by an application-dependent outlier threshold. We call this parameter range the capture range of the method. A random studycan also measure the precision and accuracy by considering the mean

error and standard deviation for the inlier cases. We use 60 projection images taken with significant translation but only small rotation (roughly ±50 mm and ±3° maximum over the whole sequence) and we use the same two reference images, shown in Figure 5.1. We employ a state-of-the-art 2D-3D registration method as reference [Wang 14]. The reference implementation required several hours to align the CT with all images, but with visually very good results. We draw 600 random initial offsets $\tilde{\boldsymbol{\varphi}}$ from a uniform distribution of ±25 mm and ±1° and run a variant of Simplex for non-linear minimization of F. We report errors in pixels by projecting the bounding box corners of the reconstruction volume of the pumpkin by both estimate $\mathbf{P}_0^\star$ and 2D-3D registration reference $\mathbf{P}_0$. This gives an upper bound on the pixel errors expected inside the pumpkin. Figure 5.3 shows the result of the study, sorted by the initial error (obtained by projecting the bounding box corners based on initial estimate $\tilde{\boldsymbol{\varphi}}$). The correct pose can be recovered up to a mean pixel error of 20 px (3.1 mm on the detector) on the outside of the volume. Interestingly, the precision of the method was better for larger initial misalignment. This is likely an artifact of some heuristics in the optimization strategy. Closer investigation showed that the algorithm [Rowa 90], for small errors in rotation, appears to focus on translation parameters first and then fails to recover accurate rotation due to early stopping.

Finally, we applied the optimization algorithm successively to each frame, starting with correct alignment as an initial guess for the first image. We used four reference views to successfully track the pumpkin up to an agreement with the registration-based method of 1.7° and a re-projection error of 18.9 px or 2.9 mm on the detector. It was demonstrated, that even large rotations can be recovered, when more reference views are available [Aich 15b]. Computation time is below one second per optimization, including processing.

5.1.5 Summary

We have presented a consistency-based algorithm which can recover 2D and 3D transformations of an unknown object with a set of reference X-ray projections. However, for practical applications several obstacles exist. First and foremost, the additional effort of acquiring reference views may not be acceptable in many clinical applications. We have not found a case where the data were available as is. Second, the presented study is not entirely realistic when it comes to the truncation assumption. Epipolar consistency assumes that the object is fully visible on the detector. However, due to the harmful nature of X-ray radiation, typically only a small part of a patient is imaged in a clinical task. Additionally, tools or contrast agent would be present, which dominates the images. Since these also move and probably in a different manner than the patient, it is expected that EC would not be able to differentiate between the two moving objects. Unless some method is found to alleviate the problem, clinical application is unrealistic and we are not aware of a practical scenario in industry or material testing. Later, in Section 5.3, we will present a related algorithm which considers a global translation between two sets of images.

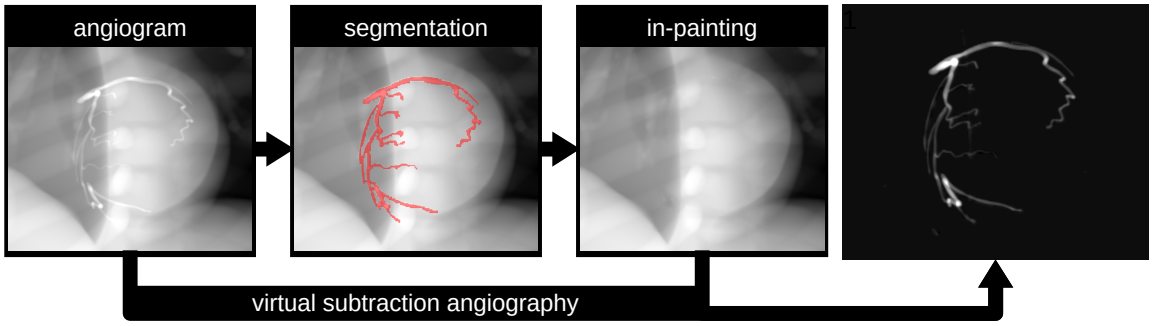

Figure 5.4: vDSA pipeline. An X-ray projection showing contrasted vessels serves as input to a segmentation algorithm. The resulting segmentation mask of the vessels is used to remove contrasted pixels from the original image by in-painting. The resulting image does not contain vessels and can serve as a virtual mask image for subtraction angiography.

5.2 Angiography

5.2.1 Rotational Angiography and Truncation

This chapter addresses rotational angiography of the heart. In this modality, a contrast agent is injected into the blood stream of a patient to visualize blood vessels while a scanner rotates about the patient acquiring a series of images. In this way, a beating heart with all its vessels can be visualized, which would otherwise be almost invisible due to the low tissue contrast typical X-ray modalities exhibit. In this section, we assume a typical FDCT short scan trajectory with 133 projections. The scanner rotates by 210° in approximately 7 seconds, recording several heat beats. Since shortness of breath is a typical symptom for many heart conditions, many patients may be unable to hold their breaths [Blon 06]. The result is a highly inconsistent CT acquisition affected by both respiratory and cardiac motion. The motion models we use are linear and our optimization algorithms have in the past shown problems with periodic inconsistencies. Besides, a 3D non-linear deformation cannot be corrected for by a mere deformation of a projection image. Instead, the dominant cranio-caudal translation will be considered.

5.2.2 Virtual Subtraction Angiography

Motion, however, is not the only source of inconsistency. X-rays are, after all, harmful radiation, so collimators are used to limit the image to a region of interest around the heart. Large parts of the thorax are truncated leading to major inconsistencies. The two dominant sources of inconsistency, motion and truncation cannot be separated by considering DCC alone. This section briefly presents a method to remove truncated structures from the image enabling the estimation of motion via consistency conditions. The contrasted vessels are relevant to the clinician and are contained within the region of interest in their entirety. Vessel segmentation is a typical task in angiography and a variety of approaches exist. We assume pre-processing [Toma 98] and

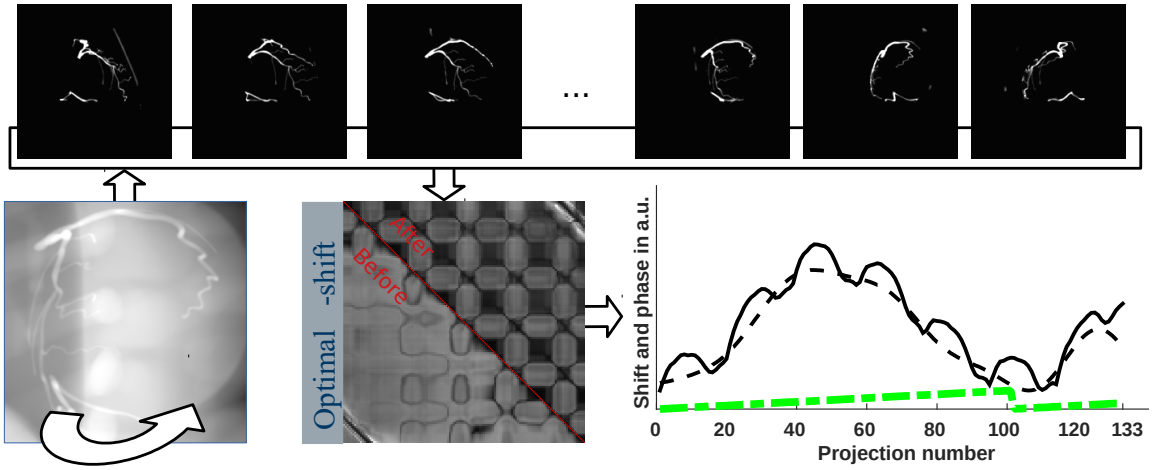

Figure 5.5: Images from a simulated rotational angiography sequence after virtual subtraction.

segmentation of the heart vessels [Unbe 16a] has been performed based on structure and tubular shape of vessels [Fran 98].

Virtual subtraction angiography (vDSA, cf. Figure 5.4) is a new in-painting based pre-processing technique which enables the application of consistency conditions in situations, where the projection images are truncated, but the structures of interest are not [Unbe 16c]. By segmentation, all structures of interest may be removed from an image and replaced by in-painting with content from the remaining image. In-painting is the task of filling holes with sensible image content based on the context and neighborhood [Aach 01]. Such an in-painted image is an estimate to what the image would look like if the structures of interest were not present. It can then be subtracted from the original, to obtain an estimate of the absorption limited to structures of interest. These subtracted images are themselves projection images and they are no longer truncated, so data consistency conditions can be applied.

5.2.3 Motion Extraction and Automatic Gating

We present a numerical simulation of an XCAT like phantom [Rohk 10, Maie 12] with $n = 133$ (unless otherwise stated) projections showing both breathing and heart motion, cf. Figure 5.5 bottom left. Background subtraction is performed using vDSA to get contrast-only sequence, cf. Figure 5.5 top row. A simplistic model of detector v-shift represents translational movement in cranio-caudal direction of each view. It can be written as right-multiplication of all projection matrices for all $i < n$

$$\mathbf{P}_i^{\varphi} = \mathbf{H}_i^{\varphi}\mathbf{P}_i, \tag{5.13}$$

with

$$\mathbf{H}_i^{\varphi} \cong \begin{pmatrix} 1 & & 0 \\ & 1 & t_v \\ & & 1 \end{pmatrix} \in \mathbb{R}^{3\times 3}. \tag{5.14}$$

The optimization problem for EC cost function becomes

$$\boldsymbol{\varphi}^\star = \underset{\boldsymbol{\varphi}}{\operatorname{argmin}} \sum_{j=0}^{n} \sum_{j=i}^{n} d_{\mathcal{B}} \cdot \mathrm{EC}(\mathbf{H}_i^{\boldsymbol{\varphi}} \mathbf{P}_i, \mathbf{H}_j^{\boldsymbol{\varphi}} \mathbf{P}_j, I_i, I_j). \tag{5.15}$$

The heuristic weighting with the baseline distance $d_{\mathcal{B}}$ is due to a higher sensitivity of the cost function EC for opposing views rather than neighboring views. Note that all projection matrices change, and therefore consistency has to be computed for all $N = 8778$ pairs of views. In our GPU implementation, one such evaluation with Radon intermediate functions of 768×768 bins takes about 350 ms on mobile hardware. The cost can be visualized in a grayscale image by arranging the cost $\mathrm{EC}(\mathbf{P}_i^{\boldsymbol{\varphi}}, \mathbf{P}_j^{\boldsymbol{\varphi}}, I_i, I_j)$ in the elements (i, j) of an $n \times n$ matrix; in the following called "cost image". Due to symmetry of EC, this matrix would be symmetric and the diagonal elements are undefined and set to zero (inconsistency of a projection with itself). In Figure 5.5, bottom center, we therefore use the bottom left half of the image to shade by the inconsistency of initial guess $\mathrm{EC}(\mathbf{P}_i, \mathbf{P}_j, I_i, I_j)$, given by scanner calibration, while the upper right is shaded based on the optimization result $\mathrm{EC}(\mathbf{P}_i^{\boldsymbol{\varphi}\star}, \mathbf{P}_j^{\boldsymbol{\varphi}\star}, I_i, I_j)$. The overall brightness of the upper right is reduced when compared to the lower left (i.e. higher consistency). However, the periodicity of the heart-beat becomes clearly visible as regular brighter regions. This remaining inconsistency most likely mostly goes back to the non-linearity of the heart motion, which obviously cannot be fully explained by our simplistic motion model. We optimized the EC metric using a repeated coordinate-wise grid-search. Since grid-search cannot be applied to 133 dimensional parameter space for practical run-time reasons, only a coordinate-wise grid-search was possible. The periodicity, however, sometimes leads to jumps in this approach. Absolute shift is also hard to optimize, since the EC metric changes only very little when all views are shifted by the same amount at once. We therefore, also investigated a more stable graph-based optimization approach named alpha-Expansion [Fels 17], which avoids the problem. The experiments in Felsner et al. indicate that optimization is more stable, when iterating over all possible shifts and applying the shifts to all projections at the same time, rather than testing all shifts of a single projection before proceeding to the next. This is true even when no regularization is used.

5.2.4 Comparison to Fourier Consistency

We evaluated both epipolar consistency based on Grangeat and Fourier consistency conditions (FCC) [Unbe 17b]. The ground truth are shifts based on a human clicking on certain features in the images, cf. Figure 5.6, black dashed. Due to some constraints in the implementation of FCC, we used only 128 instead of 133 projections. Both FCC and EC follow the manual ground truth well. EC seems to reflect the details of the motion a little better, except for the last few images, where it slightly over-estimates the motion. In Figure 5.5, bottom right, we show that both breathing (blue dashed) and cardiac (solid blue) motion, which can be recovered by frequency analysis [Unbe 17b]. However, Unberath et al. [Unbe 18] has shown that performance of a related auto-focus based method currently shows better reconstruction results than any of our DCC based methods. Note that minimizing the energy in the wedge-shaped region in Fourier space is not the same as enforcing a consistency condition.

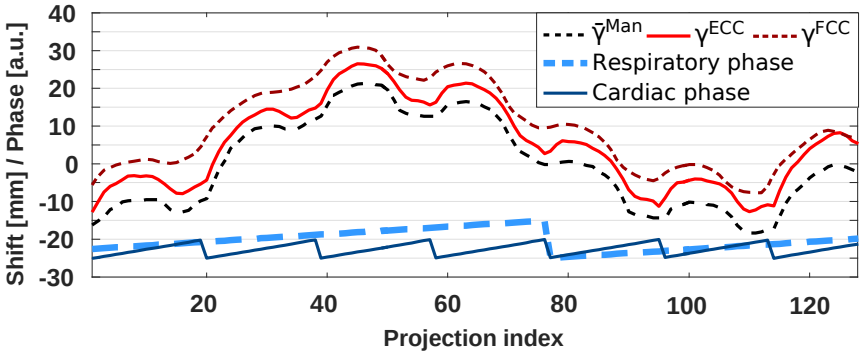

Figure 5.6: Comparison of the results by enforcing Fourier properties of the sinogram and epipolar consistency based on Grangeat. The legend indicates manual shifts (Man) and those obtained by epipolar consistency (ECC) and Fourier pseudo-consistency (FCC).

Especially in the discrete Fourier transform, this minimization is only a heuristic ("pseudo-consistency") and can lead to a bias towards shifting the center of mass of the projection to the rotation axis (although not shown in this work).

5.2.5 Epipolar Shroud

Motion extraction from line integral data has been done before epipolar consistency was developed. Rit et al. [Rit 12] presents a study of the variability of respiratory diaphragm motion based on [Zijp 04], which computes horizontal sums in images and is sometimes referred to as Amsterdam shroud. In rotational scans the rotation axis is typically aligned with the image v-axis. Recall that two images from such a scan, with primary angle difference less than about 120° have epipolar lines almost horizontal and almost parallel. Especially for primary angle difference less than about 30°, EC is therefore at its core computing horizontal image sums.

With this relationship in mind, we present in Figure 5.7, left, a plot of the consistency of image v-shifts (vertical axis in a range of 150 px) of a single image (projection index 0, left) for all other 132 projection images (on the horizontal axis). The darker a pixel in this figure, the less inconsistency we have for a specific shift. In the left half of this plot, we observe the motion pattern as a dark curve, which follows well the respiratory and heart motion. In the right half of the image, this pattern is more and more difficult to follow since a narrow band with entirely different shape disrupts the curve. This region corresponds exactly to projections with about 180° degrees primary angle difference. In these situations, the epipoles lie inside the image and epipolar lines are not simply aligned with the horizontal image axis. In this situation, the magnitude of epipolar consistency also changes.

In Figure 5.7, second from the left, the plot is repeated with projection index 132 (i.e. the last image in the scan) as a reference. Unsurprisingly, the epipole is contained in the image for different projection indices. In order to exclude regions where the epipole enters the image and produce a single, Amsterdam-shroud like image, we now mix the two plots based on the relative distance of the baseline to

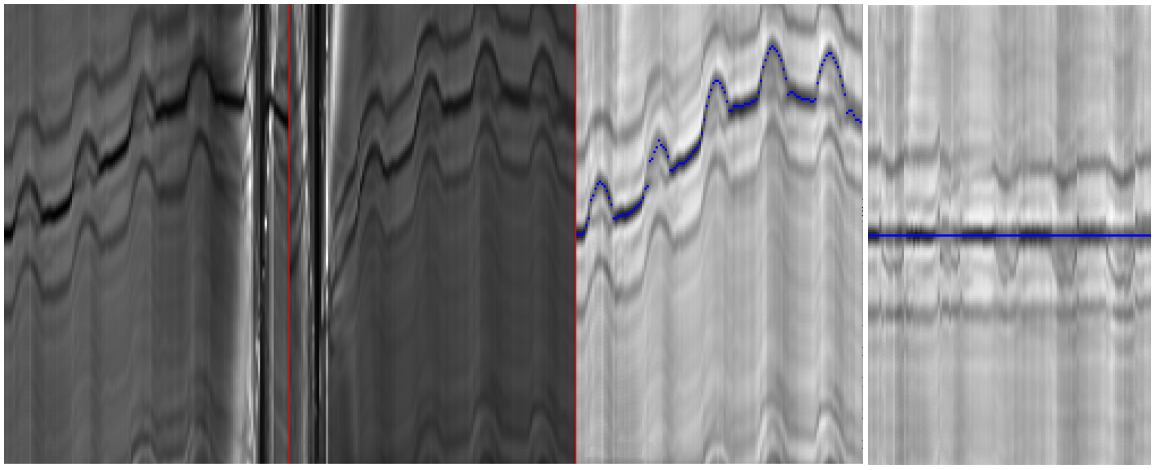

Figure 5.7: For plots over consistency by projection index (horizontal axis) versus detector shift up to 150 px (vertical axis). The respiratory and heart motion can be seen. From left to right: Consistency with projection index 0, consistency with projection index 133, a mixing of the two, based on the relative distance of the baseline to the origin and, on the right, the same image after shifting the projections based on the minimum inconsistency. Observe that the first two images show an irregular change of pattern for opposing views. This is due to the epipoles coming closer to and finally entering the image. The two rightmost images appear brighter due to window-level effects: the extreme values for opposing projections are removed with respect to the two leftmost images.

the origin (iso-center). The result is shown in Figure 5.7, second from the right. The blue dots indicate the minimum in each column. Apparently, this can be used as a pretty good estimate of cranio-caudal motion, similarly to the discussions in the last sections. As a sanity check, we also applied this mixing and grid-search algorithm for a scan that was already corrected for respiratory and cardiac motion using ECC. The result is a clear minimum for $v = 0$ shown as a horizontal blue straight line. One important note is that the algorithm, in this way, only works if shift estimates from the two reference projections agree. In this case, this has been achieved by shifting projection with index 132 based on the consistency with projection index 0 first. The method could serve as an initial estimate or a faster alternative, although we expect results to be less stable, considering only a small portion of the available information is actually used. If one of the reference images has a segmentation issue, for example, the method will inevitably fail.

5.2.6 Summary

We have shown that epipolar consistency can be used to estimate heart motion, in spite of truncation, periodic motion and non-linear transformations related to the cardiac cycle. Consistency can be used to extract information about breathing and heart cycle similarly to ECG. We have seen that EC performs comparably to Fourier pseudo-consistency, while the EC algorithm is more general, in that it does not assume a circular trajectory. However, the hopes that consistency might allow

an initial motion correction for reconstruction of the arteries is not supported by our data. In fact, motion compensation algorithms based on iterative reconstruction were shown to be better suited for an accurate estimation of heart motion. The advantage of EC remains that it is fast and does not require reconstruction.

5.3 3D-3D Registration in Raw Data Domain

5.3.1 Parametrization

In this section we, discuss the potential of EC for 3D-3D registration. The idea is to pre-align an existing CT image with the current position of the patient or to align two CT images. The computations shall be done in the raw-data domain to provide a much faster and less computationally expensive solution than intensity-based 3D-3D registration. In the following, we will work with two sets of projection images, the (registration) source projection images given by an index set $\mathcal{S}$, which show the same object as the target projection images given by an index set $\mathcal{T}$. The two are related by some unknown rigid transformation $\mathbf{T}^{\boldsymbol{\varphi}}$, defined in Eq. 5.10 with six parameters. We model the rigid 3D-3D registration problem as a minimization of the pairwise cost EC over the parameters $\boldsymbol{\varphi}$

$$\boldsymbol{\varphi}^\star = \operatorname*{argmin}_{\boldsymbol{\varphi}} \, \mathrm{M}\left(\mathcal{T}, \, \mathcal{S} \,|\, \phi\right), \tag{5.16}$$

with

$$\mathrm{M}\left(\boldsymbol{\varphi}\right) = \sum_{(t,s)\in\mathcal{T}\times\mathcal{S}} d_{\mathcal{B}} \cdot \mathrm{EC}\left(\mathbf{P}_t, \, \mathbf{P}_i\mathbf{T}_\phi^{-1}, \, I_t, \, I_s\right). \tag{5.17}$$

The heuristic weighting with the baseline distance $d_{\mathcal{B}}$ is due to a higher sensitivity of the cost function EC for opposing views rather than neighboring views. Note that it is equivalent to either transform the object by $\mathbf{T}_{\boldsymbol{\varphi}}$ or to transform all source and detector positions by the inverse $\mathbf{T}_{\boldsymbol{\varphi}}^{-1}$. As before, the optimization problem is non-linear and non-convex and can be solved using gradient-based or gradient-free non-linear optimization software.

5.3.2 Simulation Study

As a proof of concept for EC-based registration, we investigated noise-free forward projections of a pumpkin phantom, see Figure 4.6. The transformation parameters are

$$\boldsymbol{\varphi}^\star \approx (5.7\,\mathrm{mm}, \, 6.8\,\mathrm{mm}, \, 1.2\,\mathrm{mm}, \, -5.66°, \, 5.0°, \, -4.4°)^\top. \tag{5.18}$$

We simulated two 360° full scans with 106 projections each of 1024×760 pixels with a source-detector distance of 611 mm and a source-iso-center-distance of 404 mm, shown in Figure 5.8, left. The trajectory mimics a table-top CT system with parameters chosen such that the phantom was not truncated in the projections. The Radon intermediate functions $\mathfrak{G}_i$ were pre-computed with 786×786 bins, which takes less than 10 seconds for all 212 projections using the GPU. In Figure 5.9 we show plots of the metric M over errors in individual parameters. For all six parameters, the plots

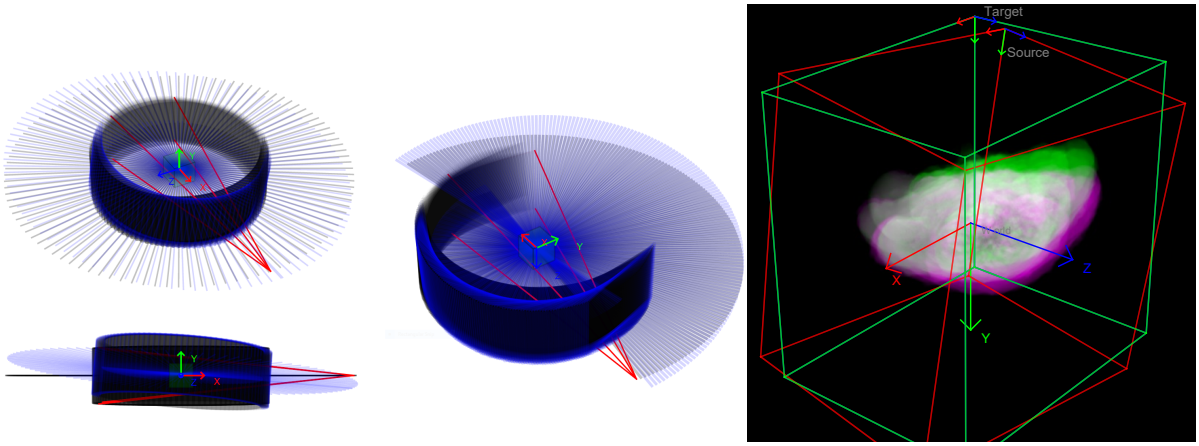

Figure 5.8: Left: Visualization of the full-scan trajectory with 106 views. Original trajectory in black and same trajectory transformed by optimal $\mathbf{T}_{\boldsymbol{\varphi}}^{-1}$ in blue (two perspectives for better visualization of transformation). Right: Same visualization for a short-scan trajectory taken from an actual Artis Zeego C-arm system. Only 166 out of 496 projections are shown.

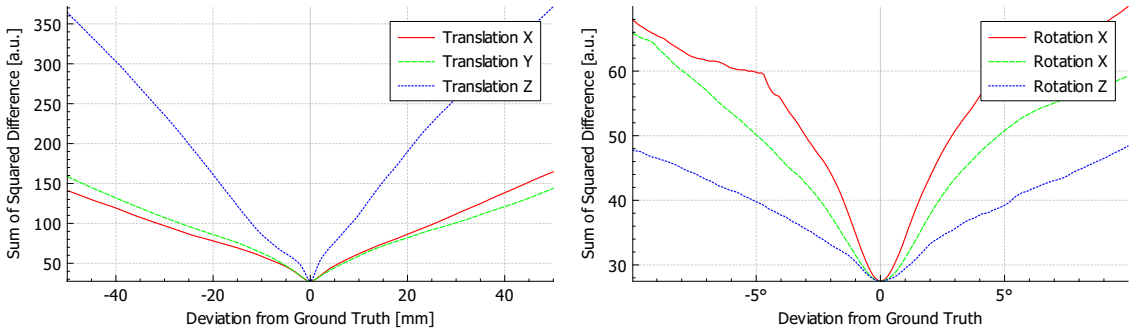

Figure 5.9: Plots of the six parameters as deviations from the ground truth $\boldsymbol{\varphi}^{\star}$ (shown at the origin). The cost function shows a clear minimum for all six parameters for the correct alignment.

show a clear minimum of the cost function for correct registration (i.e. at 0 in these plots), which means that the cost function is sensible.

We ran a variant of the gradient-free algorithm Simplex on the initial guess $\boldsymbol{\varphi} = 0$. The optimization converged in $\approx$ 450 iterations and we were able to recover $\phi^\star$ with an accuracy of ≈ 0.03 mm $\approx 0,06°$ in all parameters. Optimization took 9 seconds. Visually, the bounding boxes of ground truth and registration result in apparently perfect overlap. To demonstrate the advantage of registration without prior reconstruction, we repeated the experiments with just 9 projections in both target and source scan. Again, we conduct a random study with $n = 100$ samples, with random translation of ± 25 mm and rotations of $\pm 10°$. In this realization, the mean absolute offset of ± 12.6 mm and 4.98°. After optimization, there were four outliers. The inliers had a maximum error of 0.07 mm and 0.04°. With that little data, a single registration took less than half a second on average.

We repeated the same experiment with Gaussian noise of standard deviation $\approx$ 10% of the maximum intensity added to the 9 projections of both scans. The amount of noise added was considerable, corresponding to a very low-dose acquisition of just 9 projections, left. However, before running the algorithm, we allowed the preprocessing to apply Gaussian smoothing. Results deteriorated to eight outliers. The inliers had a mean error of 0.21 mm and 0.33°. It is expected that noise averages out with additional data. We noticed that by increasing the number of projections to 14 per scan, the algorithm coped better and results improved to three outliers. The inliers had a mean error of 0.11 mm and 0.25°. Optimization took ≈ 0.7 seconds on average. Note that for all 106 projections, there are no outliers for the noisy data and mean error was 0.04 mm and 0.024°.

5.3.3 Physical Head Phantom

After promising numerical experiments, we tested our algorithm on real acquisitions of a human head phantom. We acquired three scans of the phantom in different position with a Siemens Artis Zeego clinical C-arm. The 20-second short-scan protocol acquires 496 projections of 1240×960 (after 2×2 binning on the detector hardware). The scanner calibration showed a mean source-detector distance of 1198 mm and a source-detector distance of 785 mm. Angular range was 198° and the angular step between two projections was $0.4° \pm 0.047°$. All three scans were reconstructed to a $512 \times 512 \times 398$ voxel volume with a spacing of 0.486 mm. We implemented a simple intensity-based registration algorithm based on the sum of squared intensity difference to generate reference registrations. Visual inspection, cf. Figure 5.10 for data sets 0 and 1, shows perfect alignment of the scans. The parameters of the reference registration were

$$\phi_{01}^{\text{ref}} = (6.31 \text{ mm}, -2.13 \text{ mm}, 2.53 \text{ mm}, 0.007°, 0.396°, 0.012°)^\top \tag{5.19}$$

and

$$\phi_{02}^{\text{ref}} = (8.49 \text{ mm}, -2.34 \text{ mm}, 3.90 \text{ mm}, 0.014°, 0.636°, 0.011°)^\top. \tag{5.20}$$

In Figure 5.11 we show plots of the EC cost function over the six parameters (for translation, left, and three rotation, right). The rotation axis in this example is

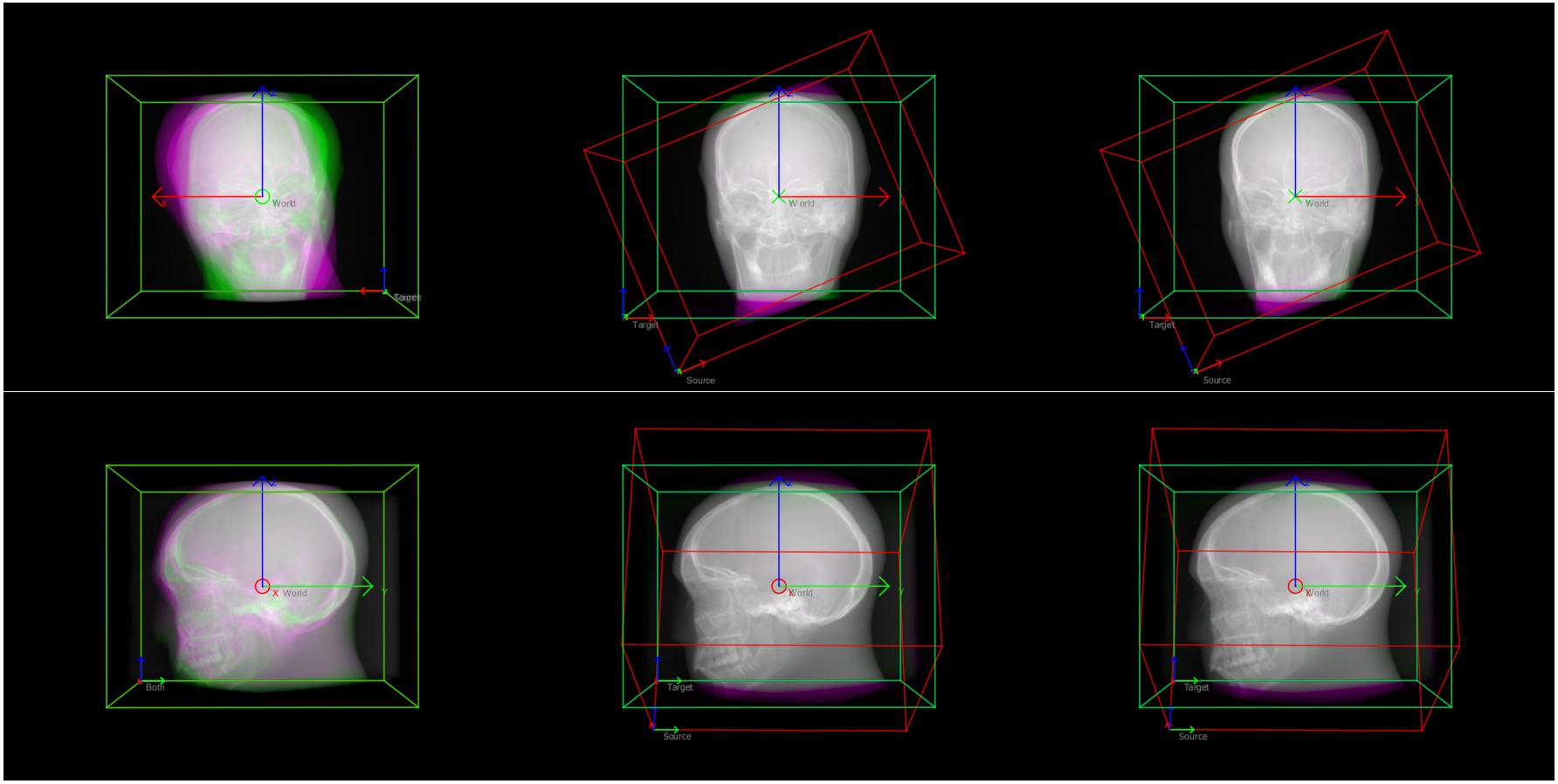

Figure 5.10: Overlay of the first two real scans of a physical human head phantom. Registration target is in the green channel and source is in the red and blue channels. Any misalignment shows as green, respectively purple hue. Left: before registration. Center: EC-based registration. Right: Reference intensity-based registration. Across most of the image, alignment is near perfect, so registration was successful. Bounding boxes visualize transformation between the two scans, source in red, target in green. EC-based and reference registration are visually identical.

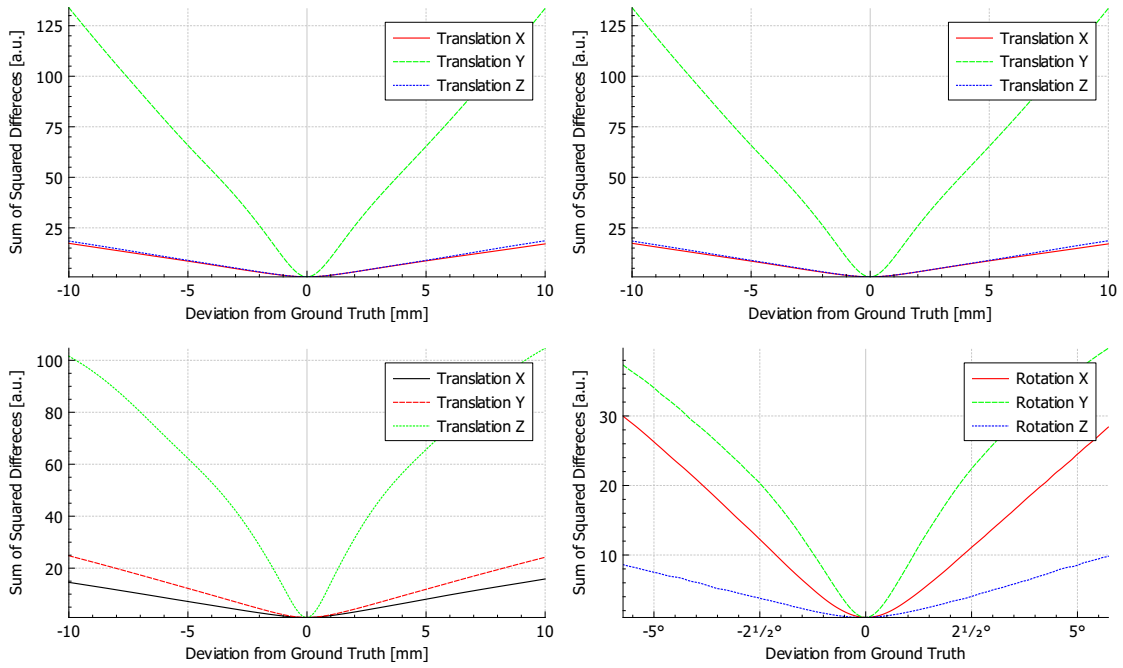

Figure 5.11: Plots of the metric M for registration of real scan one and two and one and three. In each plot, the minimum corresponds well with the correct alignment.

roughly aligned with the Z-axis. The plot is centered at the reference parameters (in this case ϕ_{01}^{ref} for scan 1), which is clearly a strong minimum with smooth slopes in both positive and negative direction. Starting from the zero-vector as initial guess, optimization of the EC-metric was able to recover the reference parameters well below voxel accuracy in under 10 seconds using 11 views from each scan.

5.3.4 Random Study

Finally, we conducted a random study with $n = 100$ samples and with random translation of ± 25 mm rotations of $\pm 5°$ for the real phantom data. The realization of the experiment was on average 12.6 mm and 2.44°. The error after optimization was 0.25 mm and 0.025° with no outliers. When only 9 projections per scan were used, there were 13 outliers of more than one mm error and each registration took under one second. The new algorithm for rigid 3D-3D registration computed tomography scans works in projection domain of flat-panel detectors. It uses data consistency conditions to find the correct geometric pose of one acquisition with respect to another. We validated our registration algorithm on numerical phantom data, where the method performed extraordinarily well for full-scan without truncation of the object. We were able to find correct alignment without an initial guess. We evaluated the method on real data of a head phantom. This data is acquired on a short-scan trajectory and includes several physical effects not modeled by the beer-lambert law. Despite this, a rough initial guess up to about ± 25 mm and $\pm 5°$ can be corrected for in a robust way. A global optimization, at this point, works only for simulated data, although we did not observe a local minimum with lower cost than correct alignment.

5.3.5 Summary

We have presented an algorithm which performs 3D alignment of two sets of projection images, without the need for reconstruction. The algorithm could be used as a pre-aligment of an existing CT scan with the current patient pose by acquisition of a few reference projections. In addition, it is able to register two CT acquisitions in the raw data domain. We have evaluated the algorithm against a naive SSD-based 3D-3D registration algorithm in the domain of the reconstructed image. We have seen that we can recover small rigid transformations between the sets with reasonable accuracy using much less data than the reconstruction-based approach. In addition, we have shown that the algorithm can handle large amounts of simulated noise.

A better optimization strategy would likely allow for global registration, for example starting with multiple initial guesses. A this point, we would like to point out that epipolar consistency has also been used to find symmetry planes in the object [Preu 18]. This problem is virtually the same as registering two CT scans, where one of them has been flipped along any axis. The only difference is that the determinant of the sought after registration matrix is negative in that case. However, the idea of using EC for registration is novel and interesting due to its speed. It could be used to align a reconstructed 3D image with projections of another scan simply by using forward projection of the 3D image, plus, it is able to work with very little dose, for example to accurately align a 3D CT image with a patient in an interventional setting by just taking a few shots from different directions.

CHAPTER 6

Outlook and Summary

6.1 Outlook

This work can be seen as basic research into applicability of consistency conditions to FDCT data and demonstrated three metrics of epipolar consistency. However, most experiments used Grangeat consistency, since this was the first epipolar consistency developed. Just because the relationship between FBCC and GCC is merely a derivative, FBCC may still bear advantages in applications where a constant intensity offset, i.e. the absolute intensity is important. The derivative operation in Grangeat consistency has the effect of enhancing borders, which is a common instrument in other alignment or registration methods. The derivative also removes constant offsets in the redundant information, which may partly explain away truncated structures and make it more robust. A thorough comparison in all presented applications is required. The consistency conditions based on Smith and Grangeat appear to behave quite differently. Current research is working on finding other applications, not related to motion [Wurf 18, Hoff 18]. Future work must now focus on applications with real data. With the exception of calibration correction, no other application has been studied in detail.

Truncation remains the major obstacle. While one method is presented specifically for angiography, it is currently unknown if similar concepts may be applicable to tracking in fluoroscopy, for example, where surgical instruments may present a similar problem. In applications such as 3D-3D registration our algorithm does not tap into one important source of information. Intra-scan inconsistency may give strong evidence for an initial alignment, when present in both scans. More importantly, our naive optimization approach should be replaced with optimizers, which are also used for global 3D-3D registration using image similarity metrics. Only then, comparison is fair. Alignment of patient to CT seems a realistic application to study, since no additional data needs to be acquired. A clinical partner may already have data to thoroughly investigate this application.

This work may open new perspectives on existing heuristic methods [Rit 12, Zijp 04] and put them on a solid theoretical foundation. It may be worthwhile to find applications where such simple heuristics are used and possibly extend or im-

prove these using EC. Following energy as it moves along epipolar lines between views may be a superior additional source of information, akin to Wein et al. [Wein 11]. Higher-order methods and completeness arguments may be interesting. Clackdoyle et al. [Clac 16] presented an approach to higher orders for circular cone-beam trajectories, it is based on higher orders of differentiation. Finding additional usable information in three or more general projections would be extremely valuable.

Finally and most importantly, this entire work could be understood as standard computer vision research with the specialty that transmission images replace opaque visible light imaging. Classical computer vision methods are well-researched but usually rely on known and detected points and statistical algorithms for stability. So much more computer vision research can likely be transferred to transmission imaging, by replacing the algebraic and or geometric error on point correspondences with epipolar consistency. Many interesting effects may ensue, and certainly optimization will be an obstacle. One concrete example where these considerations my be advantageous is the estimation of the fundamental matrix directly from two transmission images. This may be relevant even for motion and calibration correction, since the intrinsic properties of the fundamental matrix correctly represent the geometry. While most parametrizations used in this work suffer, to some extent, from some kind of geometric dependency, decomposition of the fundamental matrix can produce stable and unambiguous parameters for two views. A close look at auto-calibration methods and even factorization algorithms that focus on epipolar consistency may produce quite different perspectives to the geometry of tomographic imaging.

6.2 Summary

The X-ray and Radon transforms are introduced in **Chapter 1** as integral operators. A Cartesian-to-polar change of variables presents the so-called generalized projection theorem. The Radon transform is closely related to the Fourier transform, allowing for reconstruction of an object from its 2D Radon transform. In computed tomography, algebraic and analytic reconstruction algorithms exist. They have allowed cross-sectional views through objects and patients since the 1970ies and they exist for 2D and 3D parallel and cone-beam geometry. However, reconstruction algorithms usually assume a perfect Lambertian absorption along straight monochromatic rays and accurately known acquisition geometry. Real data violates these assumptions due to beam-hardening, scatter, inaccurate scanner calibration or patient motion. Artifact reduction techniques use prior information, additional sensors or iterative procedures to achieve good image quality under these circumstances. This work, by contrast, addresses data consistency conditions. These are mathematical conditions of the projection operator.

Algebraic reconstruction encodes the linear relationship between a discretized version of the object and its projection by a system matrix. Reconstruction can be performed by inverting this matrix. In this context, data consistency conditions arise as the right null-space of the matrix inverse. No object exists, which produces projections in this null-space. Portions of acquired data which project to the null-space are inconsistent. In other words, data consistency conditions are range conditions of the projection operator.

In continuous two-space, the Radon transform has inherent range conditions as well. So-called moment curves are weighted integrals over the detector variable. According to the Helgasson-Ludwig consistency conditions (HLCC), these take the form of polynomials of a certain degree. For example, the mass of the projection (order 0) is constant for all projection angles and the center of mass of the projection (order 1) is the projection of the center of mass. Another way to characterize the range of the Radon transform is by considering its Fourier transform. It contains wedge-shaped regions with low energy. Extensions to fan- and cone-beam exist, however some have strong assumptions making them impractical while others are heuristic.

A true 3D cone-beam consistency condition is John's equation. It takes the form of a second order partial differential equation for a source moving on a plane parallel to the detector. Direct application of the PDE is difficult. It can also be expressed as a wave equation where motion in a certain direction fulfills a consistency property in Fourier space. Later, this property was simplified to single line-integral over the detector by considering only the constant term at zero-frequency. This condition is referred to as linear tomography consistency (LTC).

Chapter 2 introduces projective geometry and the pinhole camera model as the basis for epipolar geometry. Homogeneous coordinates for points and lines in two and three dimensions, as well as planes are introduced. General join and meet operations are defined in two and three dimensions and both can be expressed in terms of the Plücker matrix. In projective three-space, the line is represented via Plücker coordinates. They are six-dimensional and can be interpreted as two three-vectors. One points in the direction of the line, while the other defines a plane through the origin which contains the line. They are orthogonal and dividing the norm of the moment by the norm of the direction gives the distance of the line to the origin. Plücker coordinates thus have only four degrees of freedom.

The linear relationship between two and three dimensions can be described by central projection. Central projection is the geometry of pinhole cameras and can be written as a three-by-four projection matrix. In the context of X-ray imaging, the image plane is the detector and the center of projection is the X-ray source. If the size of a detector pixel is known, then the source-detector geometry is fully defined by a projection matrix. In addition, motion of the detector and motion of the object can be written as left- and right-multiplication of 2D and 3D transformation matrices with the projection matrix. Epipolar geometry is the geometry of two pinhole cameras. The two source positions define a so-called baseline. An epipolar plane is defined as any plane containing the baseline. The core idea of epipolar geometry is that the intersection of an epipolar plane with the two detectors defines two corresponding lines in the projection images. The 2D epipolar lines are related via the same 3D epipolar plane.

Chapter 3 introduces three types of epipolar consistency (EC) of X-ray projection images. John's equation assumes a source moving parallel to the detector. Projective geometry allows for the generalization of LTC to any flat-detector geometry by re-projection of existing images to arbitrary detector planes. The two projection images define an epipolar geometry. Re-projection to a common detector plane parallel to the baseline is an instance of stereo rectification which is a well-known algorithm in computer vision. The re-projection can be understood as a virtual rotation, trans-

lation and change of the focal length. Applying LTC after rectification is a type of EC we call fan-beam consistency conditions (FBCC), because only the two fans of X-rays contained in a single epipolar plane are used.

Next, the connection to the Clack-Defries analytical reconstruction algorithm which also relies on line integrals on the detectors is established. At the core of this algorithm lies the Radon intermediate function. For the ramp and derivative filters of the Radon transform, a direct connection between the 2D lines and 3D planes exist. Since corresponding epipolar lines go back to the same epipolar plane, the algorithm directly expresses data redundancy. This results in two more EC conditions, namely for Grangeat (derivative) and Smith (ramp) Radon intermediate functions. Grangeat's theorem can be illustrated using geometry and a change of variables for line integrals.

At this point, an algorithm to compute a metric of EC is suggested by comparing redundant information from two X-ray projection images using the sum of squared difference. While the first part of the algorithm deals with an efficient way to sample epipolar lines, the last part of the algorithm can be, either, a weighted integration to compute FBCC, or, sampling pre-computed Radon intermediate functions at corresponding positions. These corresponding positions describe two sinusoidal curves in the Radon intermediate functions. The three flavors of epipolar consistency are compared by the example of two real X-ray images of the pumpkin phantom. Evaluating FBCC is considerably more expensive. A derivative in angular direction of FBCC turns out to be identical Grangeat consistency.

Chapter 4 examines applications of EC for motion estimation. A general pairwise cost-function is defined along with a general parametrization for all linear transformations (for example translation, rotation and affine transformations). Three motion compensation applications are then addressed by the same optimization problem, only different parametrizations.

The first is tracking an unknown object under fluoroscopy. The pumpkin phantom is used to prove that a rigid transformation can be recovered using only a few known reference projections. The method is compared to 2D-3D registration, which uses a full 3D reconstruction to compute the same motion. Random studies show stability of the algorithm and accuracy which may be acceptable in some applications. However, truncation or the presence of surgical instruments remain an unsolved problem. The second application is rotational angiography. In this case, heart vessels are visualized by injection of contrast agent under rotation. The data is heavily truncated, leading to extreme inconsistency, in addition to cardiac and respiratory motion. An in-painting based virtual subtraction algorithm is presented, which allows for EC to estimate cranio-caudal motion of the heart and extract both cardiac and respiratory phase. A comparison to a Fourier pseudo-consistency-based method and a manual method shows similar performance. The third application is rigid 3D-3D alignment of two CT data sets using consistency conditions. The method is evaluated on simulated full-scan data and real short-scan data. Random studies of a head phantom show stability of the registration, although global alignment was successful only on simulated data. This is mostly a question of exhaustive optimization or a smart heuristic, however. Alignment of the real scans is fast and accurate.

List of Symbols

Abbreviations

CT	Computed Tomography, visualization of a slice through an object
DCC	Data Consistency Conditions, including HLCC, ECC and others.
FCC	Fourier consistency conditions
FDK	Feldkamp, Davis and Kress, reconstruction algorithm
GCC	Grangeat Consistency Conditions, a kind of EC
HLCC	Helgason-Ludwig Consistency Conditions
LTC	linear tomosynthesis condition
PDE	Partial differential equation
SCC	Smith Consistency Conditions, a kind of EC
vDSA	virtual digital subtraction angiography
FBCC	Pairwise fan-beam consistency. Identical to LTC after a re-projectoin to a common virtual detector plane.

Calculus

$\mathbb{P}^n$	real projective space.
$\mathbb{S}^1$	unit circle $\mathbb{S} = \{\boldsymbol{a} \in \mathbb{R}^2 : \|\boldsymbol{a}\| = 1\}$
$\mathbb{S}^2$	unit sphere $\mathbb{S} = \{\boldsymbol{a} \in \mathbb{R}^3 : \|\boldsymbol{a}\| = 1\}$
f^{2D}	2D object function, $f^{2D} : \mathbb{R}^2 \mapsto \mathbb{R}$
f	3D object function, $f : \mathbb{R}^3 \mapsto \mathbb{R}$
$(\mathcal{F} f^{2D})$	2D Fourier transform of object function f^{2D}
$(\mathcal{F}_x)$	partial Fourier transform for the spectral variable $\xi \leftrightarrow x$
$\mathcal{R}$	Radon transform, operator notation
$\mathcal{X}$	X-ray transform, operator notation
δ	Dirac impulse

Geometry —Matrices

$\mathbf{A}$ a real matrix $\mathbf{A} \in \mathbb{R}^{m \times n}$

$\mathbf{A}^\top$ transpose of matrix $\mathbf{A}$

$\mathbf{A}^{-1}$ inverse of invertible matrix $\mathbf{A}$

$\mathbf{A}^+$ pseudo-inverse of matrix $\mathbf{A}$

$\mathbf{H}$ letter $\mathbf{H} \in \mathbb{R}^{3\times3}$ (sometimes with decorators) used specifically for 2D homographies. $\mathbf{H}$ has positive determinant, unless it is a reflection.

$\mathbf{T}$ letter $\mathbf{T} \in \mathbb{R}^{4\times4}$ (sometimes with decorators) used specifically for 3D homographies. $\mathbf{T}$ has positive determinant, unless it is a reflection.

$\mathbf{P}$ letter $\mathbf{P} \in \mathbb{R}^{3\times4}$ (sometimes with decorators) used specifically for projection matrices.

$\mathbf{F}$ letter $\mathbf{F}$ (sometimes with decoorators) used specifically for the fundamental matrix. $\mathbf{F}$ has rank two and encodes the relative geomety of two projection matrices.

$\mathbf{R}$ letter $\mathbf{R}$ (sometimes with decorators) used specifically for rotation matrices. $\mathbf{R}^\top = \mathbf{R}^{-1}$ and $\det \mathbf{R} = 1$

$[\mathbf{l}]_\times$ 3×3 Plücker matrix.

$[\mathcal{L}]_\times$ 4×4 Plücker matrix.

Geometry —Scalars and Vectors

α angle $\alpha \in \mathbb{R}$ in radians

a scalar $a \in \mathbb{R}$

$\mathbf{a}$ homogeneous coordinates of lines, for example $\mathbf{l}$, $\mathbf{m} \cdots \in \mathbb{P}^2$ and points, for example $\mathbf{a}$, $\mathbf{b}$, $\mathbf{x} \cdots \in \mathbb{P}^2$ in projective two-space

$\mathring{\boldsymbol{a}}$ real unit vector. $\mathring{\boldsymbol{a}} \in \mathbb{S}^1$ or, depending on context, $\mathring{\boldsymbol{a}} \in \mathbb{S}^2$

$\mathring{\boldsymbol{a}}^\perp$ perpendicular vector to $\mathring{\boldsymbol{a}}$. $\mathring{\boldsymbol{a}}^\top \mathring{\boldsymbol{a}}^\perp = 0$

$\bar{\mathbf{a}}$ homogeneous coordinates of planes, for example $\bar{\mathbf{e}}$, $\bar{\mathbf{f}} \cdots \in \mathbb{P}^3$ and points, for example $\bar{\mathbf{a}}$, $\bar{\mathbf{b}}$, $\bar{\mathbf{x}} \cdots \in \mathbb{P}^3$ in projective three-space

$\boldsymbol{a}$ three-dimensional real vector. $\boldsymbol{a} \in \mathbb{R}^3$

$\mathcal{L}$ Plücker coordinates of a line in projective three-space.

$\tilde{\mathcal{L}}$ dual Plücker coordinates of $\mathcal{L}$. Elements of $\mathcal{L}$ are re-arrenged such that $[\tilde{\mathcal{L}}]_\times [\mathcal{L}]_\times = \mathbf{0} \in \mathbb{R}^{4\times4}$.

$\mathbf{l}^\infty$ line at infinity. Two parallel lines with direction $\mathring{\boldsymbol{d}} = (u, v)^\top$ intersect in $\mathbf{x} = (u, v, 0)^\top$ which is a point on the line at infinity $\mathbf{l}^\infty = (0, 0, 1)^\top$

$\bar{\pi}^{\infty}$ plane at infinity. $\bar{\pi}^{\infty} \cong (0,0,0,1)^{\top}$

Other Symbols and Functions

$f^{\bullet}$ point-shaped 2D object function. Zero everywhere exept for one point

$p^{\bullet}$ Radon transforrm of point-shaped object. Sinusoidial curve

$\tilde{g}(\boldsymbol{c}, \boldsymbol{x})$ normalized X-ray transform.

$\hat{g}(\boldsymbol{c}, \boldsymbol{\xi})$ partial fourier transform of normalized X-ray transform. Fourier space of a projection image.

$\hat{p}(\alpha, \sigma)$ partial Fourier transform of parallel projection of object function f^{2D} over detector variable $s \leftrightarrow \sigma$ In operator notation $\hat{p} = (\mathcal{F}_s \left((\mathcal{R} f^{2D}) \right))$

$p_w(\alpha)$ integral over the detector variable s of a Radon transform weighted by function $w(s)$ for a fixed projection angle α. See also: generalized projection theorem

$p_m(\alpha)$ integral $p_m(\alpha)$ over the detector variable s of a Radon transform weighted by function $w(s) = s^m$ for a fixed projection angle α. See also: moment curve

Bibliography

[Aach 01] T. Aach and V. Metzler. “Defect Interpolation in Digital Radiography - How Object-Oriented Transform Coding Helps”. In: M. Sonka and K. M. Hanson, Eds., *SPIE Vol. 4322: Medical Imaging 2001*, pp. 824–835, SPIE, San Diego, USA, February 17–22 2001.

[Abdu 18] S. Abdurahman, R. Frysch, R. Bismark, S. Melnik, O. Beuing, and G. Rose. “Beam hardening correction using cone beam consistency conditions”. *IEEE Transactions on Medical Imaging*, 2018.

[Aich 12a] A. Aichert, W. Wein, A. Ladikos, T. Reichl, and N. Navab. “Image-based tracking of the teeth for orthodontic augmented reality”. In: *International Conference on Medical Image Computing and Computer-Assisted Intervention*, pp. 601–608, Springer, 2012.

[Aich 12b] A. Aichert, M. Wieczorek, J. Wang, M. Kreiser, L. Wang, P. Fallavollita, and N. Navab. “The colored x-rays”. In: *Workshop on Augmented Environments for Computer-Assisted Interventions*, pp. 45–54, Springer, 2012.

[Aich 14] A. Aichert, N. Maass, Y. Deuerling-Zheng, M. Berger, M. Manhart, J. Hornegger, A. Maier, and A. Doerfler. “Redundancies in X-ray images due to the epipolar geometry for transmission imaging”. In: *4th International Conference on Image Formation in X-Ray Computed Tomography*, pp. 333–336, 2014.

[Aich 15a] A. Aichert, M. Berger, J. Wang, N. Maass, A. Doerfler, J. Hornegger, and A. K. Maier. “Epipolar consistency in transmission imaging”. *IEEE Transaction on Medical Imaging*, Vol. 34, No. 11, pp. 2205–2219, 2015.

[Aich 15b] A. Aichert, J. Wang, R. Schaffert, A. Dörfler, and J. Hornegger. “Epipolar Consistency in Fluoroscopy for Image-Based Tracking.”. In: *British Machine Vision Conference (BMVC)*, 2015.

[Aich 16] A. Aichert, K. Breininger, T. Köhler, and A. K. Maier. “Efficient Epipolar Consistency”. In: *4th International Conference on Image Formation in X-Ray Computed Tomography*, pp. 383–386, 2016.

[Aich 18a] A. Aichert, B. Bier, L. Rist, and A. K. Maier. “Projective Invariants for Geometric Calibration in Flat Panel Computed Tomography”. In: *5th International Conference on Image Formation in X-Ray Computed Tomography*, pp. 69–72, 2018.

[Aich 18b] A. Aichert, J. Lesaint, T. Würfl, R. Clackdoyle, L. Desbat, and A. K. Maier. “Stereo Rectification for X-ray Data Consistency Conditions”. In: *5th International Conference on Image Formation in X-Ray Computed Tomography*, pp. 198–201, 2018.

[Ande 84] A. H. Andersen and A. C. Kak. “Simultaneous algebraic reconstruction technique (SART): a superior implementation of the ART algorithm”. *Ultrasonic imaging*, Vol. 6, No. 1, pp. 81–94, 1984.

[Berg 17] M. Berger, Y. Xia, W. Aichinger, K. Mentl, M. Unberath, A. Aichert, C. Riess, J. Hornegger, R. Fahrig, and A. K. Maier. "Motion compensation for cone-beam CT using Fourier consistency conditions". *Physics in Medicine & Biology*, Vol. 62, No. 17, p. 7181, 2017.

[Bier 17] B. Bier, A. Aichert, L. Felsner, M. Unberath, M. Levenston, G. Gold, R. Fahrig, and A. K. Maier. "Epipolar consistency conditions for motion correction in weight-bearing imaging". In: *Bildverarbeitung für die Medizin 2017*, pp. 209–214, Springer, 2017.

[Blon 06] C. Blondel, G. Malandain, R. Vaillant, and N. Ayache. "Reconstruction of coronary arteries from a single rotational X-ray projection sequence". *IEEE Transactions on Medical Imaging*, Vol. 25, No. 5, pp. 653–663, 2006.

[Blum 10] T. Blum, M. Wieczorek, A. Aichert, R. Tibrewal, and N. Navab. "The effect of out-of-focus blur on visual discomfort when using stereo displays". In: *Mixed and Augmented Reality (ISMAR), 2010 9th IEEE International Symposium on*, pp. 13–17, IEEE, 2010.

[Bran 13] S. S. Brandt, K. Hommelhoff Jensen, and F. Lauze. "Bayesian Epipolar Geometry Estimation from Tomographic Projections". In: K. M. Lee, Y. Matsushita, J. M. Rehg, and Z. Hu, Eds., *Asian Conference on Computer Vision – ACCV 2012*, pp. 231–242, Springer Berlin Heidelberg, Berlin, Heidelberg, 2013.

[Breh 12] M. Brehm, P. Paysan, M. Oelhafen, P. Kunz, and M. Kachelrieß. "Self-adapting cyclic registration for motion-compensated cone-beam CT in image-guided radiation therapy". *Medical Physics*, Vol. 39, No. 12, pp. 7603–7618, 2012.

[Bruy 02] P. P. Bruyant, M. A. King, and P. H. Pretorius. "Correction of the respiratory motion of the heart by tracking of the center of mass of thresholded projections: a simulation study using the dynamic MCAT phantom". *IEEE Transactions on Nuclear Science*, Vol. 49, No. 5, pp. 2159–2166, 2002.

[Buzu 08] T. M. Buzug. *Computed Tomography: From Photon Statistics to Modern Cone-Beam CT*. Springer, 2008.

[Chan 17] Z. Chang, R. Zhang, J.-B. Thibault, D. Pal, L. Fu, K. Sauer, and C. Bouman. "Modeling and pre-treatment of photon-starved CT data for iterative reconstruction". *IEEE Transaction on Medical Imaging*, Vol. 36, No. 1, pp. 277–287, 2017.

[Chen 05] G.-H. Chen and S. Leng. "A new data consistency condition for fan-beam projection data". *Medical Physics*, Vol. 32, No. 4, pp. 961–967, Apr 2005.

[Chen 08] G.-H. Chen, J. Tang, and S. Leng. "Prior image constrained compressed sensing (PICCS): a method to accurately reconstruct dynamic CT images from highly undersampled projection data sets". *Medical Physics*, Vol. 35, No. 2, pp. 660–663, 2008.

[Chum 03] O. Chum, T. Werner, and T. Pajdla. "Joint Orientation of Epipoles". In: *British Machine Vision Conference (BMVC)*, pp. 6.1–6.10, British Machine Vision Association, 2003.

[Clac 13a] R. Clackdoyle. "Necessary and sufficient consistency conditions for fan-beam projections along a line". *IEEE Transactions on Nuclear Science*, Vol. 60, No. 3, pp. 1560–1569, 2013.

[Clac 13b] R. Clackdoyle and L. Desbat. "Full data consistency conditions for cone-beam projections with sources on a plane". *Physics in Medicine & Biology*, Vol. 58, No. 23, pp. 8437–8456, Dec 2013.

[Clac 15] R. Clackdoyle, M. Defrise, L. Desbat, and J. Nuyts. "Consistency of fan-beam projections along an arc of a circle". In: *Proc. 13th Int. Meeting Fully Three-Dimensional Image Reconstruction Radiol. Nucl. Med.*, pp. 253–256, 2015.

[Clac 16] R. Clackdoyle, L. Desbat, J. Lesaint, and S. Rit. "Data Consistency Conditions for Cone-Beam Projections on a Circular Trajectory". *IEEE Signal Processing Letters*, Vol. 23, No. 12, pp. 1746–1750, 2016.

[Clac 94] R. Clack and M. Defrise. "Cone-beam reconstruction by the use of Radon transform intermediate functions". *JOSA A*, Vol. 11, No. 2, pp. 580–585, 1994.

[Corm 63] A. M. Cormack. "Representation of a function by its line integrals, with some radiological applications". *Journal of Applied Physics*, Vol. 34, No. 9, pp. 2722–2727, Apr 1963.

[Coxe 87] H. S. Coxeter. *Projective Geometry*. Springer New York, 1987.

[De M 09] B. De Man and J. A. Fessler. "Statistical iterative reconstruction for x-ray computed tomography". 2009.

[Debb 13] C. Debbeler, N. Maass, M. Elter, F. Dennerlein, and T. M. Buzug. "A new CT rawdata redundancy measure applied to automated misalignment correction". In: *Proceedings of the 12th international meeting on fully three-dimensional image reconstruction in radiology and nuclear medicine*, pp. 264–267, 2013.

[Defr 12] M. Defrise, A. Rezaei, and J. Nuyts. "Time-of-flight PET data determine the attenuation sinogram up to a constant". *Physics in Medicine & Biology*, Vol. 57, No. 4, p. 885, 2012.

[Edho 86] P. R. Edholm, R. M. Lewitt, and B. Lindholm. "Novel Properties Of The Fourier Decomposition Of The Sinogram". In: *Proceedings of the international society for optics and photonics SPIE*, pp. 8–18, 1986.

[Erla 00] K. Erlandsson, D. Visvikis, W. Waddington, and P. Jarritt. "Truncation reduction in fan-beam transmission scanning using the Radon transform consistency conditions". *IEEE Transactions on Nuclear Science*, Vol. 47, No. 3, pp. 989–993, Jun 2000.

[Feld 84] L. A. Feldkamp, L. C. Davis, and J. W. Kress. "Practical cone-beam algorithm". *Journal of the Optical Society of America A*, Vol. 1, No. 6, pp. 612–619, Jun 1984.

[Fels 17] L. Felsner, A. Aichert, M. Unberath, and A. K. Maier. "Motion Estimation in Rotational Angiography with α–Expansion Moves". In: *IEEE Nuclear Science Symposium Conference Record (NSS)*, 2017.

[Fran 98] A. F. Frangi, W. J. Niessen, K. L. Vincken, and M. A. Viergever. "Multiscale vessel enhancement filtering". In: *International Conference on Medical Image Computing and Computer-Assisted Intervention*, pp. 130–137, Springer, 1998.

[Frys 15] R. Frysch and G. Rose. "Rigid Motion Compensation in Interventional C-arm CT Using Consistency Measure on Projection Data". In: N. Navab, J. Hornegger, W. M. Wells, and A. Frangi, Eds., *International Conference on Medical Image Computing and Computer-Assisted Intervention*, pp. 298–306, Springer International Publishing, 2015.

[Gord 70] R. Gordon, R. Bender, and G. T. Herman. "Algebraic reconstruction techniques (ART) for three-dimensional electron microscopy and X-ray photography". *Journal of theoretical Biology*, Vol. 29, No. 3, pp. 471–481, 1970.

[Gran 91] P. Grangeat. "Mathematical framework of cone beam 3D reconstruction via the first derivative of the Radon transform". In: G. T. Herman, A. K. Louis, and F. Natterer, Eds., *Mathematical Methods in Tomography*, pp. 66–97, Springer, Berlin, Germany, 1991.

[Gras 62] H. Grassmann. *Die Ausdehnungslehre*. T.C.F. Enslin, 1862.

[Grul 15] T. Grulich, W. Holub, U. Haßler, A. Aichert, and A. K. Maier. "Geometric adjustment of X-ray tomosynthesis". In: *Proc. Fully Three-Dimensional Image Reconstruct. Radiol. Nucl. Med.*, pp. 468–471, 2015.

[Hart 00] R. I. Hartley and A. Zisserman. *Multiple View Geometry in Computer Vision*. Cambridge University Press, ISBN: 0521623049, 2000.

[Helg 84] S. Helgason. *Groups and geometric analysis: Radon transforms, invariant differential operators and spherical functions*. Vol. 1, Academic press, 1984.

[Hoff 18] M. Hoffmann, T. Würfl, N. Maaß, F. Dennerlein, A. Aichert, and A. K. Maier. "Empirical Scatter Correction using the Epipolar Consistency Condition". In: *5th International Conference on Image Formation in X-Ray Computed Tomography*, pp. 193–197, 2018.

[Houn 73] G. N. Hounsfield. "Computerized transverse axial scanning (tomography): Part 1. Description of system". *The British Journal of Radiology*, Vol. 46, No. 552, pp. 1016–1022, 1973.

[Huan 17] Y. Huang, X. Huang, O. Taubmann, Y. Xia, V. Haase, J. Hornegger, G. Lauritsch, and A. K. Maier. "Restoration of Missing Data in Limited Angle Tomography Based on Helgason-Ludwig Consistency Conditions". *Biomedical Physics & Engineering Express*, Vol. 3, No. 3, 2017.

[Huan 18] Y. Huang, O. Taubmann, X. Huang, G. Lauritsch, and A. K. Maier. "Papoulis–Gerchberg algorithms for limited angle tomography using data consistency conditions". In: *5th International Conference on Image Formation in X-Ray Computed Tomography*, pp. 189–192, 2018.

[John 04] F. John. *Plane waves and spherical means applied to partial differential equations*. Courier Corporation, 2004.

[John 14] S. G. Johnson. "The NLopt nonlinear-optimization package". 2014.

[John 38] F. John. "The ultrahyperbolic differential equation with four independent variables". *Duke Mathematical Journal*, Vol. 4, No. 2, pp. 300–322, 06 1938.

[Klei 72] F. C. Klein. *Vergleichende Betrachtungen über neuere geometrische Forschungen (Das Erlanger Programm).* Verlag Andreas Deichert, Erlangen, 1872.

[Kold 10] D. Kolditz, M. Meyer, Y. Kyriakou, and W. A. Kalender. "Comparison of extended field-of-view reconstructions in C-arm flat-detector CT using patient size, shape or attenuation information". *Physics in Medicine & Biology*, Vol. 56, No. 1, p. 39, 2010.

[Kutt 08] O. Kutter, A. Aichert, C. Bichlmeier, J. Traub, S. Heining, B. Ockert, E. Euler, and N. Navab. "Real-time volume rendering for high quality visualization in augmented reality". In: *International Workshop on Augmented environments for Medical Imaging including Augmented Reality in Computer-aided Surgery (AMI-ARCS 2008), New York, USA*, 2008.

[Lang 13] T. Lang *et al.* "Automatic misalignment correction method for cone-beam CT". European Congress of Radiology 2013, 2013.

[Laur 06] G. Lauritsch, J. Boese, L. Wigstrom, H. Kemeth, and R. Fahrig. "Towards cardiac C-arm computed tomography". *IEEE Transaction on Medical Imaging*, Vol. 25, No. 7, pp. 922–934, 2006.

[Lave 96] S. Laveau and O. D. Faugeras. "Oriented Projective Geometry for Computer Vision". In: *Processding of the European Computer Vision Conference 1996*, pp. 147–156, Springer-Verlag, 1996.

[Laza 08] N. Lazaros, G. C. Sirakoulis, and A. Gasteratos. "Review of stereo vision algorithms: from software to hardware". *International Journal of Optomechatronics*, Vol. 2, No. 4, pp. 435–462, 2008.

[Leeu 18] T. van Leeuwen, S. Maretzke, and K. J. Batenburg. "Automatic alignment for three-dimensional tomographic reconstruction". *Inverse Problems*, Vol. 34, No. 2, 2018.

[Lesa 16] J. Lesaint, R. Clackdoyle, S. Rit, and L. Desbat. "Two cone-beam consistency conditions for a circular trajectory". In: *Proc. 4th Int. Conf. Image Formation X-Ray Comput. Tomography*, pp. 431–434, 2016.

[Lesa 17a] J. Lesaint, S. Rit, R. Clackdoyle, and L. Desbat. "Calibration for Circular Cone-Beam CT Based on Consistency Conditions". *IEEE Transactions on Radiation and Plasma Medical Sciences*, Vol. 1, No. 6, pp. 517–526, 2017.

[Lesa 17b] J. Lesaint, S. Rit, R. Clackdoyle, and L. Desbat. "Calibration for Circular Cone-Beam CT Based on Consistency Conditions". *IEEE Transactions on Radiation and Plasma Medical Sciences*, Vol. 1, No. 6, pp. 517–526, 2017.

[Lesa 18a] J. Lesaint, A. Aichert, S. Rit, L. Desbat, and R. Clackdoyle. "Epipolar Consistency Conditions: with or without Grangeat". In: *IEEE Nuclear Science Symposium Conference Record (NSS)*, 2018.

[Lesa 18b] J. Lesaint. *Data consistency conditions in X-ray transmission imaging and their application to the self-calibration problem.* PhD thesis, Communauté Universite Grenoble Alpes, 2018.

[Levi 10] M. S. Levine, E. Y. Sidky, and X. Pan. "Consistency Conditions for Cone-Beam CT Data Acquired with a Straight-Line Source Trajectory". *Tsinghua Science and Technology*, Vol. 15, No. 1, pp. 56–61, Feb 2010.

[Levo 06] M. Levoy. “Light fields and computational imaging”. *Computer*, No. 8, pp. 46–55, 2006.

[Lewi 83] R. M. Lewitt. “Reconstruction algorithms: transform methods”. *Proceedings of the IEEE*, Vol. 71, No. 3, pp. 390–408, 1983.

[Liu 17] R. Liu, L. He, Y. Luo, and H. Yu. “Singular value decomposition-based 2D image reconstruction for computed tomography”. *Journal of X-ray Science and Technology*, Vol. 25, No. 1, pp. 113–134, 2017.

[Loop 99] C. Loop and Z. Zhang. “Computing rectifying homographies for stereo vision”. In: *Computer Vision and Pattern Recognition, 1999. IEEE Computer Society Conference on.*, pp. 125–131, IEEE, 1999.

[Ludw 66] D. Ludwig. “The radon transform on euclidean space”. *Communications on Pure and Applied Mathematics*, Vol. 19, No. 1, pp. 49–81, Feb 1966.

[Luo 18] S. Luo and S. Luo. “An Epipolar Based Algorithm for Respiratory Signal Extraction of Small Animal CT”. *Sensing and Imaging*, Vol. 19, No. 1, Feb 2018.

[Maas 14] N. Maass, F. Dennerlein, A. Aichert, and A. K. Maier. “Geometrical jitter correction in computed tomography”. In: *Proceedings of the third international conference on image formation in X-ray computed tomography, edited by Frederic Noo, Salt Lake City*, pp. 338–342, 2014.

[Maie 11] A. K. Maier, J. H. Choi, A. Keil, C. Niebler, M. Sarmiento, A. Fieselmann, G. Gold, S. Delp, and R. Fahrig. “Analysis of Vertical and Horizontal Circular C-Arm Trajectories”. In: *Proceedings of the international society for optics and photonics SPIE*, pp. 7961231–7961238, 2011.

[Maie 12] A. K. Maier, H. G. Hofmann, C. Schwemmer, J. Hornegger, A. Keil, and R. Fahrig. “Fast simulation of x-ray projections of spline-based surfaces using an append buffer”. *Physics in Medicine & Biology*, Vol. 57, No. 19, p. 6193, 2012.

[Maie 18] A. K. Maier, S. Steidl, V. Christlein, and J. Hornegger. *Medical Imaging Systems: An Introductory Guide*. Vol. 11111, Springer, 2018.

[Manh 13] M. T. Manhart, M. Kowarschik, A. Fieselmann, Y. Deuerling-Zheng, K. Royalty, A. K. Maier, and J. Hornegger. “Dynamic iterative reconstruction for interventional 4-D C-arm CT perfusion imaging”. *IEEE Transaction on Medical Imaging*, Vol. 32, No. 7, pp. 1336–1348, 2013.

[Mark 12] P. Markelj, D. Tomaževič, B. Likar, and F. Pernuš. “A review of 3D/2D registration methods for image-guided interventions”. *Medical image analysis*, Vol. 16, No. 3, pp. 642–661, 2012.

[Mazi 10] S. R. Mazin and N. J. Pelc. “Fourier properties of the fan-beam sinogram”. *Medical Physics*, Vol. 37, No. 4, pp. 1674–1680, Apr 2010.

[Metz 02] S. Metzler, J. Bowsher, and R. Jaszczak. “Geometrical similarities of the Orlov and Tuy sampling criteria and a numerical algorithm for assessing sampling completeness”. In: *Nuclear Science Symposium Conference Record, 2002 IEEE*, pp. 1241–1245, IEEE, 2002.

[Mull 14] K. Müller, A. Maier, C. Schwemmer, G. Lauritsch, S. De Buck, J. Wielandts, J. Hornegger, and R. Fahrig. "Image artefact propagation in motion estimation and reconstruction in interventional cardiac C-arm CT". *Physics in Medicine & Biology*, Vol. 59, No. 12, p. 3121, 2014.

[Natt 86] F. Natterer. *The Mathematics of Computerized Tomography. Wiley-Teubner series in computer science*, Wiley, 1986.

[Ohne 00] B. Ohnesorge, T. Flohr, K. Schwarz, J. Heiken, and K. Bae. "Efficient correction for CT image artifacts caused by objects extending outside the scan field of view". *Medical Physics*, Vol. 27, No. 1, pp. 39–46, 2000.

[Pane 08] D. Panetta, N. Belcari, A. Del Guerra, and S. Moehrs. "An optimization-based method for geometrical calibration in cone-beam CT without dedicated phantoms". *Physics in Medicine & Biology*, Vol. 53, No. 14, p. 3841, 2008.

[Patc 02] S. K. Patch. "Consistency conditions upon 3D CT data and the wave equation". *Physics in Medicine & Biology*, Vol. 47, No. 15, p. 2637, 2002.

[Pluc 68] J. Plücker. *Neue Geometrie des Raumes: gegründet auf die Betrachtung der geraden Linie als Raumelement. erste Abteilung. Neue Geometrie des Raumes: gegründet auf die Betrachtung der geraden Linie als Raumelement : zwei Abtheilungen in einem Bande*, Teubner, 1868.

[Preu 15] A. Preuhs, M. Berger, Y. Xia, A. K. Maier, J. Hornegger, and R. Fahrig. "Over-Exposure Correction in CT Using Optimization-Based Multiple Cylinder Fitting". In: T. Deserno, H. Handels, H.-P. Meinzer, and T. Tolxdorff, Eds., *Bildverarbeitung für die Medizin 2015*, pp. 35–40, Mar 2015.

[Preu 18] A. Preuhs, A. K. Maier, M. Manhart, J. Fotouhi, N. Navab, and M. Unberath. "Double Your Views-Exploiting Symmetry in Transmission Imaging". *arXiv preprint arXiv:1803.10650*, 2018.

[Preu 19] A. Preuhs, M. Manhart, E. Hoppe, M. Kowarschik, and A. K. Maier. "Motion gradients for epipolar consistency". In: *15th International Meeting on Fully Three-Dimensional Image Reconstruction in Radiology and Nuclear Medicine*, p. 110720D, International Society for Optics and Photonics, 2019.

[Prum 09] M. Prummer, J. Hornegger, G. Lauritsch, L. Wigstrom, E. Girard-Hughes, and R. Fahrig. "Cardiac C-arm CT: a unified framework for motion estimation and dynamic CT". *IEEE Transaction on Medical Imaging*, Vol. 28, No. 11, pp. 1836–1849, 2009.

[Rado 17] J. Radon. "Über die Bestimmung von Funktionen durch ihre Integralwerte längs gewisser Mannigfaltigkeiten". *Berichte über die Verhandlungen der Königlich-Sächsischen Akademie der Wissenschaften zu Leipzig, Mathematisch-Physische Klasse*, Vol. 69, pp. 262–277, 1917.

[Raus 16] J. Rausch, A. K. Maier, R. Fahrig, J.-H. Choi, W. Hinshaw, F. Schebesch, S. Haase, J. Wasza, J. Hornegger, and C. Riess. "Kinect-based correction of overexposure artifacts in knee imaging with C-Arm CT systems". *Journal of Biomedical Imaging*, Vol. 2016, p. 1, 2016.

[Rich 11] J. Richter-Gebert. *Perspectives on projective geometry: A guided tour through real and complex geometry*. Springer Science & Business Media, 2011.

[Ries 13] C. Riess, M. Berger, H. Wu, M. Manhart, R. Fahrig, and A. K. Maier. "TV or not TV? That is the question". *Proceedings Fully3D*, pp. 341–344, 2013.

[Rit 12] S. Rit, M. Van Herk, L. Zijp, and J.-J. Sonke. "Quantification of the variability of diaphragm motion and implications for treatment margin construction". *International Journal of Radiation Oncology* Biology* Physics*, Vol. 82, No. 3, pp. e399–e407, 2012.

[Rohk 10] C. Rohkohl, G. Lauritsch, A. Keil, and J. Hornegger. "CAVAREV—an open platform for evaluating 3D and 4D cardiac vasculature reconstruction". *Physics in Medicine & Biology*, Vol. 55, No. 10, p. 2905, 2010.

[Rowa 90] T. H. Rowan. "Functional stability analysis of numerical algorithms". 1990.

[Smit 85] B. D. Smith. "Image reconstruction from cone-beam projections: necessary and sufficient conditions and reconstruction methods". *IEEE transactions on medical imaging*, Vol. 4, No. 1, pp. 14–25, 1985.

[Stro 03] N. K. Strobel, B. Heigl, T. M. Brunner, O. Schuetz, M. M. Mitschke, K. Wiesent, and T. Mertelmeier. "Improving 3 D image quality of X-ray C-arm imaging systems by using properly designed pose determination systems for calibrating the projection geometry". In: *Proceedings of the international society for optics and photonics SPIE*, pp. 943–954, 2003.

[Sybe 17] C. Syben, B. Bier, M. Berger, A. Aichert, R. Fahrig, G. Gold, M. Levenston, and A. K. Maier. "Joint calibration and motion estimation in weight-bearing cone-beam CT of the knee joint using fiducial markers". In: *2017 IEEE 14th International Symposium on Biomedical Imaging (ISBI)*, pp. 494–497, IEEE, 2017.

[Sybe 19] C. Syben, B. Stimpel, J. Lommen, T. Würfl, A. Dörfler, and A. K. Maier. "Abstract: Fan-to-Parallel Beam Conversion". In: H. Handels, T. M. Deserno, A. K. Maier, K. H. Maier-Hein, C. Palm, and T. Tolxdorff, Eds., *Bildverarbeitung für die Medizin 2019*, pp. 29–29, Springer Fachmedien Wiesbaden, Wiesbaden, 2019.

[Tang 11] S. Tang, X. Mou, Q. Xu, Y. Zhang, J. Bennett, and H. Yu. "Data consistency condition-based beam-hardening correction". *Optical Engineering*, Vol. 50, No. 7, p. 76501, Jul 2011.

[Thur 15] S. Thürauf, O. Hornung, M. Körner, F. Vogt, M. A. Nasseri, and A. Knoll. "Evaluation of a 9D-Position Measurement Method of a C-Arm Based on X-Ray Projections". In: *MICCAI: 1st Interventional Microscopy Workshop. Munich, Germany*, pp. 9–16, 2015.

[Toma 98] C. Tomasi and R. Manduchi. "Bilateral filtering for gray and color images". In: *Computer Vision, 1998. Sixth International Conference on*, pp. 839–846, IEEE, 1998.

[Truc 98] E. Trucco and A. Verri. *Introductory techniques for 3-D computer vision*. Vol. 201, Prentice Hall Englewood Cliffs, 1998.

[Tuy 83] H. K. Tuy. "An Inversion Formula for Cone-Beam Reconstruction". *SIAM Journal on Applied Mathematics*, Vol. 43, No. 3, pp. 546–552, Jun 1983.

[Unbe 16a] M. Unberath, S. Achenbach, R. Fahrig, and A. K. Maier. "Exhaustive graph cut-based vasculature reconstruction". In: *2016 IEEE 13th International Symposium on Biomedical Imaging (ISBI)*, pp. 1143–1146, IEEE, 2016.

[Unbe 16b] M. Unberath, A. Aichert, S. Achenbach, and A. K. Maier. "Improving Segmentation Quality in Rotational Angiography Using Epipolar Consistency". In: *MICCAI-Workshop on Computing and Visualization for Intravascular Imaging and Computer Assisted Stenting*, pp. 1–8, 2016.

[Unbe 16c] M. Unberath, A. Aichert, S. Achenbach, and A. K. Maier. "Virtual Single-frame Subtraction Imaging". In: *4th International Conference on Image Formation in X-Ray Computed Tomography*, pp. 89–92, 2016.

[Unbe 17a] M. Unberath, A. Aichert, S. Achenbach, and A. K. Maier. "Consistency-based respiratory motion estimation in rotational angiography". *Medical Physics*, Vol. 44, No. 9, 2017.

[Unbe 17b] M. Unberath, M. Berger, A. Aichert, and A. K. Maier. "Fourier Consistency-Based Motion Estimation in Rotational Angiography". In: *Bildverarbeitung für die Medizin 2017*, pp. 110–115, Springer, 2017.

[Unbe 18] M. Unberath, O. Taubmann, A. Aichert, S. Achenbach, and A. K. Maier. "Prior-free Respiratory Motion Estimation in Rotational Angiography". *IEEE transactions on medical imaging*, Vol. 37, No. 9, pp. 1999–2009, 2018.

[Von 04] L. Von Smekal, M. Kachelrieß, E. Stepina, and W. A. Kalender. "Geometric misalignment and calibration in cone-beam tomography: Geometric misalignment and calibration in cone-beam tomography". *Medical physics*, Vol. 31, No. 12, pp. 3242–3266, 2004.

[Wang 14] J. Wang, A. Borsdorf, B. Heigl, T. Kohler, and J. Hornegger. "Gradient-Based Differential Approach for 3-D Motion Compensation in Interventional 2-D/3-D Image Fusion". In: *3D Vision (3DV), 2014 2nd International Conference on*, pp. 293–300, IEEE, 2014.

[Wein 11] W. Wein and A. Ladikos. "Detecting patient motion in projection space for cone-beam computed tomography". In: *International Conference on Medical Image Computing and Computer-Assisted Intervention*, Springer, Sep. 2011.

[Welc 98] A. Welch, C. Campbell, R. Clackdoyle, F. Natterer, M. Hudson, A. Bromiley, P. Mikecz, F. Chillcot, M. Dodd, P. Hopwood, *et al.* "Attenuation correction in PET using consistency information". *IEEE Transactions on Nuclear Science*, Vol. 45, No. 6, pp. 3134–3141, 1998.

[Wick 12] J. Wicklein, H. Kunze, W. A. Kalender, and Y. Kyriakou. "Image features for misalignment correction in medical flat-detector CT". *Medical Physics*, Vol. 39, No. 8, pp. 4918–4931, Aug 2012.

[Wiec 10] M. Wieczorek, A. Aichert, O. Kutter, C. Bichlmeier, J. Landes, S. M. Heining, E. Euler, and N. Navab. "GPU-accelerated Rendering for Medical Augmented Reality in Minimally-invasive Procedures.". In: *Bildverarbeitung für die Medizin 2010*, pp. 102–106, 2010.

[Wiec 11] M. Wieczorek, A. Aichert, P. Fallavollita, O. Kutter, A. Ahmadi, L. Wang, and N. Navab. "Interactive 3D visualization of a single-view X-Ray image". In: *International Conference on Medical Image Computing and Computer-Assisted Intervention*, pp. 73–80, Springer, 2011.

[Wurf 17] T. Würfl, N. Maaß, F. Dennerlein, X. Huang, and A. Maier. "Epipolar Consistency Guided Beam Hardening Reduction-ECC 2". *Fully Three-Dimensional Image Reconstruction in Radiology and Nuclear Medicine*, pp. 181–185, 2017.

[Wurf 18] T. Würfl, N. Maaß, F. Dennerlein, A. Aichert, and A. K. Maier. "Physical Constraints for Beam Hardening Reduction using Polynomial Models". In: *5th International Conference on Image Formation in X-Ray Computed Tomography*, pp. 356–359, 2018.

[Xia 15] Y. Xia, S. Bauer, A. K. Maier, M. Berger, and J. Hornegger. "Patient-bounded extrapolation using low-dose priors for volume-of-interest imaging in C-arm CT". *Medical Physics*, Vol. 42, No. 4, pp. 1787–1796, 2015.

[Xia 17] Y. Xia, M. Berger, S. Bauer, S. Hu, A. Aichert, and A. K. Maier. "An Improved Extrapolation Scheme for Truncated CT Data Using 2D Fourier-Based Helgason-Ludwig Consistency Conditions". *International journal of biomedical imaging*, Vol. 2017, 2017.

[Xu 10] J. Xu, K. Taguchi, and B. M. W. Tsui. "Statistical Projection Completion in X-ray CT Using Consistency Conditions". *IEEE Transaction on Medical Imaging*, Vol. 29, No. 8, pp. 1528–1540, Aug 2010.

[Yu 07] H. Yu and G. Wang. "Data consistency based rigid motion artifact reduction in fan-beam CT". *IEEE Transactions on Medical Imaging*, Vol. 26, No. 2, pp. 249–260, 2007.

[Zeng 10] G. L. Zeng. *Medical image reconstruction: a conceptual tutorial.* Springer, 2010.

[Zijp 04] L. Zijp, J.-J. Sonke, and M. van Herk. "Extraction of the respiratory signal from sequential thorax cone-beam X-ray images". In: *International conference on the use of computers in radiation therapy*, pp. 507–509, 2004.

Index